Master thesis and internship[BR]- Master's thesis : H-infinity robust controller development for seismic isolation of Gravitational-Wave Detectors : Implementation on the E-TEST prototype[BR]- Integration internship

Auteur : Magain, Gilles
Promoteur(s) : Sacré, Pierre; Collette, Christophe
Faculté : Faculté des Sciences appliquées
Diplôme : Master en ingénieur civil en aérospatiale, à finalité spécialisée en "aerospace engineering"
Année académique : 2024-2025
URI/URL : http://hdl.handle.net/2268.2/23384

UNIVERSITE DE LIEGE
FACULTE DES SCIENCES APPLIQUEES

H-infinity robust controller development for seismic isolation of Gravitational-Wave Detectors : Implementation on the E-TEST prototype.

Magain Gilles

Thesis presented to obtain the degree of :
Master of Science in aerospace Engineering

Thesis supervisor(s) :
Colette Christophe
Sacré Pierre

Academic year: **2024 - 2025**

Acknowledgments

First, I would like to thank my promoters, Christophe Colette and Pierre Sacré. They have been deeply involved in my work and followed closely its evolution. I could benefit from their expertise, advice and availability during this internship.

My thanks also go to the PhD students working at the Precision Mechatronics Laboratory, always answering my questions and providing guidance. This is especially true for Haidar Lakkis and Thomas Giordano who contributed actively to the development of my work.

I also want to thank Marie Smeets, who has always been encouraging me and pushed me to the best of my capacities.

My final thanks go to my family that has always been supportive during my academic career and has provided me with everything I needed for me to be fully dedicated to my student life.

Abstract

Gravitational wave astronomy is the most recent branch of the universe observation. It will widen our spectrum of analysis due to the new information brought by those waves. However, their detection is a technical challenge since their magnitude is minimal when reaching the earth. Designs based on Michelson interferometers are used to detect them. It is mandatory to reduce any perturbation applied to those detectors since they need to have an extraordinary degree of precision. One of the main noise limiting their resolution is the ground motion. Multiple systems, active or passive, are then employed to reduce its impact on the interferometers.

This thesis adresses the challenge of seismic noise. The goal is the implementation of a robust control strategy, called H infinity, on the E-TEST prototype, which is a precursor of the Einstein Telescope. The objective is to obtain a controller, which is rarely done for such complex system using this method. This work explores the isolation of this structure, especially below $10\,Hz$, where ground motion is most pronounced. After reviewing the gravitational waves, their detectors, the major noise sources and the current isolation technologies, this thesis introduces the required knowledge of Control Theory necessary to the understanding of the implementation of such method. The core of the work is the use of two different models representing the dynamics of the active platform constituting the base of the prototype. Indeed, the H infinity procedure requires a system to produce the controllers. Those systems are meticulously defined in terms of inputs and outputs signals. This allows for the method to minimize the desired outputs using the other signals as given information to the controllers. Weights are also defined to shape the desired performances given by the method. The results of both controllers applied to their corresponding model are analyzed.

The first model, being more basic, allows for a robustness study, demonstrating the interest of such method when the system is subject to uncertainties. The second model, more complex, allows for the implementation of its controller on the prototype for damping. The performances have been validated experimentally and the limitation of the controller application have been proved to be due to the model, the latter being not precise enough. However, this experiment has proven that the implementation of controllers produced with robust control methods is possible on complex structures as the E-TEST prototype. This contributes to the ongoing development of the Einstein telescope and the technologies required for the implementation of high-resolution gravitational waves detectors.

Keywords : Gravitational waves, Seismic isolation, Robust control, H-infinity control (H_∞ control), Einstein Telescope, Active vibration control, E-TEST prototype, Low-frequency noise, MIMO systems, Control system design

Contents

Glossary of Acronyms

$\mathcal{H}_\infty$ H infinity

2DOF Two degrees of freedom

AP Active Platform

ASD Amplitude Spectral Density

BSC Basic Symmetric Chamber

CE Cosmic Explorer

COK Center of Stiffness

COM Center of Mass

CP Cryogenic Payload

DC Direct Current

E-TEST project Einstein Telescope Euregio-Meuse-Rhin Site and Technology

EMR Euregio Meuse-Rhin

ET Einstein telescope

GAS Geometric Anti-Spring

GW Gravitational Waves

HAM horizontal access module

HEPI hydraulic external pre-isolator

HF High frequency

HINS Horizontal inertial sensor

HPF High-Pass Filter

IP Inverted Pendulum

IPL Inverted pendulum leg

IPP Inverted Pendulum Platform

ISI Internal seismic isolator

KAGRA Kamioka Gravitational Wave Detector

LF Low frequency

LIGO Laser Interferometer Gravitational-Wave Observatory

LQG Linear quadratic Gaussian

LTI Linear Time Invariant

LVDT linear variable differential transformer

MD magnetic damper

MIMO multiple-input multiple-output

PID Proportional Integral Derivative

PML Precision Mechatronics Laboratory

PSD Power Spectral Density

SISO single-input single-output

SVD Singular Value Decomposition

TF Transfer Function

VINS Vertical inertial sensor

Chapter 1

Introduction

The recent detections of gravitational waves have opened possibilities on the observation of the universe, one century after the prediction of those waves by Einstein's general theory of relativity. Gravitational wave astronomy allows new discoveries thanks to large Michelson interferometers used as detectors. Existing instruments are already providing data. However, even if they have a margin for upgrades, they are limited by their design and location. Disruptive technologies are needed to push the limits of the actual sensitivity of gravitational waves detectors.

The latest generation of detectors represented by Laser Interferometer Gravitational-Wave Observatory (LIGO), Virgo and Kamioka Gravitational Wave Detector (KAGRA) are different from those currently under development. Indeed, only KAGRA operates with cryogenic mirrors. The new generation made of the Einstein telescope (ET) and Cosmic Explorer (CE) will operate large cryogenic mirrors made of silicon, with laser further into the infrared. They will also be more sensitive to low frequencies. This implies improvement in the isolation from seismic motion and gravity fluctuation. To do so, the super attenuator structure from the previous generation is re-appropriated and improved to reach the desired objective of the new detectors. However, this part corresponds to the component of the detectors that will isolate it from the ground naturally at higher frequencies. Then, it is necessary to apply active control methodology to increase the bandwidth of isolation further to the lower frequencies. Such methods will be applied to the Einstein Telescope Euregio-Meuse-Rhin Site and Technology (E-TEST project) prototype, which is part of the project organized by the concerned region that aims to prove the feasibility of the ET in its territory. Indeed, this region would be suitable to match the requirement in terms of reduced human and natural activity needed to reach the wanted level of minimal noise. The performances of the robust control method H infinity ($\mathcal{H}_\infty$) will be assessed by applying it to the prototype. Indeed, $\mathcal{H}_\infty$ and other robust methods are usually hard to implement on practical examples since a good model (and good knowledge) of the system is required. This research work aims at addressing the usability of the $\mathcal{H}_\infty$ method on such complex structure and its performances when producing a fully populated matrix controller using multiple inputs and outputs.

However, before the implementation of any method, it is important to set the context of Gravitational Waves (GW) and its related detectors. The different noise limiting the resolution of the detectors are presented and explained alongside techniques to limit those perturbations. Then, a review of the existing structure of GW detectors cited just above is made, ending with a more complete presentation of the ET and the E-TEST project. This is followed by the explanation of the basics of seismic isolation from a mechanical perspective. It is useful to know the first version inspiring the structure of the E-TEST project prototype and to understand its design. This is the content of chapter 2. Once the state of the art is known, the basics of control theory are presented in chapter 3. Those are required to understand the $\mathcal{H}_\infty$ method which is presented in this same chapter and that will be used to isolate the prototype. This chapter also provides the tools that are going to be used during the implementation for analysis purpose. Once the context is set, the state of the art concerning isolation and the theory

background is known, the setup of the prototype is precisely presented in chapter 4. Indeed, multiple models will be developed to match the dynamic of the structure. It is then mandatory to know and understand the original structure that will be modeled. Moreover, the knowledge of the available sensors and actuators is significant for the development of a controller. Chapter 5 presents the implementation of a controller using the $\mathcal{H}_\infty$ method on a model called the Two degrees of freedom (2DOF) model. This is a simple representation of the prototype that is used to highlight the different mechanics of the method. Then, the different steps taken to prepare the problem producing the controller, and its performances, are presented. This model is the only analytical in this paper, which makes its parameters easy to modify. Consequently, a section will focus on the robustness of the controller. Once this first implementation is done, chapter 6 shows the application of the method to a model made to match the dynamic of the real prototype. The controller obtained will be used experimentally. The theoretical and practical performances will then be compared. In the chapter 7, the conclusion is drawn, and the future work is outlined. Indeed, this paper is only the initial step in the implementation of the $\mathcal{H}_\infty$ method to real complex systems.

Chapter 2

State of the art

In this chapter, the context of the GW and their detectors are set. The different limiting noises are presented alongside techniques to improve their resolution. Then, a review of the different existing GW detectors will be made alongside the presentation of the future ET and the E-TEST project which aims at developing technologies useful for the detector and its goal performances. It will appear clear that the projected design of ET is elaborated with the knowledge acquired by the previous generation of GW detectors. Finally, the basics of seismic isolation are presented. The first part focuses on the passive isolation possibilities while the second is about active techniques.

2.1 Gravitational waves

Gravitational waves are ripples in space [1]. More precisely, they are time-dependent strains in space-time that can be defined as

$$h = \frac{\delta L}{L} \tag{2.1}$$

L being the distance between two reference points, δL the induced displacement over L and h the strain which is induced perpendicular to the axis of the gravitational wave propagation.
Gravitational waves are transverse, which means that they oscillate perpendicularly to the direction of propagation, and they travel at the speed of light. A wave travelling in the z direction will then compress space along the x-axis while stretching it along the y-axis (or vice versa) as can be seen in figure 2.1.

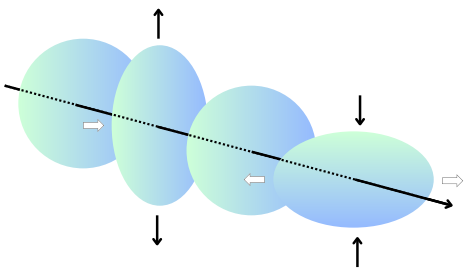

Figure 2.1: Propagation of the gravitational wave and its transverse property. The figure is based on a scheme retrieved from [2].

GW are completely different from the other astrophysical messengers such as photons, neutrinos or cosmic rays. However, they provide unique information about extremely energetic processes in the universe by bringing data about the dynamics of massive objects at relativistic speeds such as black

holes or neutron stars orbiting each other. Indeed, they are produced when matter is accelerated in an asymmetrical way. However, due to their interaction nature, detectable signals are produced only for very large masses in very strong gravitational field, which is not present on earth. Asymmetrical explosions of stars, as supernovae, can also produce such waves. Those events are quite far away, making the detection of gravitational wave very difficult as they will be very weak when finally passing by the earth. [3] Their signals are occupying a wide range of frequency, from ripples in the cosmological background at $10^{-17}\,Hz$ to formation of neutron stars in supernovae explosion at $10^{3}\,Hz$. Also, signals coming from the coalescence of binary stars system have a relatively simple form, their strength and evolution time being enough to obtain the distance to the source. This makes the detection of the waves an additional tool for distance computation.

The problem encountered by the physicists is related to the magnitude of the strain in the vicinity of earth. Indeed, even with violent event, the order of magnitude is 10^{-21} or lower. To detect few events per year, the amplitude sensitivity of a supposed detector should be close to 10^{-22} for timescales as short as a millisecond. This leads to a bandwidth of $1000\,Hz$. The spectral density of the amplitude sensitivity is then $\frac{10^{-22}[-]}{\sqrt{1000\,[Hz]}}$, giving an amplitude spectral density lower than $10^{-23}\,Hz^{-1/2}$. Those values clearly indicate that any type of disturbance, even small, will have an impact on the measurement. Then, any noise needs to be minimized.

2.2 Gravitational waves detectors

GW detectors allow scientists to have access to the information contained in those waves. The most common detector type is the ground-based. It was the first type to be designed. Joseph Weber, in the 1980s, looked for tidal strains in aluminium bars at room temperature, well isolated from acoustic noise and ground vibration. Those were resonant around $1600\,Hz$ which is the supposed peak of collapsing stars. However, no confirmation of their results has been possible. Studies have been pursued, and Weber bar type detectors now go to a sensitivity level of 10^{-18} for a millisecond pulse thanks to a cooling strategy. The biggest drawback of those detectors is that they are sensitive only to signal with enough energy in narrowband around their resonance frequency.

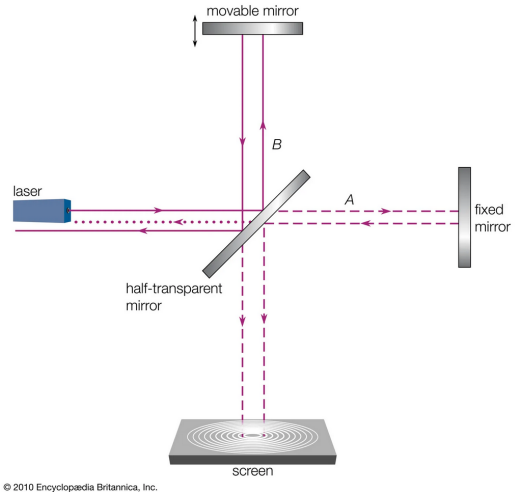

(a) Representation of a Michelson interferometer. The figure is retrieved from [4].

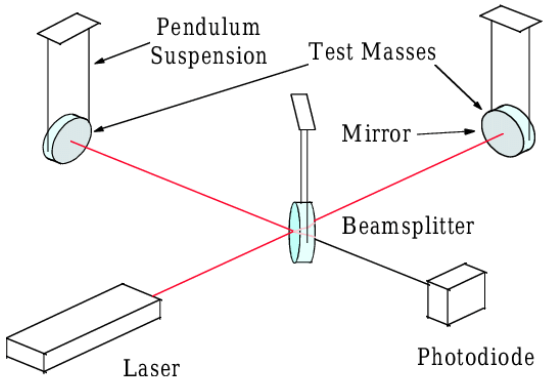

(b) Schematic of a gravitational wave detector using the principle of a Michelson interferometer with test masses. The figure is retrieved from [5].

Figure 2.2: General Schematic of Interferometer and gravitational wave detector, the design of the latest being inspired by the first.

The principle of a simple Michelson interferometer, as depicted in figure 2.2a and 2.2b, is an alternative design which provides the high sensitivity over a wide bandwidth. This design uses test masses far from each other and freely suspended to isolate them from ground displacement and thermal noise. Then, thanks to the interferometer design, the motion of those masses can be sensed when they interact with gravitational waves. If a GW crosses the interferometer in the perpendicular direction, one of the arms will increase in length while the other will decrease, resulting in a change in the output of the detector. Those interferometric detectors require a strain noise floor around $2 \times 10^{-23}\, Hz^{-1/2}$. The arms length of the ground based detectors being limited by practical implementation, such as the cost or the geographic possibilities, realistic length must be assumed. However, this will limit the sensitivity of the detector. Assuming an arm length between 3 and $4\, km$, detecting strains discussed earlier would require a residual motion of the test masses of about $3 \times 10^{-20}\, m(Hz)^{-1/2}$ over the operating range of the detector [5], which should be from around $10\, Hz$ and a few kHz. This highlights the necessity of the reduction of each type of noise possibly causing interferences for the detection.

2.3 The limiting noises

In this section, the main sources of noise limiting the sensitivity of the gravitational waves detectors will be presented. It is theoretically possible to build a system limited only by the Heisenberg Uncertainty Principle. However, practical issues will prevent this possibility. At low frequencies, the fluctuating gravitational gradient is one of the main limitations for the sensitivity of the interferometer. This is the main argument for pursuing those detection experiments in space. For the ground based detectors, the rest of the limiting perturbations are the seismic vibration and other ground mechanical noise, thermal noise of the test masses and their suspensions and shot noise from the photodiodes used to monitor the interference pattern. This is stated in [6] and can be seen in figure 2.3 where the different sources of noise are presented depending on the frequency. This plot concerns Advanced LIGO. Which is explained is confirmed at low frequencies, only the shot noise is not presented on this graph.

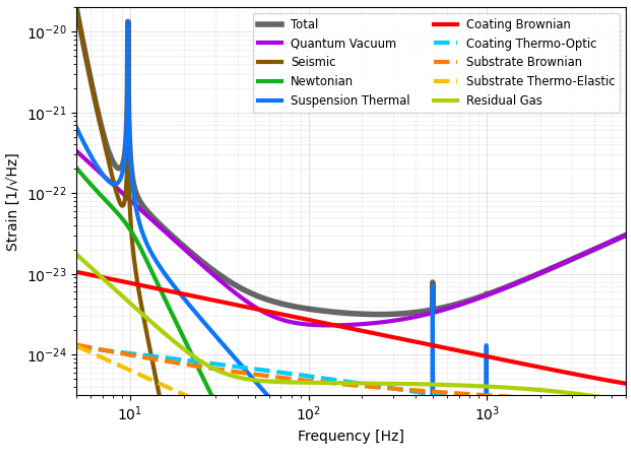

Figure 2.3: Noise budget of the different sources of disturbance in the case of Advanced LIGO. The figure is retrieved from [7].

2.3.1 Seismic Noise

In the three dimensions, the seismic noise in a quiet site on earth would be quantified by the following spectrum $10^{-7} f^{-2}\, m(Hz)^{-1/2}$ where f is the frequency in Hz. Then, if the sensitivity must be around $3 \times 10^{-20}\, m(Hz)^{-1/2}$, for a frequency of $30\, Hz$, the isolation must be greater than 10^9, nine order of magnitude. Since the seismic noise is in three dimensions, vertical isolation must also be considered. Then, those isolation levels for the horizontal motion can be reached by using a pendulum. As will

be presented later, this will offer a roll-off following $\frac{1}{frequency^2}$ above the pendulum frequency. For the vertical direction, the isolation can be achieved by suspending the test mass to a spring. Those designs will be discussed in section 2.7 where the various existing gravitational wave detectors are presented. A simple example of this kind of solution is the GEO 600 detector presented in figure 2.4. However, it must be clear that the performances provided by GEO 600 are not sufficient to detect GW. It simply presents the different characteristics that are used in the different super-attenuators that are presented in section 2.7.

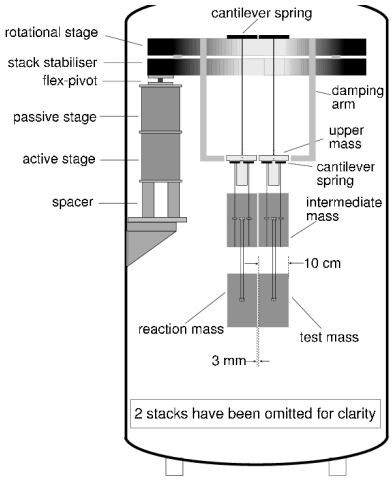

Figure 2.4: Schematic of the isolation solution used for the GEO600 gravitational wave detector. The figure is retrieved from [5] [8].

It can be seen that the test mass is hung from a pendulum of three stages, including the test mass itself, which ensures the horizontal isolation. The first two stages are hung to a cantilever spring in order to perform the vertical isolation. The whole structure is then hung from a passive isolation platform which is on an active electro-mechanical anti-vibration system. This design will then be augmented and perfected for the latest generation of gravitational wave detectors. Since a pendulum is introduced in the solution structure, the motions at its resonance frequencies need to be cut down. To do so, active damping of the pendulum modes must be incorporated, and to reduce the response at low frequency around the seismic peak, low frequency isolators have to be used.

2.3.2 Thermal Noise

The thermal noise applied to the mirror mass and the last stages of the suspension pendulum is one of the main noise sources at low frequencies. The thermal noise in the operating range of the detector comes from the tails of the resonant modes of the test masses. The spectral density of thermal motion of the test mass, for any harmonic oscillator, as a mass hung on a spring or to a pendulum, can be expressed as

$$x^2(\omega) = \frac{4k_B T\omega_0^2\phi(\omega)}{\omega m\left[(\omega_0^2-\omega^2)^2+\omega_0^4\phi^2(\omega)\right]}, \tag{2.2}$$

with k_B the Boltzmann's constant, T the temperature, m the mass and $\phi(\omega)$ the loss angle or loss factor of the oscillator having an angular resonant frequency ω_0. This loss factor is the phase lag angle between the motion of the mass and a force applied to it at a frequency far below ω_0. For example, in the case of a mass on a spring, the loss factor is a measure of the mechanical energy which is lost due to the material of the spring. Considering the pendulum strategy used here, the major part of the energy is stored in the lossless gravitational field, resulting in a loss factor lower than the one of the material

used for the wires of the pendulum. Indeed, for a pendulum with a test mass m which is suspended by four wires of length l, the loss factor of the pendulum can be expressed as [9]

$$\phi_{pend}(\omega) = \phi_{mat}(\omega)\frac{4\sqrt{TEI}}{mgl}, \tag{2.3}$$

With I the moment of the cross-section of each wire, T the tension in each wire and E the Young's modulus of those wires. It is then interesting to notice that this expression is not dependent on the frequency over the bandwidth of interest of the gravitational wave detector, which is the case for most material's loss factor. To estimate the effective internal thermal noise of a test mass, every resonant mode of the mass can be considered as a harmonic oscillator. Also considering that the detector operational range is below the resonances of the masses, the effective spectral density of the displacement resulting from internal thermal noise can be expressed as

$$x^2(\omega) = \frac{\beta 4k_b T\phi_{mat}(\omega)}{m\omega\omega_0^2}, \tag{2.4}$$

Where m is the mass of the test mass, ω is the angular frequency comprised in the range of the detector, ω_0 is the resonant angular frequency of the fundamental mode, $\phi_{mat}(\omega)$ is the material loss, and β is the correction factor including the motion due to the higher order modes of the test mass. Its value is currently lower than 10. Then, to minimize the thermal noise, the mechanical loss factor of the different materials used for the test masses and the resonance frequency of the pendulum should be the lowest possible. Moreover, the test masses should be shaped to maximize their internal resonance frequencies.

2.3.3 Shot Noise

Photons are quantum particles. They can only come in whole numbers, no fraction of photon can be collected in a device. Then, even from an unvarying source of light, for a given time span of interval, it is unlikely that the same number of photons at multiple intervals will be collected. Instead, the number of collected photons will follow a Poisson distribution as can be seen on figure 2.5. Then, the variability of the number of photons from an interval to the next one is the shot noise. This type of noise will limit the sensitivity of optical devices.

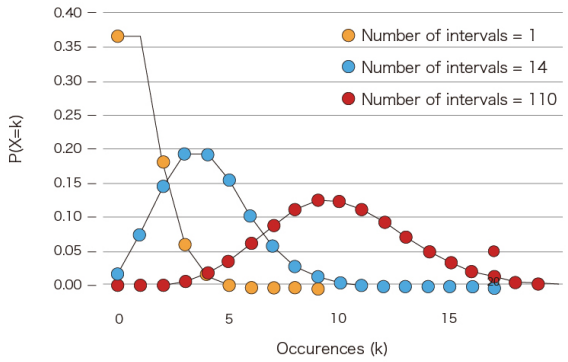

Figure 2.5: Poisson distributions depending on the number of interval. This represents the distribution of the number of photon collected in a device. [10]

Gravitational waves can be detected thanks to the outputs of our interferometer, which is a chosen point in a fringe pattern. The best choice is not at any maximum or minimum since any slight disturbances would not be easily detected as the pattern is very flat at those points. Indeed, it can

be visualized as a sinus curve, having a null derivative at each peak and valley. Then, the point with the biggest derivative should be selected. It can then be set as the halfway up point. Any slight perturbation in the arms length would result in a consequent change in the output of the interferometer. Those changes would be monitored by a photodiode. Then, shot noise could limit the sensitivity of the optical readout scheme. The sensitivity can be expressed as in equation 2.5 or 2.6.

$$\text{detectable strain in time } \tau = \frac{1}{L}\left[\frac{\lambda h c}{2\pi^2 P \tau}\right]^{1/2} \tag{2.5}$$

or,

$$\text{detectable strain } Hz^{-1/2} = \frac{1}{L}\left[\frac{\lambda h c}{\pi^2 P}\right]^{1/2}, \tag{2.6}$$

with P the laser power, λ the wavelength of the laser, L the length of the interferometer arms, τ the time, c the velocity of light, and h the Planck's constant. The assumption of a quantum efficiency of 1 for the photodetector is made. Then, taking into account the shot noise, the power required to obtain the desired sensitivity is $6 \times 10^6\, W$. This represents a lot of energy. However, techniques to reach this level of power will be discussed in the following section.

2.4 Laser Interferometric techniques

In order to provide the power necessary to reach the wanted sensitivity despite the presence of shot noise, multiple techniques have been elaborated. They are necessary for the different detectors to be useful in the field of gravitational waves astronomy. Those techniques are presented in this section.

2.4.1 Power recycling

The signal-to-noise ratio of an interferometer can be shown to be optimum when the output light of the detector is close to minimum [11]. Then, contrary to what is presented in the previous section, it is common to use a modulation technique to operate the output at a null of the interference pattern. This is technically possible thanks to an electro-optic phase modulator placed at the beginning of the interferometer [5]. Then, if the mirrors are of good quality and of low optical loss, almost all the light input to the interferometer is reflected towards the laser. It is said that the laser is not properly impedance matched to the interferometer. This can be corrected by adding a mirror between the laser and the interferometer, a power recycling mirror. If the mirror is perfectly chosen and fitting the characteristics of the system, no light is reflected back to the laser. This is perfect impedance matching. Then, a power build-up occurs within the interferometer, increasing the power, which is suitable for shot noise diminution. Then, only considering the losses due to the mirror reflection, those taken as A per reflection, the intensity in the whole detector considered as a single cavity increases by a factor $(\pi L)/(cA\tau)$, where the number of bounces of the light is optimized for signals of timescale τ. Afterward, the following expression is obtained.

$$\text{detectable strain in time } \tau = \left(\frac{\lambda h A}{4\pi L P \tau^2}\right)^{1/2} \tag{2.7}$$

2.4.2 Signal recycling

When gravitational waves interact with the arms of the interferometer, sidebands are created alongside the frequency of the detector itself, $f_0 + f_{gw}$ and $f_0 - f_{gw}$, where f_0 is the device frequency and f_{gw} the sidebands added by the gravitational radiation intercepted by the detector. While the frequency f_0 interact destructively at the output, the sidebands f_{gw} do not necessarily act in a destructive way. Then, they are visible at the output, allowing the detection of the waves. In the same logic as for the

power recycling method, a mirror specifically chosen can be put at the output of the interferometer to send back the sidebands in the system, for them to resonate, enhancing the signal size over a certain bandwidth determined by the reflectivity of the mirror. Also, the bandwidth depends on the length of the cavity formed by the mirror and the system. It can be tuned thanks to the placement of the recycling mirror. This principle and the power recycling principle are represented in figure 2.6.

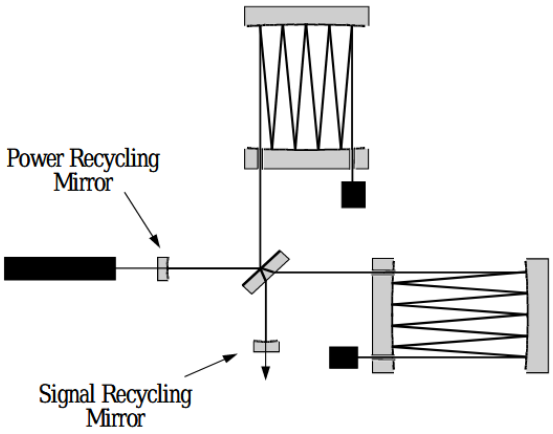

Figure 2.6: Representation of the principles of power and signal recycling in an interferometer using two recycling mirrors placed between the laser and the device, and at the output of the device. The figure has been retrieved from [6].

2.5 Fluctuation of radiation pressure

The last phenomenon having enough importance in terms of noise is the fluctuation of the radiation pressure in the arms on the test masses. For a simple Michelson interferometer with a power $P/2$ in each arm, the power spectral density of the residual motion of the test mass m due to the power fluctuation can be expressed as in equation 2.8.

$$\delta x^2(\omega) = \left(\frac{4Ph}{m^2\omega^4 c\lambda}\right), \tag{2.8}$$

where h is the Planck's constant, c is the speed of light, and λ the wavelength of the laser light. Taking into account the cavity reflection ($\sim$ 50 reflections), at a frequency of $10\,Hz$, accounting for a power of $5 \times 10^3\,W$ and a mass of $30\,kg$, the amplitude spectral density reached is $9 \times 10^{-20}\,m(Hz)^{-1/2}$ [5]. This confirms the fact that radiation pressure fluctuation has to be taken into account. Those effects can be greatly diminished by reducing the power. It is clear that a trade-off between shot noise and radiation pressure fluctuation has to be made.

2.6 The Einstein telescope and the E-TEST project

The existing gravitational waves detectors call for improvement in terms of sensitivity. However, even if those instruments have possible upgrades, they are intrinsically limited by their design and their location. Indeed, a significative improvement in sensitivity could only be reached with a disruptive technology. This is the case in the third generation of gravitational wave detectors with the Einstein telescope (ET) and Cosmic Explorer (CE).

The ET is composed of three different detectors, as presented in figure 2.7, in order to maximize the detection capability. Those detectors are composed of two Michelson interferometers. The arms

of those latest are $10\,km$ long, one is designed to specially maximize the sensitivity at high frequency and is called the High frequency (HF), and one is designed for the low frequencies and is called the Low frequency (LF). The first will be around room temperature, meaning $290\,K$ while the latest will be at cryogenic temperature around $10\,K$ to reduce thermal noise. This low frequency sensitivity is one of the main differences between the early generations of gravitational wave detectors and the third, composed of ET and CE. Moreover, one of the innovations is the use of large cryogenic mirrors made of silicon and lasers with wavelength further in the infrared (from $1550\,nm$ to around $2100\,nm$). The aim of this new generation of detectors is to be much more sensitive at low frequency.

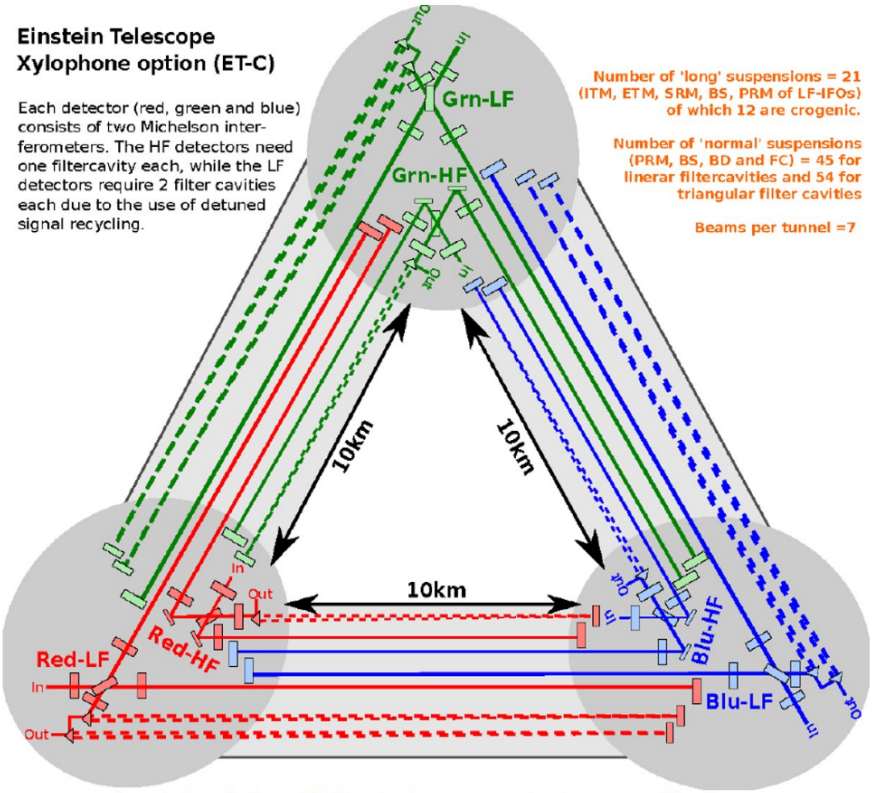

Figure 2.7: Schematic of the general geometry of the Einstein telescope. Each color correspond to a different detector (green, red and blue). Each detector has two parts, one dedicated to the LF and the other for the HF. The figure is retrieved from [12].

The E-TEST project is a project that has been recently funded by the European program interreg Euregio Meuse-Rhin (EMR). It is dedicated to activities conducted between Belgium, The Netherlands and Germany. The project unites a consortium of eleven partners from those three countries and has two objectives. The first one is to develop a method which is eco-friendly and non-invasive that would allow for the imaging of the geological conditions in the EMR region. Also, an observatory of the underground should be developed. The second is the development of the technologies needed for the third generation of detectors. Indeed, a prototype of large suspended cryogenic mirror isolated from the seismic vibration at low frequencies must be designed. This prototype will have unique features : a silicon mirror of $100\,kg$, a radiative cooling strategy, a low frequency hybrid isolation stage, cryogenic sensors and electronics, a laser and optics at $2\,microns$ and a low thermal noise coating.
The development of the second objective has been divided in two workpackages. The first is the design and the realization of a seismic attenuator which combines passive filtering with active pre-isolation stages. The goal is to have as good performance as possible in a bandwidth from $0.1 - 10\,Hz$. The development and design of the necessary cryogenic sensors and electronics is also a part of the first

workpackage. The second is focused on the optical engineering part of the problem, namely the silicon mirror, the laser and optics, the photodetectors and the low noise coating technology.

The ET project is important for the EMR region since it is one of the site candidate for hosting the detector. Also, such project, more than just the scientific or the technological return, will provide economic development in different domains. Then, multiple projects have been initiated and share some objectives. For example, the ETpathfinder project of the EMR region will bring some of the necessary technology of the E-TEST project. Those are the cryogenic state of the test mass, the silicon material used for the mirror, and the use of new wavelengths ($1550 - 2100\,nm$). However, the focus of both projects is very different since they focus on different parts of a full telescope. ETpathfinder will result in a facility laser-interferometer which could be used to test and develop other technologies. On the other hand, E-TEST project will provide a prototype working at cryogenic temperature and a seismic model used to prove that the detector can be built in the EMR region. Moreover, the E-TEST project results will be used by companies and institutes to develop other technologies or products.

2.7 Existing gravitational wave detectors

As just explained, the E-TEST project aims at improving already existing designs of GW detectors by increasing its sensitivity. Then, in this section, the different detectors from the previous generation are presented with a focus on their seismic isolation system. This is important to understand the fundamentals of the design that will be used and improved with the E-TEST project prototype. The detectors Virgo, advanced LIGO, and KAGRA which are from the previous generation are then presented. Finally, the general design of the E-TEST project prototype is explained.

2.7.1 Virgo

Virgo is a detector of gravitational waves using an interferometer structure with $3\,km$ long arms, which is a collaboration between the French CNRS and the Italian INFN located in the Pisa countryside. [13]

Its main characteristic is its high sensitivity over a wide band of frequencies, going from $10\,Hz$ to few kHz. Its goal is to have a sensitivity for spectral strain of $h = 10^{-23} - 10^{-22}\,Hz^{-1/2}$ which is equivalent to a mirror displacement of $4 \times 10^{-18}, 10^{-19}, 6 \times 10^{-20}\,mHz^{-1/2}$ at $10, 100, 1000\,Hz$ respectively. [14] Those sensitivities require reducing the horizontal seismic noise by a factor 10^9. The mirror of the interferometer is isolated from ground seismic noise thanks to the super-attenuator, which is the suspension system. Those specifications allow the gravitational wave detector to be sensitive to binaries and supernovae. Detections from a few to a few tens per year are expected. The low frequencies specifications also allow for pulsar detection by integrating the signal over one year.

The design of the super attenuator is presented in figure 2.8. In order to reach the different isolation specifications, development effort has been injected in the design of this multi-stage vibration isolator. Indeed, the amplitude spectral density of the seismic noise is expressed in all direction, for higher frequencies than $1\,Hz$, by $\frac{10^{-7}}{f^2}\,m/\sqrt{Hz}$. This is several order of magnitude larger than the mirror displacement induced by the detection of a GW signal. Moreover, sources of signals like pulsars or binaries are expected to emit at those frequencies. The reduction of the transmission of seismic vibration to the mirror is then performed by suspending the mirror, and every optical element, to the super attenuator. The function of the super attenuator is to make the residual motion of the mirror along the laser beam negligible with respect to other noise sources that can limit the sensitivity of the gravitational wave detector. This is achieved starting at $4\,Hz$. Indeed, at lower frequencies, Newtonian gravitational noise is preventing further improvement in the performances. However, from those $4Hz$ to few tens of Hz, the sensitivity is limited by the pendulum thermal noise. This represents an amplitude spectral density of $2 \times 10^{-15} f^{-5/2}\,m/\sqrt{Hz}$. Also, mechanical coupling is unavoidable as well as the non-parallelism of

two Inverted Pendulum (IP) separated by $3km$ due to the curvature of the earth. This can transform vertical vibration into horizontal displacement. Therefore, the super attenuator must be effective in every direction or degrees of freedom. As a multi-stage oscillator, the super attenuator passively reduces excitation at frequencies above the normal mode region, which corresponds to $0.03 - 2\,Hz$. However, it magnifies everything at the frequencies of this normal mode. This corresponds to natural phenomenon as Earth tidal strain or thermal effect on surface. This means that active control isolation is needed to damp those normal modes.

The super attenuator effects can be related to the mechanical low-pass filtering action of a harmonic oscillator. For a simple oscillator, the displacement induced to the point of suspension is transmitted to the suspended mass with a transfer function being $\frac{f_0^2}{f^2}$ at frequencies f being above the normal mode frequency f_0. In the case of N oscillators, there are multiple resonant frequencies $f_{01}, \cdots, f_{0N}$ and the new transfer function is

$$\frac{\Pi_{k=1}^{N} f_{0i}^2}{f^{2N}},$$

at frequencies above the highest normal mode frequency f_{0N}. As can be seen in figure 2.8, the super attenuator contains a seven-stage pendulum, which is equivalent to a chain of harmonic horizontal oscillators. Then, knowing the length l of each wire connecting consecutive stages, the pendulum resonance frequency of each stage is known to be $f_0 = \frac{1}{2\pi}\sqrt{\frac{g}{l}}$, g being the gravity acceleration. The total length of the chain is $9\,m$. With this chain, the horizontal normal modes of the attenuator are below $2.5\,Hz$ and the required attenuation is reached starting from $4\,Hz$.

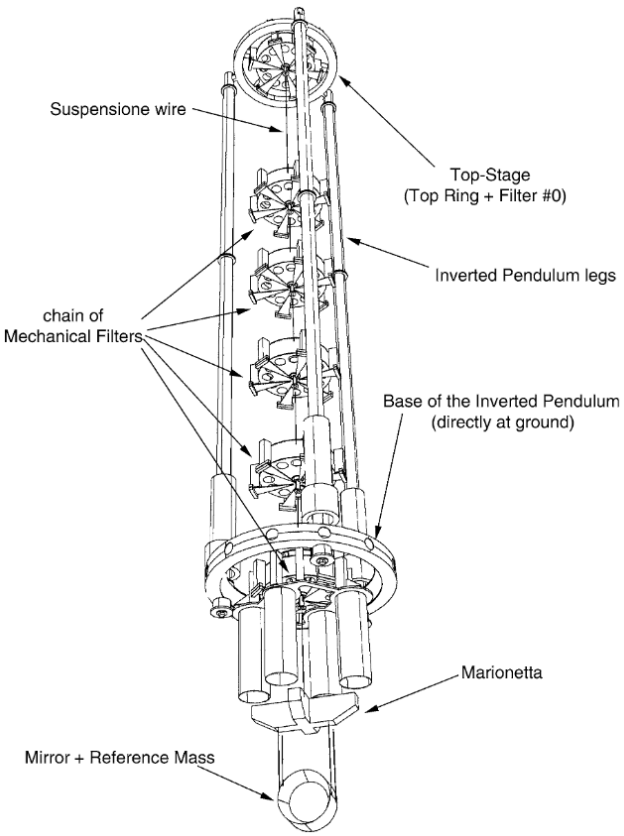

Figure 2.8: The super-attenuator used to suspend the mirror in VIRGO. The figure is retrieved from [14].

To obtain vertical attenuation, each of the five upper masses have been replaced by a mechanical filter. Those filters are drum-shaped steel elements of $70\,cm$ of diameter, $18\,cm$ of height and $100\,kg$ of mass. Triangular cantilever blade springs are used to obtain the vertical elasticity. The base of those triangles is clamped to the outer part of the filter body bottom part, while the tips can only move vertically and are attached to the steel wire linked to the next stage. The natural frequency of each filter is then $f_0 = \frac{1}{2\pi}\sqrt{\frac{k_b}{M}} \approx 1.5\,Hz$, k_B being the stiffness of the blades and M being the mass of the filter. The structure of those filter elements is shown in figure 2.9. With this, the super attenuator has its highest vertical normal mode around $7\,Hz$. To reduce it under $2\,Hz$, the different filters have been equipped with a system of magnetic anti-spring, reducing the vertical equivalent stiffness. It allowed to reach a resonance frequency of $0.4\,Hz$ for each mechanical filter. Those changes allow the effective attenuation to be present also starting from $4\,Hz$. The same logic of chain of oscillator can also be applied to the angular degrees of freedom. Then, to keep those resonant frequencies of the angular modes below $2\,Hz$, and also to minimize the coupling with the displacement modes, the filters are designed with large momenta of inertia, $I_{xx} \sim I_{yy} \sim I_{zz} \sim 10\,kg\,m^2$. Moreover, the wire used to linked two stages is attached the closest possible to the center of mass and its diameter has been reduced as much as possible to have low angular stiffness.

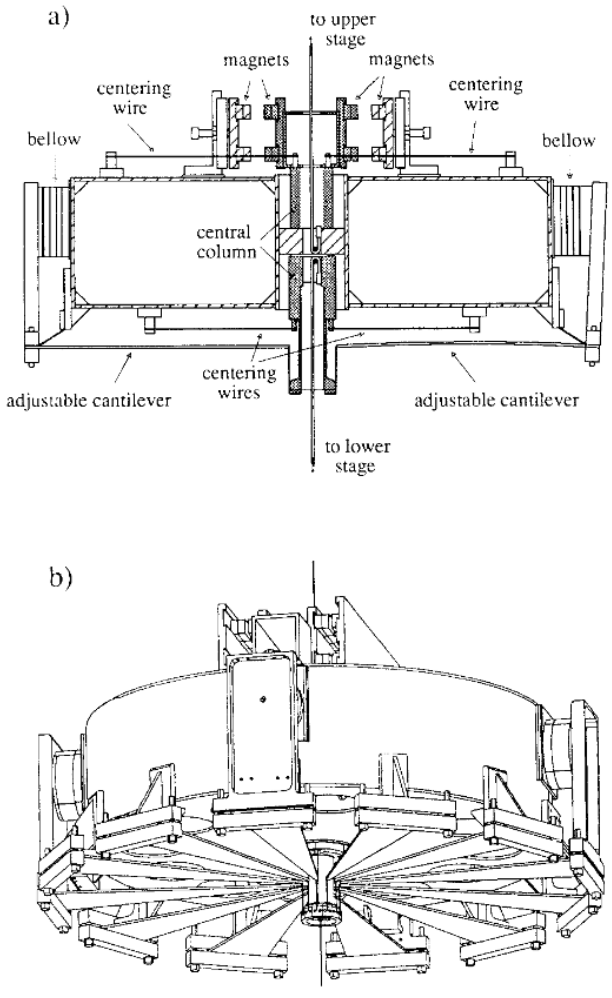

Figure 2.9: Structure of the mechanical filter used in VIRGO super attenuator, side view and perspective view. The figure is retrieved from [14].

The top stage of the multi-stage pendulum is also composed of one of those filters. It is called *Filter zero* in figure 2.8. It is connected to an outer ring, itself sustained by three legs. Each leg is $6\,m$ long and is connected to the ground thanks to a flexible joint. The structure can then be compared to an IP. Suspended to the last filter, the marionette sustains the mirror with 4 thin steel wires of $200\,\nu m$ of diameter. It allows for the control of the mirror in three degrees of freedom, the translation along the beam, the pitch and the yaw.

Since the system isolates naturally at high frequencies, active control must be implemented to damp at least its resonance peak. To do so, a set of three coils is placed on the ground to act on the top stage where magnets are mounted. The error signal required for the feedback is provided by linear variable differential transformer (LVDT) and by interferometer signals. However, the isolation is mainly due to the passive techniques.

2.7.2 Advanced LIGO

In the 1980's and 1990's, active control isolation strategies have been investigated for experiment concerning the measure of the Earth's gravitational field. It opened the way for new platforms actively controlled with inertial sensors. The first generation of gravitational wave observatories LIGO was built in the 1990s. Even with proposal to use active isolation, passive techniques were selected at that time. After some time, a proposal was made to upgrade LIGO with active techniques. That resulted in detectors much more sensitive called Advanced LIGO.

The design of the active platform and the suspension are thought to be independent, facilitating the design itself, the construction and the displacement of each part. Low frequency isolation is performed by large heavy and stiff Active Platform (AP). For high frequencies, soft suspensions mounted on the platform provide isolation to the interferometer mirror. Advanced LIGO relies only on active platform for the low frequency isolation compared to VIRGO, mainly passively isolating at higher frequency.

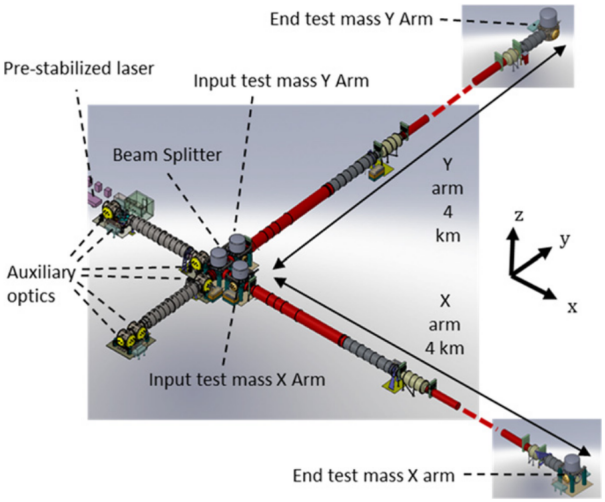

Figure 2.10: Advanced LIGO vacuum system, as presented in [15].

At each observatory, eleven hydraulic platforms, called hydraulic external pre-isolator (HEPI), are used for the pre-isolation from the outside of the vacuum chamber. This is presented in figure 2.10. Five single-stage Internal seismic isolator (ISI) are mounted on the HEPI's. They are located in the vacuum chambers called the horizontal access module (HAM). Their role is the isolation of the interferometer auxiliary optics from motion of the ground. This configuration is shown in figure 2.11.

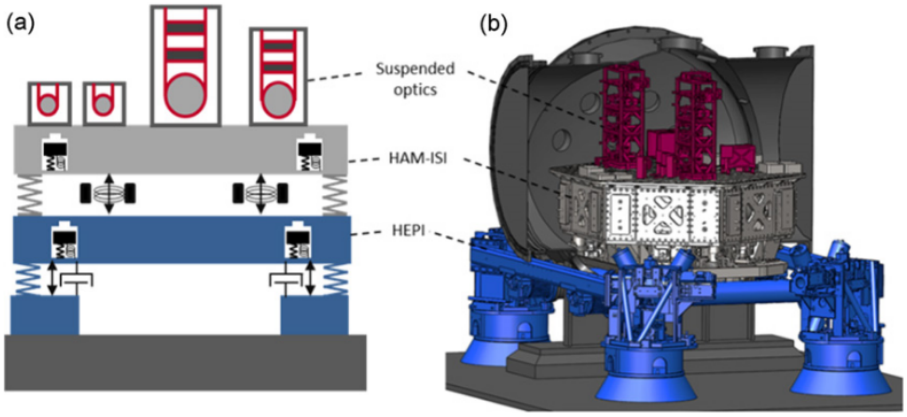

Figure 2.11: Schematic and CAD representation of the different stages of isolation build for the HAM chambers. The figure is retrieved from [15].

As can be seen, three system are build one over the other to provide five stages of seismic isolation to the auxiliary optics. The first system is the HEPI, providing one stage of isolation. The second stage of isolation is brought with the ISI system, combining active and passive techniques. This is the stage which the auxiliary optics are fixed to. Most of them are suspended to passive isolating system, up to three stage of suspension.

The second configuration is shown in figure 2.12. This three systems cascade provide up to seven stages of isolation to the core optics of the interferometer located in the Basic Symmetric Chamber (BSC). As for the first configuration, the HEPI is the first stage of isolation and ISI the second, still combining active and passive solutions but here containing two stages. From the figure, it can be seen that the test mass is suspended from a four stages pendulum.

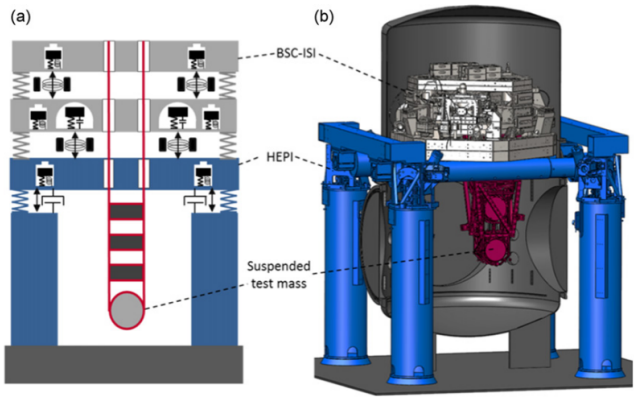

Figure 2.12: Schematic and CAD representation of the different stages of isolation build for the BSC chambers. The figure is retrieved from [15].

In both configurations, the ISI, for HAM and BSC, are build with optical tables which the interferometer component are mounted on. Those systems use low-noise inertial sensors to operate at low frequencies, down to $0.05\,Hz$. Passive isolation is assured by suspensions mounted on the platform and cascading multiple stages. It provides the necessary isolation to attenuate the ground vibration in the bandwidth of interest, above $10\,Hz$.

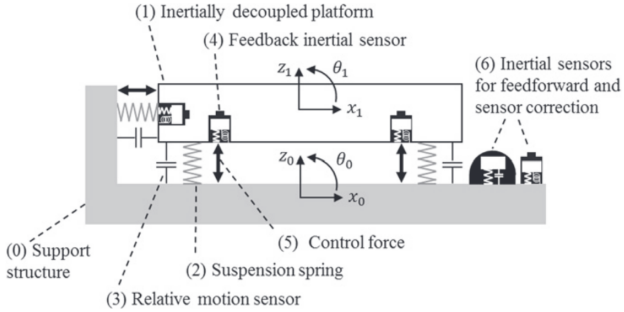

Figure 2.13: Representation of the isolation method used in Advanced LIGO for the vacuum chamber and presented in (and retrieved from) [15].

The isolation method using active and passive isolation for Advanced LIGO is summarized in figure 2.13. The grey object numbered 0 is the platform, or the previous stage, that will transmit the ground motion to the isolation platform 1, that is supported by suspension springs 2. Above its resonance frequency, the platform is passively isolated. For very low frequency, relative sensors 3 are used to measure the position compare to the support structure. Active inertial isolation is performed through feedback control using inertial sensors 4, from 0.1 Hz to 30 Hz. All the sensors are combined to provide the necessary information to the control forces 5. Additional sensors are placed on the ground, or on the previous stage platform, to provide more information and correct the information coming from the sensors mounted on the different platform or to do feedforward. The platforms are designed to minimize the cross-coupling of the different degrees of freedom in the control bandwidth. Then, each degree of freedom can be controlled in a single-input single-output (SISO) way.

All Advanced LIGO chambers are equipped with the HEPI's. Those combines quiet hydraulic actuators, inductive position sensors, geophones and ground seismometers. The latest are used to perform sensor correction. The hydraulic actuators are results of the quiet hydraulic drive technique. This allows for reaching low noise performances by operating completely in laminar flow regime, and by the absence of frictional interfaces. The sensors and actuators are common for the HAM and the BSC chambers. Only the structure, the suspended frame and the payload can vary between those chambers.

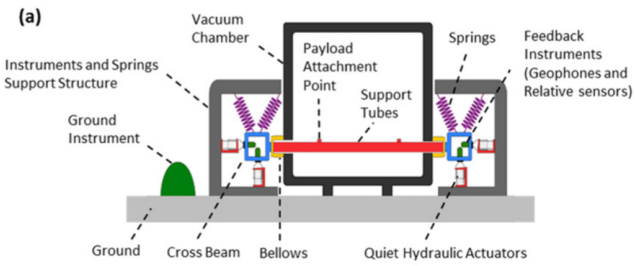

Figure 2.14: Conceptual representation of the HEPI system in the HAM chambers. The figure is retrieved from [15].

The structure is then a suspended quadrilateral rigid frame. The suspension is made with four supporting parts called the HEPI housing, at the four corners of this frame. Each includes two helical springs mounted in V shape, two inductive position sensors, two geophones and two hydraulic actuators. At the interfaces between the air and the vacuum, bellows are used.

2.7.3 KAGRA

KAGRA is an interferometric gravitational waves detector which is underground. As for the previous detectors, it relies on high performances isolators. Four different configurations of those isolators are used for the different components of the detector, type A, B, Bp and C. Those are presented in figure 2.15. It can be seen that the main optics are suspended at the lowest level of the multi-stages pendulum systems to provide the desired isolation from the ground movement and also to minimize the thermal noise generation. Those systems rely on passive isolation for high frequencies and active isolation for low frequencies, as for the previous presented detector. The passive isolation relies on the fact that the isolation from ground for a multi-stages oscillator is expressed through a transfer function decreasing as f^{-2n} above its resonance frequency, f being the frequency and n the number of stages. On the other hand, active damping is performed thanks to sensors feeding actuators both placed on each stage.

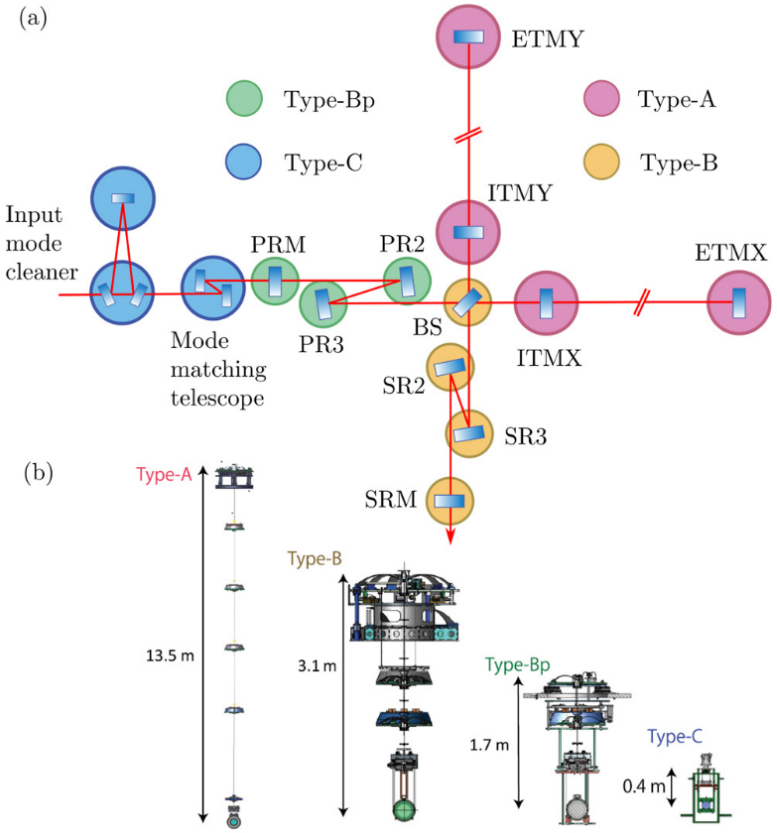

Figure 2.15: Layout of the different optical system used in KAGRA and their corresponding suspension systems, retrieved from [16]

Each configuration presented in figure 2.15 corresponds to a suspension type. Type-A suspensions are used for the most critical optic devices. They are equipped by IP for the horizontal isolation and five stages of Geometric Anti-Spring (GAS) filters for the vertical isolation. Those GAS filters are close to what are the mechanical filters used in the previous attenuators. From there, the cryogenic payload is hanging. Type-B suspensions have an IP stage, three levels of GAS filters and a room temperature payload, and it is used in the beam splitter and the three signal recycling mirror. Type-Bp suspensions have only two levels of GAS filters, but an extra recoil mass is placed at the lower one almost as a substitute for the IP. It is used for the three power recycling mirrors. Type-C suspensions are based on the design of the TAMA300 interferometer and are used for the input and output mode cleaners.

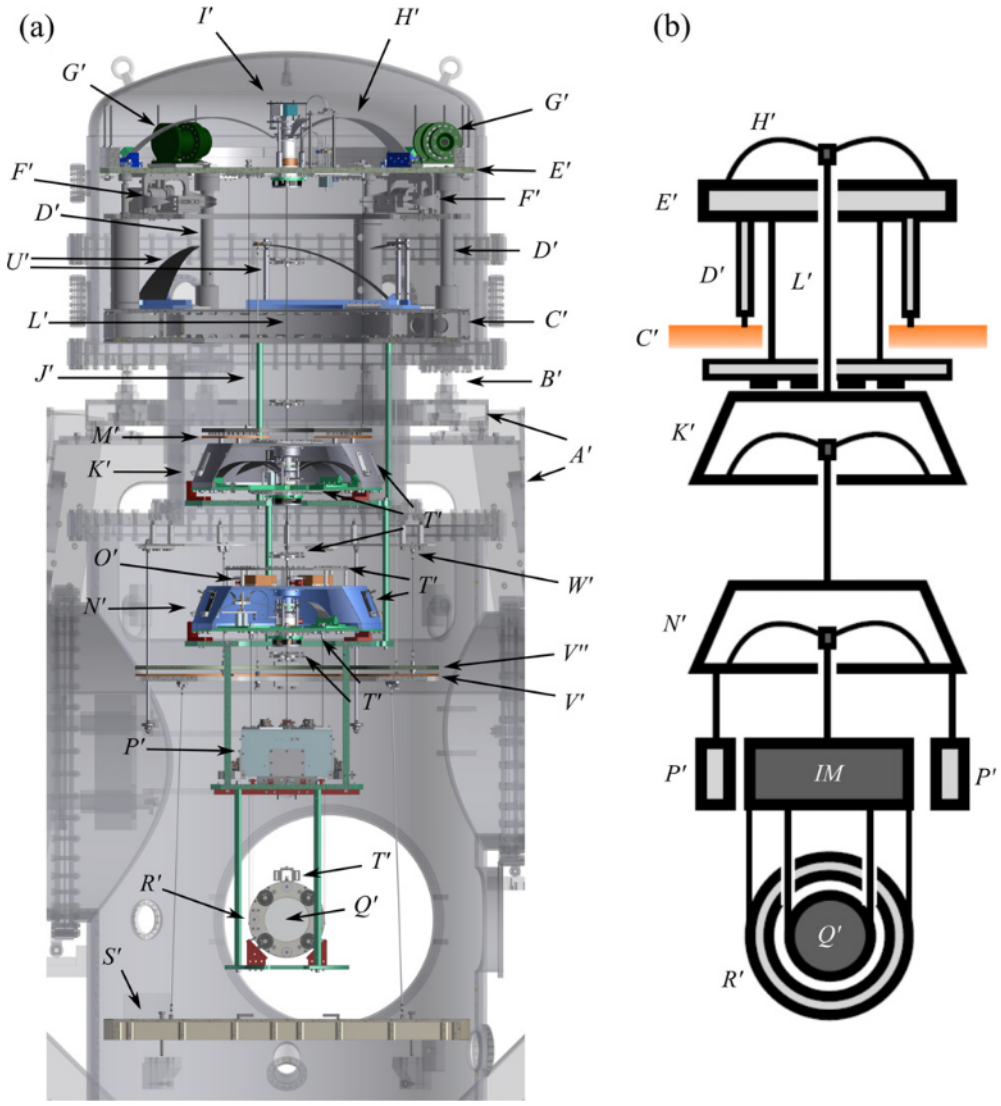

Figure 2.16: Three dimension CAD and schematic of the type-B suspension of KAGRA. A' : supporting outer frame, B': jack ,C' : IP base, D' : IP leg, E' : IP table, F' : LVDT, coil-magnet actuator and horizontal fishing rode, G' : geophone, H' : top GAS filter blades,I' : various components, J' : security structure, K' : standard GAS filter, L' : maraging steel rod, M' : magnetic damper, N' : bottom filter, O' : moving masses to adjust pitch and roll, $'P$: IRM, Q' : mirror or beam splitter, R' : RM, S' : optical table, T' : cable clamps, U' : spring blade assemblies for the optical table suspension, V' magnetic damper for the optical table suspension, V' : iron ring with magnet, W' : suspension point. The figure is retrieved from [16].

Now, the type-B suspension will be described. This will be the case for no other suspensions because of the redundancy of the different elements and structure in each suspension. The base of the IP, noted C' in figure 2.16, is supported by the outside frame thanks to three elements going through flexible bellows. This assures the mechanical decoupling between the frame and the tank. Three legs are connected to the IP base to support the Inverted Pendulum Platform (IPP), noted as E'. The resonance frequency of this structure can be tuned by adding arc-shaped weights at the edge of the table. $172\,kg$ is placed on the table for the beam splitters and $103\,kg$ for the signal recycling mirrors. Distributed all around the IPP are different assemblies, noted F', containing a LVDT displacement sensor and a coil-magnet actuator. Next to these assemblies are horizontal fishing rods and pairs of soft, opposed,

auxiliary springs. The assemblies and the LVDT's are on a motor-driven base allowing for DC position adjustment. Three geophones, noted G', are positioned around the IPP. All Those components are used to sense displacement and actuate in the transversal, yaw and longitudinal degrees of freedom.

On the described IPP is mounted the GAS filter, noted as H'. It supports the hanging chain. In the assembly noted by I', a motor-driven rotary bearing allowing for the yaw maneuver of the chain is used for adjustment. This assembly also comprises a LVDT for vertical displacement, a coil magnet-actuator and a vertical motor driven fishing rod for DC adjustment. The second GAS filter hanging from the IPP, is qualified of "standard" because it is neither fixed on the IPP nor connected to the payload at the end of the suspending chain. In the type-B suspension, only one standard filter is present, but it can be seen in figure 2.15 that it differs depending on the type of suspension. At the end of the chain, suspension rods are thinner to achieve a more convenient position of the effective bending point caused by the tension resulting from the load. Copper plates in form of ring, noted as M', are placed on the standard filter. It interacts with magnet plates hanging from IPP, giving eddy-current damping of the fundamental yaw mode and other pendulum modes. This system is called the magnetic damper (MD). This structure can then be declined for the other type of suspensions. Indeed, only elements contained in this presentation are duplicated while the global principle is the same for all the attenuators.

2.7.4 The E-TEST prototype

The goal structure of the super attenuator of the Einstein telescope (ET) is presented in figure 2.17a. The configuration of this design is based on what has been proposed for the Virgo detector and has been modified to reach the desired performances matching the requirements of ET. Indeed, the design of the Virgo attenuator is a good choice of baseline since its requirement are complying with those of ET, and moreover, its performances have been confirmed experimentally over several years. However, modifications have been applied to reduce the cross-over frequency under the $3\,Hz$ of Virgo. Maximization algorithm have been used to obtain those performances which leads to the design shown in figure 2.17a that involves six standard multi-cascaded pendulums and the payload containing the marionette and the test mirror. Multi-pendulum is efficient to passively isolate the seismic noise above the resonance frequency, the longer the pendulum, the better.

However, a prototype will be used due to space and budget constraints. This is a full scale model with a $100\,kg$ mirror as shown in figure 2.17b. It comprises an AP, an IP and a cascaded pendulum. The AP can move freely in six degrees of freedom and its vertical flexibility is parameterized thanks to three-blade springs and the horizontal flexibility is done with three flexures. The IP legs are mounted on the AP and support the IPP. The legs and the AP are linked thanks to flexures allowing displacement in rotation in the three degrees of freedom. At the upper end of the legs are attached counterweights in order to enhance the horizontal isolation of the IPP by compensating the center of percussion. Then, The GAS filter is on the IPP for vertical isolation reduction. From this filter, the marionette is hanged with a rigid wire. The cold platform is then attached to it with three elastic wires enabling the marionette to manipulate and position the payload (composed of the cold platform and the mirror) as desired. Finally, the mirror is suspended from the cold platform by cantilever spring in parallel attached to four wires. They provide vertical compliance, setting the final suspension stage frequency at $13\,Hz$.

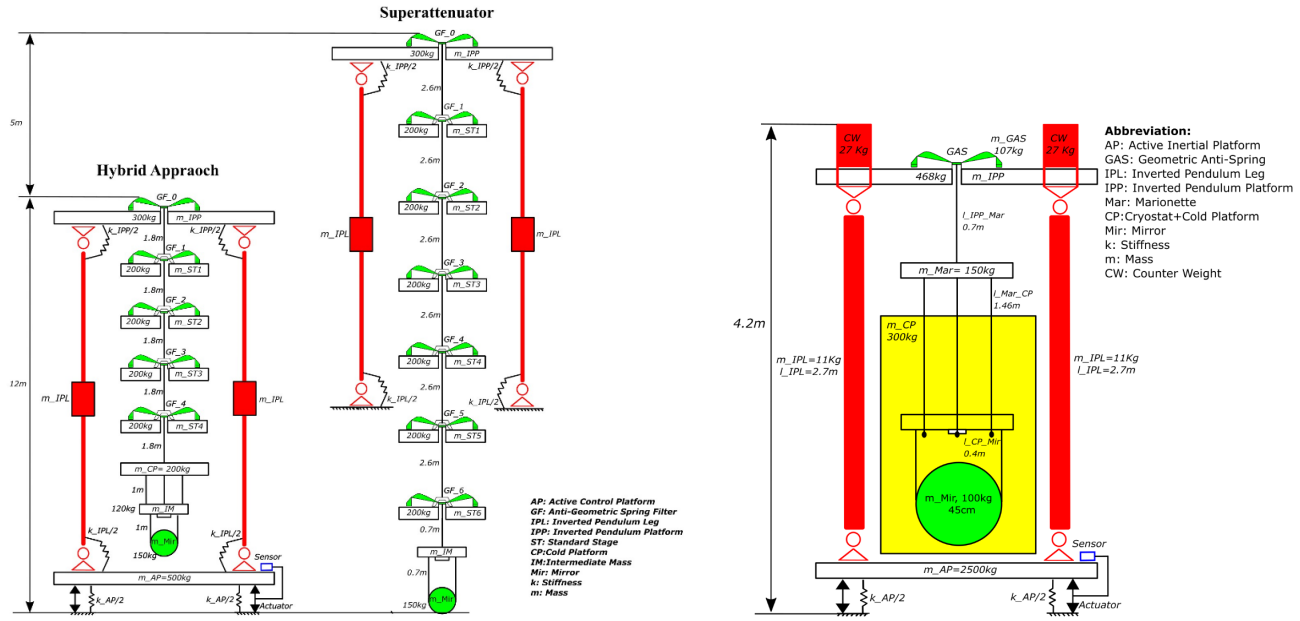

(a) Schematic of the ET super-attenuator and of the Hybrid Isolation System. This figure is retrieved from [12].

(b) Schematic of the E-TEST project prototype. The figure has been retrieved from [17].

Figure 2.17: Schematic of the supper-attenuator wanted for ET, the Hybrid Isolation System and E-TEST project prototype.

2.8 Seismic Isolation

In this section, the basics of isolation will be discussed. First, passive isolation is presented. Passive isolation does not use any external devices as actuators to isolate the system. It relies only on its characteristic to obtain the best performances. Then the active isolation is presented in the second part of this section. There, the advantage of the different types of sensor-actuator combination will be discussed. Seismic isolation is related to the ground motion. Indeed, as already discussed, the ground disturbances are one of the main limitation for the GW detectors. Those perturbations are present at low frequencies. Most of the phenomenon at higher frequencies are related to human activities. Those can be suppressed by choosing a remoted area for the implementation of the detectors.

2.8.1 Passive isolation

The system that will be used for the explanation of the different type of isolation is a one degree of freedom system. This one is composed of a mass m which is linked to the ground via a stiffness k and a damper with damping coefficient c. The mass has a translational degree of freedom x and the ground translational motion is noted w. Directly going to the Laplace domain, the equation 2.9 is describing the dynamic of the system depending on the frequencies.

$$ms^2X + cs(X - W) + k(X - W) = 0 \tag{2.9}$$

$$F = \frac{X}{W} = \frac{cs + k}{ms^2 + cs + k} \tag{2.10}$$

From this equation, the transfer function describing the transmissibility from the ground to the mass is retrieved in equation 2.10. It is then obvious that the parameters of the system have a major impact on the shape of that transmissibility. The original system has a unitary value for each of its parameters except for the damping coefficient which has the value $c = 0.1\,N/(m/s)$. Then, those different parameters will be changed in order to see their effect on the system. This is shown in figure 2.18.

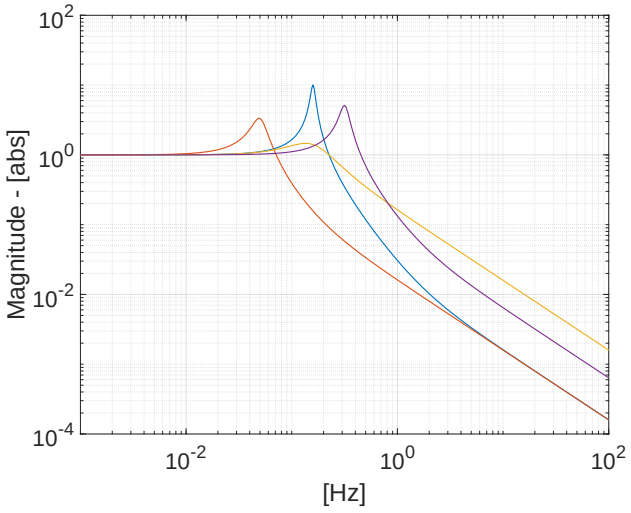

Figure 2.18: Bode plots of the passive one degree of freedom system depending on the stiffness, the damping and the mass. — is the original system. — is the system with a stiffness of $0.1\,N/m$. — is the system with a damping coefficient of $1\,N/(m/s)$. — is the system with a mass of $0.25\,kg$.

The original system is the blue curve. The peak correspond to its damped natural frequency which can be computed as $\omega_d = \omega_n\sqrt{1-\left(\frac{c}{2m\omega_n}\right)^2}$. This is the frequency at which the motion of the ground is amplified by the system since the value of the function is greater than one. Below this frequency, the value of the transfer function tends toward its frequency undependent value. In this case, this is one since $\lim_{s\to 0} F = \frac{k}{k} = 1$. This means that at low frequency, the system transmits the motion of the ground to the mass perfectly with no amplification. This is one of the reason why passive isolation is not sufficient for the seismic case since the perturbation are at low frequency.
Then, after the peak, the system naturally isolates itself from the ground since the dynamic is dominated by the squared term in the denominator $\lim_{s\to\infty} F = \frac{c}{ms}$ which gives in a logarithmic scale a $-20\,dB/dec$ slope at high frequency. The goal for isolation is then to make the natural frequency of the system as small as possible and to damp as much as possible the peak caused at that frequency.
The effect of the stiffness is shown in figure 2.18 where the orange curve corresponds to the system with its stiffness divided by ten. Since the natural frequency is computed by $\omega_n = \sqrt{\frac{k}{m}}$ the peak appears before the one of the original system. The bandwidth of the frequency where the mass is naturally isolated is then extended to lower frequencies. The yellow curve corresponds to a system with the damping ratio multiplied by ten. It can be observed that the peak is totally damped since almost no amplification is present at the natural frequency. However, the natural isolation at higher frequency is now degraded. The last curve which is purple corresponds to a system with a mass four time lighter. Due to the expression of the natural frequency, the peak is displaced to higher frequencies and the system is slightly more damped. The effects on the damping of the peak by the stiffness and the mass can be explained with the expression of the critical damping coefficient which is $c_c = \sqrt{km}$.

To conclude, it is then clear that the stiffness should be kept as low as possible for passive isolation. Also, the heavier the system is, the better. Those two parameters will act on the same elements of the shape of the isolation curves. They will make the natural frequency lower, leading to more isolation above that frequency. Moreover, the damping coefficient should be high enough to damp the amplification peak at natural frequency without degrading too much the isolation at high frequencies. Then, for better performances at lower frequencies, active isolation is needed.

2.8.2 Active isolation

To perform active isolation, an actuator and a sensor need to be placed on the system. The actuator will act on the mass by being place between the mass and the ground. This leads to the new equation 2.11 and 2.12 describing the system in the Laplace domain.

$$ms^2X + cs(X - W) + k(X - W) = f \tag{2.11}$$

$$F = \frac{X}{W} = \frac{cs + k}{ms^2 + cs + k + f} \tag{2.12}$$

The force f applied by the actuator will be proportional to the output of the sensor with a factor $-H$. If the sensor outputs the displacement of the mass, it corresponds to equation 2.13. The effects of this sensor are shown in figure 2.19 by the orange curve for $H = 100$. It can be seen that the peak is at higher frequency while its magnitude has been slightly diminished. Below this peak, the isolation has been improved. At higher frequencies, the performances are the same. The system equipped with a velocity sensor of the mass is described by equation 2.14. In the figure, it corresponds to the yellow curve. It is clear that this type of sensor allows for the damping of the resonance peak. However, away in high or lower frequencies, the performances are the same. The last type of sensor is the force sensor which measures the acceleration of the platform. It is described by the purple curve in the figure. It can be noticed that the isolation at high frequencies is greatly improved. However, the resonance peak is now less damped compared to the original system, and it is located at lower frequencies. Below this peak, the performances are the same. This latest combination of sensor-actuator is then the less well suited for seismic isolation.

$$F_{disp} = \frac{cs + k}{ms^2 + cs + k + H} \tag{2.13}$$

$$F_{vel} = \frac{cs + k}{ms^2 + (c + H)s + k} \tag{2.14}$$

$$F_f = \frac{cs + k}{(m + H)s^2 + cs + k} \tag{2.15}$$

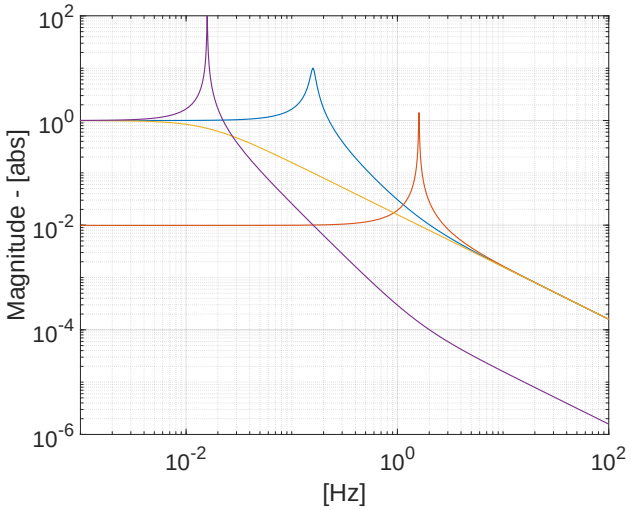

Figure 2.19: Bode plots of the active system depending on the type of sensor. — is the original system. — is the system with a displacement sensor. — is the system with a velocity sensor. — is the system with a force sensor.

Chapter 3

Control Theory

Control Theory is a field of applied mathematics which concerns methods of control applied to certain physical processes and systems. It is deeply connected to the theory of differential equations which is used to describe the different problems, systems or processes that need to be manipulated. The notion of control is related to feedback. This involves the transmission and the return of information. Control Theory is then the science which aims at modifying the environment. [18]

In this chapter, the basic concepts of control theory will be presented in order to facilitate the understanding of the method that will be applied in this paper. This will begin with explanation on the state-space form and the transfer function. The notion of Observability and Controllability will then be presented followed by the singular value decomposition. Finally, the $\mathcal{H}_\infty$ method will be explained and precision will be brought about the use of weights in the section concerning the mixed-sensitivity $\mathcal{H}_\infty$ method.

3.1 State Space

The state space analysis of control system is inherent to modern control theory. Indeed, while conventional control theory is only applicable to Linear Time Invariant (LTI) SISO system, modern control theory allows studying multiple-input multiple-output (MIMO) system that are either linear or nonlinear, time invariant or varying. This method uses the concept of state to model those complex control system.

The state variables of a dynamic system is the smallest set of variables completely determining the system behaviour at any time $t \geq t_0$ thanks to the knowledge of these variables at $t = t_0$ together with the knowledge of all inputs for $t \geq t_0$. [19] The state variables are then the set of n variables $x_1, x_2, ..., x_n$ describing the dynamic of the system, making it completely determined, if their initial value at $t = t_0$ and the value of the inputs for $t \geq t_0$ are known. One of the advantage of the method is that those states do not need to be physically measurable nor observable. However, practically, measurable quantities are preferable since those will be needed for feedback control.

The system needs elements that are able to memorize the values of inputs. Integrators serve as memory devices in continuous-time control systems. The outputs of those integrators are then the state variables of our system. The number of states is then equal to the number of integrators. Let's consider a MIMO system with n integrator, r inputs and m outputs. The n outputs of the integrators are then our state variables. Those can be defined with equations 3.1 and 3.2.

$$\mathbf{x}(t) = \begin{bmatrix} x_1(t) \\ x_2(t) \\ \cdot \\ \cdot \\ x_n(t) \end{bmatrix}, \mathbf{f}(\mathbf{x}, \mathbf{u}, t) = \begin{bmatrix} f_1(x_1, ..., x_n; u_1, ..., u_r; t) \\ f_2(x_1, ..., x_n; u_1, ..., u_r; t) \\ \cdot \\ \cdot \\ f_n(x_1, ..., x_n; u_1, ..., u_r; t) \end{bmatrix} \tag{3.1}$$

$$\mathbf{y}(t) = \begin{bmatrix} y_1(t) \\ y_2(t) \\ \cdot \\ \cdot \\ y_m(t) \end{bmatrix}, \mathbf{g}(\mathbf{x}, \mathbf{u}, t) = \begin{bmatrix} g_1(x_1, ..., x_n; u_1, ..., u_r; t) \\ g_2(x_1, ..., x_n; u_1, ..., u_r; t) \\ \cdot \\ \cdot \\ g_m(x_1, ..., x_n; u_1, ..., u_r; t) \end{bmatrix} \tag{3.2}$$

Using 3.1 and 3.2, the system can be completely described with the state equation 3.3 and the output equation 3.4. Those represent a so-called time varying system if t is explicitly involved in $\mathbf{f}$ or $\mathbf{g}$.

$$\dot{\mathbf{x}}(t) = \mathbf{f}(\mathbf{x}, \mathbf{u}, t) \tag{3.3}$$
$$\mathbf{y}(t) = \mathbf{g}(\mathbf{x}, \mathbf{u}, t) \tag{3.4}$$

Linearizing the equations about the operating state, the state 3.5 and output 3.6 equations can be retrieved.

$$\dot{\mathbf{x}}(t) = \mathbf{A}(t)\mathbf{x}(t) + \mathbf{B}(t)\mathbf{u}(t) \tag{3.5}$$
$$\mathbf{y}(t) = \mathbf{C}(t)\mathbf{x}(t) + \mathbf{D}(t)\mathbf{u}(t) \tag{3.6}$$

Where $\mathbf{A}$ is the state matrix, $\mathbf{B}$ the input matrix, $\mathbf{C}$ the output matrix and $\mathbf{D}$ the direct transmission matrix. In the case where the functions $\mathbf{f}$ and $\mathbf{g}$ do not include t explicitly, the system is called time-invariant. Then the different matrices presented are independent of time. This system can be represented with a block diagram as shown in figure 3.1.

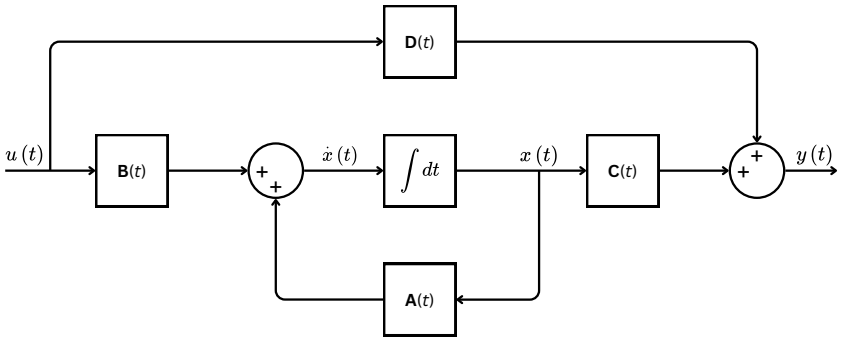

Figure 3.1: Block diagram representation of the state space of a dynamic system. $\mathbf{u}(t)$ are the inputs in function of time, $\mathbf{x}(t)$ the states and $\mathbf{y}(t)$ the outputs. $\mathbf{A}$, $\mathbf{B}$, $\mathbf{C}$ and $\mathbf{D}$ are the state space matrices, respectively the states, inputs, outputs and direct transmission matrices.

3.2 Transfer function

In control theory, Transfer Function (TF) are used to represent input-output relationships of components or systems that can be described as linear, time-invariant, differential equations. One of these systems can be written as follows

$$a_0 y^m + a_1 y^{m-1} + \cdots + a_{m-1}\dot{y} + a_m y \tag{3.7}$$
$$= b_0 u^r + b_1 u^{r-1} + \cdots + b_{r-1}\dot{u} + b_r u \tag{3.8}$$

with $m \geq r$, y being the outputs of the system and u the inputs.

The TF can then be obtained with the ratio of the Laplace transformed output over the Laplace transformed of the input, taking all initial conditions as zero.

$$\begin{aligned} TF = G(s) &= \frac{\mathcal{L}[output]}{\mathcal{L}[input]}\Big|_{zero\,initial\,conditions} \\ &= \frac{Y(s)}{X(s)} = \frac{b_0 s^r + b_1 s^{r-1} + \cdots + b_{r-1}s + b_m}{a_0 s^m + a_1 s^{m-1} + \cdots + a_{m-1}s + a_m} \end{aligned} \tag{3.9}$$

The transfer function of a system can also be expressed in state space form. Indeed, using equations 3.5 and 3.6, it can be defined in the Laplace domain as

$$s\mathbf{X}(s) = A\mathbf{X}(s) + B\mathbf{U}(s) \tag{3.10}$$
$$\mathbf{Y}(s) = C\mathbf{X}(s) + D\mathbf{U}(s) \tag{3.11}$$

Where $\mathbf{X}(s)$,$\mathbf{U}(s)$ and $\mathbf{Y}(s)$ are the Laplace transformed of the states, the inputs and the outputs. $\mathbf{X}(s)$ can be substituted from equation 3.10 to 3.11, obtaining

$$\mathbf{Y}(s) = (C(sI - A)^{-1}B + D)\mathbf{U}(s) = G(s)\mathbf{U}(s) \tag{3.12}$$

$G(s)$ is then the transfer function matrix of dimension $m \times r$ describing each input-output relation. Alternatively, the transfer function $G(s)$ can be defined as the Laplace transform of the impulse response.

$$G(s) = \int_0^\infty g(t)e^{st}dt \tag{3.13}$$

3.3 Observability and controllability

The observability and controllability are two important properties of a dynamic system. A system described by the state space equations 3.5 and 3.6 is said to be state observable if, for any time $t_n > 0$, the initial state $x(0) = x_0$ can be known from the history of inputs $u(t)$ and outputs $y(t)$ in the interval $[0, t_1]$. This can be verified using the following Observability matrix

$$\mathcal{O} = \begin{bmatrix} C \\ CA \\ \cdot \\ \cdot \\ CA^{n-1} \end{bmatrix} \tag{3.14}$$

The considered dynamic system is observable if this matrix is full column rank (rank n, the number of states).

This system is also said state controllable if, for any initial state $x(0) = x_0$, any time $t_1 > 0$ and any final state x_1, an input $u(t)$ exists such that $x(t_1) = x_1$. It can also be verified with the controllability matrix

$$\mathcal{C} = \begin{bmatrix} B & AB & A^2B & \cdots & A^{n-1}B \end{bmatrix} \tag{3.15}$$

The controllability matrix needs to be full rank n for the system to be said state controllable. However, a full rank state controllability matrix does not necessarily mean that the system is practically controllable and a non-full rank state controllability matrix does not imply a practically uncontrollable system. Indeed, some states may not be of practical importance. Those theoretical tools are still useful since it indicates if states could be deleted since they are not controllable and have no effect on the output for zero initial state. [20]

3.4 Singular Value decomposition

The Singular Value Decomposition (SVD) produces orthonormal bases of a given matrix that will be diagonalized thanks to its singular values. A is a m by n matrix, square or rectangular, with a rank r. With this method, two sets of singular vectors is obtained, u's and v's. The first is defined in the $\mathbf{R}^m$ domain and the latest in the $\mathbf{R}^n$ domain. They will constitute the columns of a m by m matrix $\mathbf{U}$ and a n by n matrix $\mathbf{V}$. This composes the four fundamental subspaces [21] :

$$\begin{aligned} u_1, \cdots, u_r &\text{ is the orthonormal basis of the column space} \\ u_{r+1}, \cdots, u_m &\text{ is the orthonormal basis of the left null space } N(A^T) \\ v_1, \cdots, v_r &\text{ is the orthonormal basis of the row space} \\ v_{r+1}, \cdots, v_n &\text{ is the orthonormal basis of the null space } N(A) \end{aligned}$$

Those subspaces allow for the diagonalization of the matrix A. Indeed, it can be expressed as : $Av_1 = \sigma_1 u_1 \cdots Av_r = \sigma_r u_r$. Since the u's and v's are orthonormal, the matrices $\mathbf{U}$ and $\mathbf{V}$ have $\mathbf{U}^T\mathbf{U} = \mathbf{I}$ and $\mathbf{V}^T\mathbf{V} = \mathbf{I}$. The equation 3.16 is then obtained.

$$A \begin{bmatrix} v_1 & \cdots & v_r \end{bmatrix}^{n\times r} = \begin{bmatrix} u_1 & \cdots & u_r \end{bmatrix}^{m\times r} \begin{bmatrix} \sigma_1 & & \\ & \ddots & \\ & & \sigma_r \end{bmatrix}^{r\times r} \tag{3.16}$$

$$AV_r = U_r\Sigma_r \tag{3.17}$$

However, there still are $n - r$ v's and $m - r$ u's being part respectively of the null space $N(A)$ and the left null space $N(A^T)$. They are orthogonal to the other u's and v's since they are part of the different null space. They can then be included in the matrix equation. Square orthogonal matrices $\mathbf{U}$ and $\mathbf{V}$ are then obtained in equation 3.18.

$$A \begin{bmatrix} v_1 & \cdots & v_r & \cdots & v_n \end{bmatrix}^{n\times n} = \begin{bmatrix} u_1 & \cdots & u_r & \cdots & u_m \end{bmatrix}^{m\times m} \begin{bmatrix} \sigma_1 & & & \\ & \ddots & & \\ & & \sigma_r & \\ & \mathbf{0}^{(m-r)\times(n-r)} & & \end{bmatrix}^{m\times n} \tag{3.18}$$

$$AV = U\Sigma \tag{3.19}$$

Due to the new dimensions of the matrices $\mathbf{U}$ and $\mathbf{V}$, the equation 3.19 can be rewritten as $A = U\Sigma V^T$, which is the singular value decomposition. The different σ_i^2 are eigenvalues of A^TA and also AA^T.

3.5 The $\mathcal{H}_\infty$ method

Before discussing the development of actual controller with $\mathcal{H}_\infty$ method, it would be useful to have a standard formulation for the problem that will be solved [20]. In this case, this is feedback control design. To do so, the configuration presented in figure 3.2 is used.

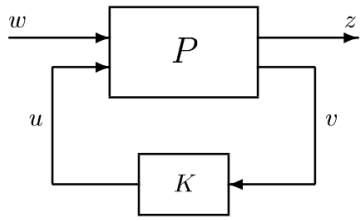

Figure 3.2: General control configuration of the optimization problem for $\mathcal{H}$ methods. The figure is retrieved from [20].

Different types of signals can be stated. The control variables are represented by u, and v are the measured variables. Those will be used for the controller using feedback method. Exogenous signals, as disturbances or commands, correspond to w and z are the error signals. Those latest are the signals that will be minimized by the method to reach the designed control objectives. The problem represented by figure 3.2 can also be written in matrix form in equation 3.20 for the generalized plant P and equation 3.21 represents the closed loop.

$$\begin{bmatrix} z \\ v \end{bmatrix} = P(s) \begin{bmatrix} w \\ u \end{bmatrix} = \begin{bmatrix} P_{11}(s) & P_{12}(s) \\ P_{21}(s) & P_{22}(s) \end{bmatrix} \begin{bmatrix} w \\ u \end{bmatrix} \tag{3.20}$$

$$u = K(s)v \tag{3.21}$$

The generalized Plant can also be expressed in state space form as shown in equation 3.22.

$$P = \left[\begin{array}{c|cc} A & B_1 & B_2 \\ \hline C_1 & D_{11} & D_{12} \\ C_2 & D_{21} & D_{22} \end{array}\right] \tag{3.22}$$

From equations 3.20 and 3.21, the closed loop transfer function from the exogenous w to the error z signals is given by the linear fractional transformation in equation 3.23. The expression of the transfer function is directly given in equation 3.24.

$$z = F_l(P, K)w \tag{3.23}$$

$$F_l(P, K) = P_{11} + P_{12}K(I - P_{22}K)^{-1}P_{21} \tag{3.24}$$

$$\|F_l(P, K)\|_\infty = max_\omega \bar{\sigma}\left(F_l(P, K)(j\omega)\right) \tag{3.25}$$

Different algorithms exist to minimize the $\mathcal{H}_\infty$ norm of the transfer function in equation 3.24. Indeed, the standard $\mathcal{H}_\infty$ optimal control problem aims at minimizing equation 3.25 which is the maximum of the singular values of the function from equation 3.24, for all frequencies. The interpretation of this optimization of the problem using the singular value is mostly helpful in the case of MIMO system. Indeed, in the case of SISO system, minimizing the maximum of the singular value of the $F_l(P, K)$ function is the same as minimizing the function response itself. However, the following assumptions are typically made [20].

$$(A, B_2, C_2) \text{ is stabilizable and detectable} \tag{3.26}$$

$$D_{12} \text{ and } D_{21} \text{ have full rank} \tag{3.27}$$

$$\begin{bmatrix} A - j\omega I & B_2 \\ C_1 & D_{12} \end{bmatrix} \text{ has full column rank for all } \omega \tag{3.28}$$

$$\begin{bmatrix} A - j\omega I & B_1 \\ C_2 & D_{21} \end{bmatrix} \text{ has full row rank for all } \omega \tag{3.29}$$

$$D_{11} = 0 \text{ and } D_{22} = 0 \tag{3.30}$$

Assumption 3.26 is simply required to assure the existence of a stabilizing controller K and assumption 3.27 ensures that the controller is proper and realizable. Assumptions 3.28 and 3.29 ensure that the optimal controller does not cancel poles and zeros on the imaginary axis which would leads to instabilities in the closed loop. Finally, assumption 3.30 is more conventional in $\mathcal{H}_2$ control algorithms. $D_{11} = 0$ makes P_{11} strictly proper. Indeed, $\mathcal{H}_2$ is the set of strictly proper and stable transfer functions. D_{22} makes P_{22} also strictly proper and simplifies procedures in $\mathcal{H}_2$ algorithms. However, these assumptions are not required for $\mathcal{H}_\infty$ methods but also simplify significantly the algorithm formulas. Additional assumptions can be made depending on the algorithm used.

$$D_{12} = \begin{bmatrix} 0 \\ I \end{bmatrix} \text{ and } D_{21} = \begin{bmatrix} 0 & I \end{bmatrix} \tag{3.31}$$

$$D_{12}^T C_1 = 0 \text{ and } B_1 D_{21}^T = 0 \tag{3.32}$$

$$(A, B_1) \text{ is stabilizable and } (A, C_1) \text{ is detectable} \tag{3.33}$$

Indeed, for simplicity, assumption 3.31 is sometimes assumed. Moreover, for additional simplification, other assumptions can be made. Assumption 3.32 is more common for $\mathcal{H}_2$ method. Assumption 3.33 can replace assumptions 3.28 and 3.29 when assumption 3.32 holds.

For the problem described in figure 3.2, considering the assumptions made, the $\mathcal{H}_\infty$ consists of the following equations to find a controller. Indeed, a stabilizing controller $K(s)$ exists such that $\|F_l(P, K)\|_\infty < \gamma$ if and only if $X_\infty > 0$ and $Y_\infty > 0$ are solution of the Riccati equations 3.34 and 3.35 as explained in [20] [22].

$$A^T X_\infty + X_\infty A + C_1^T C_1 + X_\infty(\gamma^{-2} B_1 B_1^T - B_2 B_2^T) X_\infty = 0 \tag{3.34}$$

$$\text{with } R_e\left\{\lambda_i\left[A + (\gamma^{-2} B_1 B_1^T - B_2 B_2^T) X_\infty\right]\right\} < 0, \quad \forall i$$

$$A Y_\infty + Y_\infty A^T + B_1 B_1^T + Y_\infty(\gamma^{-2} C_1^T C_1 - C_2^T C_2) Y_\infty = 0 \tag{3.35}$$

$$\text{with } R_e\left\{\lambda_i\left[A + Y_\infty(\gamma^{-2} C_1^T C_1 - C_2^T C_2)\right]\right\} < 0, \quad \forall i$$

The third condition is $\rho(X_\infty Y_\infty) < \gamma^2$. With ρ being defined as $\rho(A) = max|\lambda_i(A)|$. A stabilizing controller can then be computed as $K = F_l(K_c, Q)$ with F_l coming from equation 3.23, $Q(s)$ being any stable proper transfer function such that $\|Q\|_\infty < \gamma$ and $K_c(s)$ being given in equation 3.36.

$$K_c(s) = \left[\begin{array}{c|cc} A_\infty & -Z_\infty L_\infty & Z_\infty B_2 \\ \hline F_\infty & O & I \\ -C_2 & I & O \end{array}\right], \tag{3.36}$$

with the definition of each element given in equation 3.37 to equation 3.40.

$$F_\infty = -B_2^T X_\infty \tag{3.37}$$
$$L_\infty = -Y_\infty C_2^T \tag{3.38}$$
$$Z_\infty = (I - \gamma^{-2} Y_\infty X_\infty)^{-1} \tag{3.39}$$
$$A_\infty = A + \gamma^{-2} B_1 B_1^T X_\infty + B_2 F_\infty + Z_\infty L_\infty C_2 \tag{3.40}$$

For $Q(s) = 0$, the controller of equation 3.41 is retrieved. This is the so-called central controller which has the same number of states as the generalized plant P from the $\mathcal{H}_\infty$ problem depicted in figure 3.2.

$$K(s) = K_{c11}(s) = -Z_\infty L_\infty (sI - A_\infty)^{-1} F_\infty \tag{3.41}$$

This controller can be divided in two parts, a state estimator of the form presented in equation 3.42 and a state feedback given in equation 3.43.

$$\dot{\hat{x}} = A\hat{x} + B_1 \gamma^{-2} B_1^T X_\infty \hat{x} + B_2 u + Z_\infty L_\infty (C_2 \hat{x} - y) \tag{3.42}$$
$$u = F_\infty \hat{x} \tag{3.43}$$

The state estimator is an important feature also in other optimization techniques as Linear quadratic Gaussian (LQG). It generally has the structure given in equation 3.44. In the LQG method, it estimates the states that will be input to the controller as shown in figure 3.3. In the $\mathcal{H}_\infty$, the state estimator part of the controller has a supplementary component, which is given in equation 3.45. The term $\hat{\omega}_{worst}$ can be interpreted as the estimate of the worst case disturbance from the exogenous input.

$$\dot{\hat{x}} = A\hat{x} + Bu + K_f(y - C\hat{x}) \tag{3.44}$$
$$B_1 \gamma^{-2} B_1^T X_\infty \hat{x} = B_1 \hat{\omega}_{worst} \tag{3.45}$$

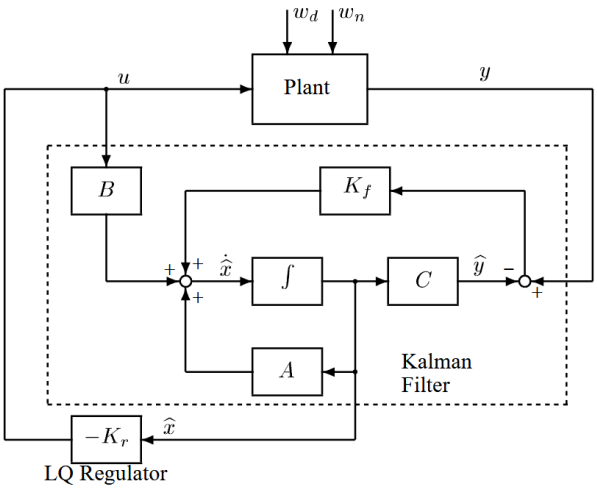

Figure 3.3: Representation in block diagram of the state estimator and the controller of the LQG method. The figure is retrieved from [20].

Those different steps can be verified while iterating on γ to find a stabilizable controller satisfying $\|F_l(P, K)\|_\infty < \gamma_{min}$. A simple bisection can be applied on γ until the value is accurate and close enough to γ_{min} which is the minimum value of γ resulting in a stabilizable controller.

3.6 Mixed-sensitivity $\mathcal{H}_\infty$ and Feedback control

The mixed-sensitivity is the transfer function problem in which the sensitivity function, alongside other closed-loop transfer functions as the complementary sensitivity function or the function KS, will be shaped. [20]

First the different transfer function that will be shaped can be defined following the system structure given in figure 3.4.

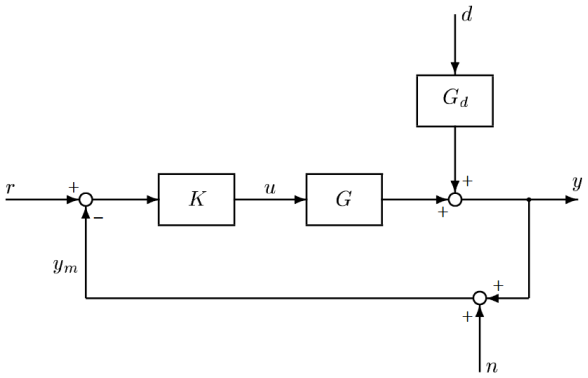

Figure 3.4: Dynamic system of one degree of freedom with feedback. The figure is retrieved from [20].

From this structure, the output $y(s)$ can be expressed thanks to the disturbance signal $d(s)$ and the plant input $u(s)$ as written in equation 3.46. Equation 3.47 is then obtained replacing the input plant $u(s)$. By isolating $y(s)$, the equation 3.48 is retrieved. The input of the plant can also be expressed as a function of $r(s)$, $n(s)$ and $d(s)$ in equation 3.49.

$$y(s) = G(s)u(s) + G_d(s)d(s) \tag{3.46}$$
$$y(s) = G(s)K(s)(r(s) - y(s) - n(s)) + G_d(s)d(s) \tag{3.47}$$
$$y(s) = T(s)r(s) + S(s)G_d(s)d(s) - T(s)n(s) \tag{3.48}$$

and,

$$u(s) = K(s)S(s)\left[r(s) - n(s) - d(s)\right] \tag{3.49}$$

The definition of the sensitivity function $S(s)$ and the complementary sensitivity function $T(s)$ are given in equation 3.50 and equation 3.51. Those are the transfer function that will be shaped alongside $K(s)S(s)$.

$$S(s) = (I + G(s)K(s))^{-1} \tag{3.50}$$
$$T(s) = (I + G(s)K(s))^{-1}G(s)K(s) \tag{3.51}$$

The figure 3.4 is an example of feedback control strategy since the output of the system is then re-injected in the controller through the error $e = r - y_m$. However, it could be considered why feedback is used at all. Indeed, feedforward could be applied by suppressing the feedback signal y_m and using the controller $K_r(s) = G^{-1}(s)$, perfectly compensating the system dynamic. Performing such an inverse is maybe not possible, this is an assumption made only for the example. Both the system G and the controller are supposed stable. Then, if the signal provided to the controller is $r - G_d d$, from equation 3.46, the output is $y = GK_r(r - G_d d) + G_d d = r$. This would be perfectly controlled. Unfortunately, the system G is never perfectly known, neither the disturbances d. The last reason to use feedback instead of feed forward is the fact that the plant G could be unstable in some cases.

Secondly, the shaping problem can be defined. A regulation problem is firstly considered. A disturbance d that is entering the plant output needs to be rejected. This type of problem is represented in figure 3.5.

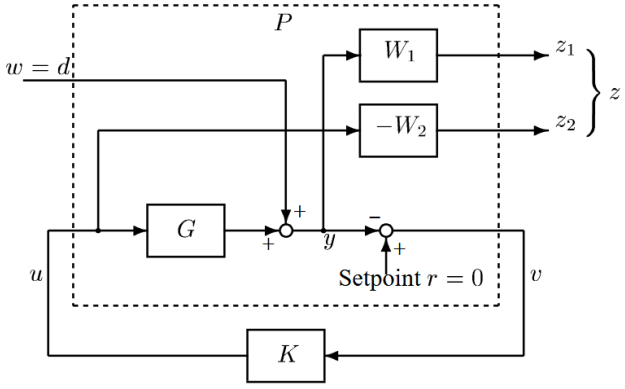

Figure 3.5: Mixed-sensitivity regulation problem, where $S(s)$ and $K(s)S(s)$ are shaped. The figure is retrieved from [20].

W_1 and W_2 are weights that can be constant or frequency dependent. They are used to shape the $S(s)$ and $K(s)S(s)$ transfer functions. It is important to include $K(s)S(s)$ to limit the size and bandwidth of the controller and the control energy used.

Generally, the disturbance d is a low frequency signal. Then, to reject it, the sensitivity function $S(s)$ needs to be made small at those low frequencies. This can be done by selecting the weight W_1 as a low pass filter with a similar bandwidth compare to the disturbance. $K(s)S(s)$ can also be shaped by selecting W_2 as a high pass filter that will limit control energy for high frequencies. Once the weights have been chosen, the problem

$$\left\| \begin{bmatrix} W_1 S \\ W_2 K S \end{bmatrix} \right\|_\infty$$

can be minimized. The weights can be matrices if the system is MIMO. Diagonal matrices are used but usually, something more complicated as a fully populated matrix is not worth the investment. The problem can be expressed in general setting as presented in figure 3.5, the disturbance being the only exogenous input. This gives the system shown in equation 3.52 where $z_1 = W_1 y = W_1 S w$ and $z_2 = -W_2 u = W_2 K S w$.

$$\begin{bmatrix} z_1 \\ z_2 \\ v \end{bmatrix} = \begin{bmatrix} P_{11} & P_{12} \\ P_{21} & P_{22} \end{bmatrix} \begin{bmatrix} w \\ u \end{bmatrix} \tag{3.52}$$

The different elements of the system are given in equation 3.53.

$$\begin{gathered} P_{11} = \begin{bmatrix} W_1 \\ 0 \end{bmatrix}, \; P_{12} = \begin{bmatrix} W_1 G \\ -W2 \end{bmatrix} \\ P_{21} = -I, \; P_{22} = -G \end{gathered} \tag{3.53}$$

The S/KS optimization can also be used for tracking problems as presented in figure 3.6. The exogenous input is now the reference $r(s)$. Then the outputs can be expressed as $z_1 = -W_1 e$ with $e = r - y$ and $z_2 = W_2 u$. However, the optimization problem is still the same.

Still for tracking problems, another sensitivity optimization problem can be useful. Indeed, the transfer function $T(s)$ can also be shaped as presented in the tracking problem shown in figure 3.7.

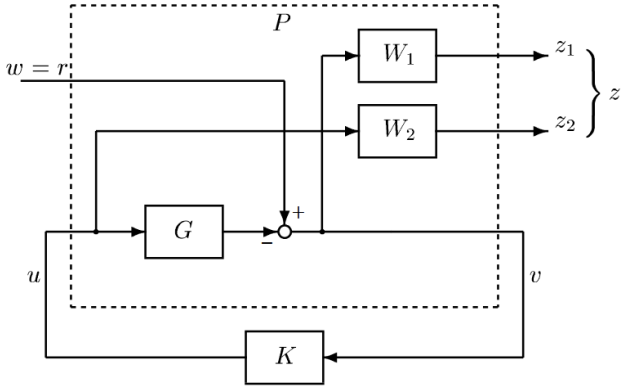

Figure 3.6: Mixed-sensitivity tracking problem, where $S(s)$ and $K(s)S(s)$ are shaped. The figure is retrieved from [20].

Shaping $T(s)$ is desirable for tracking problem, noise attenuation and can also be useful for robustness in the case of perturbation in the outputs of the plant. Then, now the problem consists of minimizing the following :

$$\left\| \begin{bmatrix} W_1 S \\ W_2 T \end{bmatrix} \right\|_\infty$$

The elements of the general plant described in equation 3.52 are now presented in equation 3.54.

$$\begin{gathered} P_{11} = \begin{bmatrix} W_1 \\ 0 \end{bmatrix},\ P_{12} = \begin{bmatrix} -W_1 G \\ W2G \end{bmatrix} \\ P_{21} = I,\ P_{22} = -G \end{gathered} \tag{3.54}$$

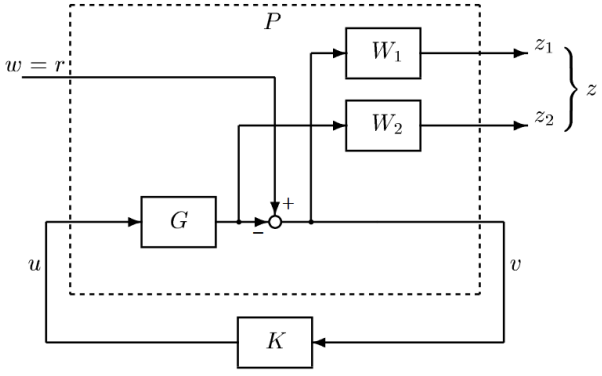

Figure 3.7: Mixed-sensitivity tracking problem, where $S(s)$ and $T(s)$ are shaped. The figure is retrieved from [20].

The $\mathcal{H}_\infty$ method can then be applied to the different system presented in this section. Indeed, the different weights used allows for the shaping of the wanted outputs for the closed loop system using the controller synthesized by $\mathcal{H}_\infty$. The advantages of the method compared to other optimization synthesis are multiple. First, its robustness is one of the main difference with the LQG method, assuring good performances even with a slightly variating system. Also, $\mathcal{H}_\infty$ can use as inputs, outputs of sensors while LQG can only use the states of the system. It is then mandatory for this latest to have access to a model of the system. Those two advantages make the $\mathcal{H}_\infty$ method prone to practical implementation since the system itself is sufficient even if it is variating slightly.

Chapter 4

Experimental set-up

In this chapter, a complete presentation of the E-TEST project prototype will be made, including all the sensors and actuators present on the structure. This is important to know the real structure that must be controlled since multiple simplified models will be presented. Indeed, the simplification of the model is necessary to attest of the efficiency of the method step by step. However, the different models must remain relevant physically to be useful in the resolution of the problem. The understanding of the prototype is then a key to attest the usefulness of each model.
A brief introduction to the project and the general prototype structure has been done in chapter 2. Here, the complete structure will be presented, beginning from the AP, passing by the IPP to the mirror. The latest is the part that must be isolated from the ground vibration and any other perturbations.

4.1 The active platform

A scheme of the AP is shown in figure 4.1, and it shows the positions of the different sensors, actuators and springs inside it.

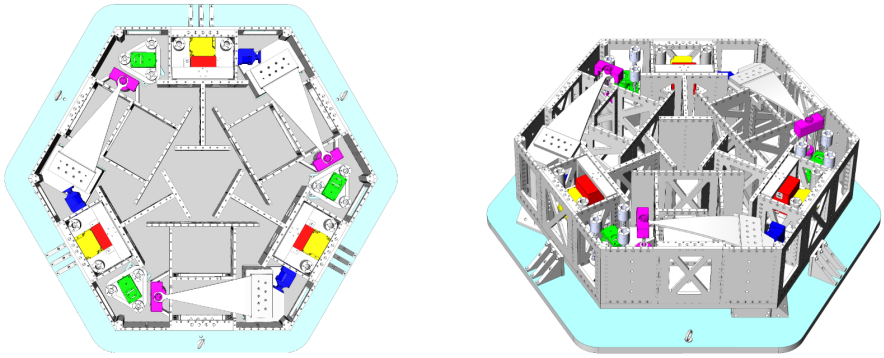

Figure 4.1: CAD representation of the AP without any top platform showing the placement of each sensor, actuator and spring. The left is a top view and the right an isometric view. Red elements are the Horizontal inertial sensor (HINS), in yellow are the Vertical inertial sensor (VINS), in green the pairs of vertical voice coil actuators and BOSEMS, in blue are the pairs of horizontal voice coil actuators and BOSEMS and finally in pink are the springs location. The figure is retrieved from [17].

Relative displacement sensors called BOSEMs are used, three measure the vertical displacement (green) and the other three measure the horizontal displacement (blue). However, relative displacement sensors will not be used for the different presented control strategies. Indeed, their use can be very difficult. This is the reason for the use of inertial sensors. In the platform, six are present. Three for

the vertical displacement in yellow and three for the horizontal in red. As can be seen in figure 4.1, They are positioned in couples, three groups of one vertical and one horizontal. The actuations of the AP is possible thanks to six voice coil actuators placed in pairs with the BOSEMS corresponding to their direction (vertical or horizontal). Each of those instruments are position with a 120° offset. Also, the actuators and sensors are in the frame of Center of Stiffness (COK), which minimizes the effects of coupling in the AP. The position of the different actuators and springs with the offset is shown in a simplified schematic in figure 4.2. The position of each element in the transverse plane is based on the practical space available and accessibility which would be needed in experimental conditions.

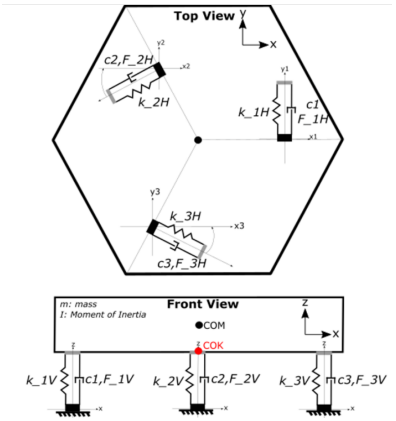

Figure 4.2: Simplified schematic of the AP from top and front view. The position of each actuator and spring is represented. The COK is shown in red in the front view. The figure is retrieved from [17].

The springs used for the stiffness of the AP have different designs depending on the direction of action. For the vertical direction, the spring design is shown in figure 4.3a. In the platform, there is a total of three of those triangular blade springs assuring vertical stiffness. The horizontal stiffness is assured by three flexure rods that are deformed as presented in figure 4.3c. Then, they are assembled as shown in figure 4.3b. The blades have one side attached to the platform and the other attached to the upper part of the flexure rods.

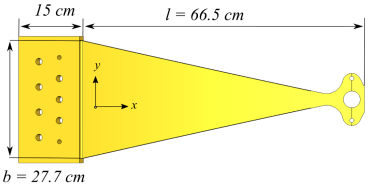

(a) Schematic of the blade spring used for the vertical stiffness of the platform.

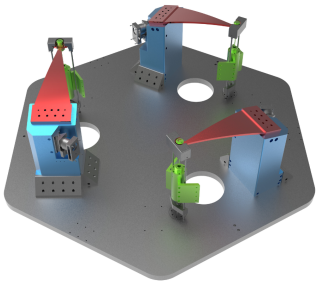

(b) CAD representation of the full springs mounted on the platform.

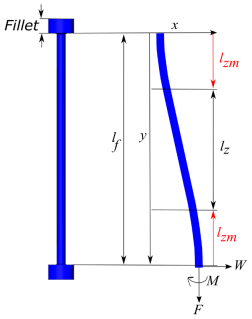

(c) Schematic of the rod spring used for the horizontal stiffness.

Figure 4.3: Different representation of the springs used in the AP in vertical and horizontal direction. The figures are retrieved from [17].

4.2 The inverted pendulum

The Inverted Pendulum (IP) is placed on the AP and is composed of the Inverted Pendulum Platform (IPP) and three Inverted pendulum leg (IPL). The legs are connected to the AP thanks to flexures assuring multi-directional flexibility. Those flexures are also present at the top of each leg to connect it to the IPP. The legs are surrounded by safety tubes assuring their protection in case of unexpected behavior of the prototype. The IPP positioned at the top of the IPL is shown in figure 4.4 in red. The yellow platform is what will serve as reference for the different actuators and sensors. This reference platform is attached to the safety tubes and is then rigidly connected to the AP, modifying its inertia. The IPP is equipped with three optical sensors and three voice coil actuators depicted in red in figure 4.4, their reference part being attached to the reference platform. Since the IPP is already isolated thanks to the AP active method, optical sensors must be used for their better resolution compared to the LVDT.

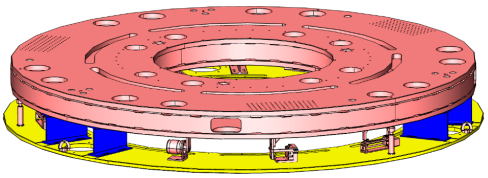

Figure 4.4: CAD representation of the IPP mounted on top of the IPL. In red is the IPP itself and in the same color but below it are represented the actuators and sensors. The yellow platform is the reference platform. The figure is retrieved from [17].

The Geometric Anti-Spring (GAS) filter is centrally placed on the IPP and is shown in figure 4.5. It has three main component, the casing which can be called the spring ring fixation and cover in red, the triangular spring blades in blue and the keystone in yellow. The filter operates feedback control thanks to a pair of vertical sensor-actuator. The sensor is an optical read-out and the actuator is a voice coil. Static positioning actuators are also equipped to the filter. Those are stepper motors.

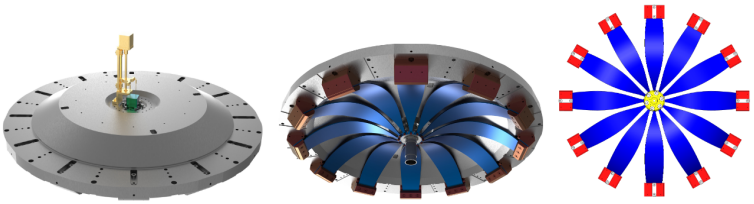

Figure 4.5: CAD representation of the GAS filter. The top view is at the left and the bottom view in the middle. The right is a schematic representation. The figure is retrieved from [17].

The marionette is suspended to the GAS filter by its body which is depicted in blue in figure 4.6. Stepper-motors are also mounted on it. The marionette is instrumented with eight coil-magnet actuators allowing for the control of the payload in angular degrees of freedom. Two optical levers can measure the orientation of the marionette with respect to the IPP.

4.3 The mirror

The Cryogenic Payload (CP) operates at cryogenic temperature and contains the silicon mirror. Its geometry is shown in figure 4.7. It serves as a test bed for the sensors detecting motion at the CP stage. Those cryogenic sensors are composed of three Horizontal inertial sensor (HINS) in red and three Vertical inertial sensor (VINS) in green. The CP also contains the structure for the protective

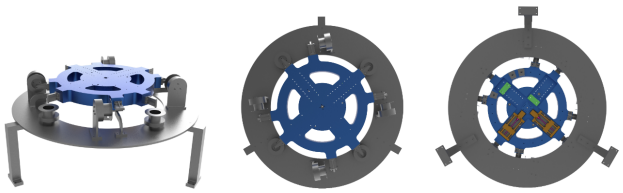

Figure 4.6: CAD representation of the marionette. At the left is the isometric view showing the body in blue and the reference frame in gray. At the middle is a bottom view and at the right is a top view showing the stepper motors in orange. The figure is retrieved from [17].

cage of the mirror, which is suspended to the CP by four silicon rods in black, parallel to four cantilever springs highlighted in green. Those latest are used to provide vertical compliance since the silicon rods are very stiff.

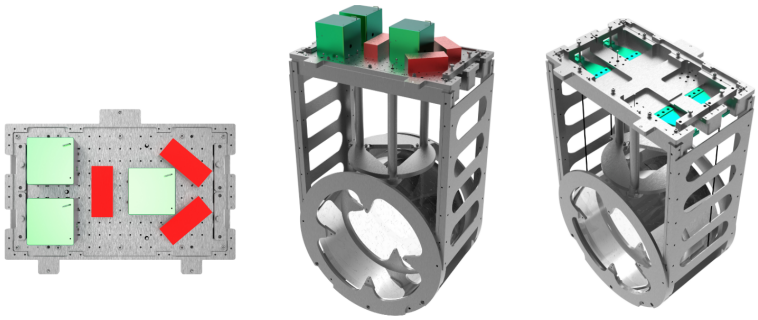

Figure 4.7: CAD representation of the CP. At the left is a top view where VINS are green and the HINS in red. Those can also be seen in the isometric view in the middle. The view at the right presents the silicon rods in black from which the mirror is suspended to the CP. The cantilever blades are also highlighted. The figure is retrieved from [17].

The CP can reach cryogenic temperature thanks to the cryostat. It is the equipment encompassing the CP without touching it, assuring thermal isolation by radiation. Since this is not linked to the mechanical isolation of the prototype, it will not be reviewed here.

Finally, the different models that will be used for the controller synthesis must be representative of the dynamic of the structure presented in this chapter. The focus will be made on the AP. Indeed, as seen here, it already contains a lot of sensors and actuators, all placed in different orientations. This already represents something complex enough to control.

Chapter 5

Preliminary controller design with low-order model

In this chapter, the development of the controller will be presented. The method used is the $\mathcal{H}_\infty$ method explained in section 3.5. The algorithm will not be explained again here.
First, the simplified model used to represent the set-up shown in chapter 4 will be defined. The models used for this thesis have been developed and provided by the Precision Mechatronics Laboratory (PML). Moreover, their inputs and outputs will be clearly stated since this is the most important for the controller, when closing the loop. Then the problem will be organized as needed for the $\mathcal{H}_\infty$ method by creating a plant outputting the right signals. Those signals will be minimized by the algorithm of the method thanks to the synthesized controller. Once the problem is set, weights need to be chosen. Those will shape the wanted signals after closing the loop on the system with the obtained controller. The principles ruling the choice of weights and their wanted effects on the system will be presented. Finally, the obtained controller will be shown and analyzed. At the end, a discussion about the use of filter will be made.

In order to synthesize a controller with any method, a plant is required. The goal is to represent the E-TEST project with enough accuracy for the method and the analysis of the results to be meaningful. However, as presented in section 2.7.4, the prototype is very complex. It would be counterproductive to directly use a full model representing the AP, IP and IPP. Indeed, by manipulating a system displaying such complex behavior, mainly due to coupling, it would be easy to miss the basics describing the controller interaction with the plant. Then, two models will be considered for this analysis. Both will focus on the AP. The first one is the 2DOF model, only considering one degree of translation and one of rotation of the AP. The model is named 2DOF because only two motions of the platform are represented. However, other degrees of freedom are taken into account, but they concern the inertial sensor or the ground. This model is the one used for this chapter and will allows for the observation of the basic principles of the method.

5.1 Controller development

This section concerns the development of the controller for the 2DOF model. This latest is first presented. Then all the steps for the production of the controller are explained.

5.1.1 Plant model

The 2DOF model represents the AP in a vertical plane. Then, the possible degrees of freedom are only the translation and the rotation in the plane considered. The representation of the system is shown in figure 5.1. The AP is modelled as a simple mass that is clamped to the ground with a pin slot joint. It

enables the translation only in one degree of freedom, here corresponding to the horizontal motion of the Center of Mass (COM) of the AP comprised in the plane noted as x, and it enables the rotation around a single axis which is in this case the axis orthogonal to the plane taken into account, resulting in the angle θ. An inertial sensor is placed at the top of the AP, allowing for the estimation of its displacement. The distance measured by this sensor is x_h and the horizontal translation is its only degree of freedom, noted x_m. Damping is assured thanks to two springs. One is horizontal with a stiffness k_1 and a damping coefficient c_1 and the other is vertical with a stiffness k_2 and a damping coefficient c_2. Control of the platform is possible due to the two actuators which are not aligned with the COM or the COK. Coupling is then expected. The numerical values of each parameter of the model are shown in table 5.1.

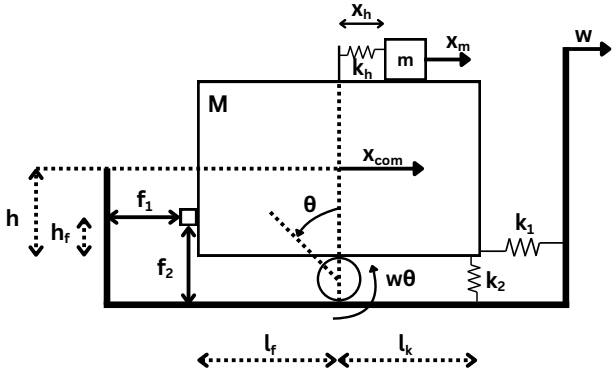

Figure 5.1: Representation of the 2DOF model provided by PML. f_1 is the horizontal actuator, f_2 the vertical actuator, x_h is the distance measured by the inertial sensor, k_1 is the stiffness of the horizontal sensor, k_2 the stiffness of the vertical sensor, and the degrees of freedom are x the translation of the center of the AP mass, θ the rotation of the AP around its clamped point to the ground, x_m the translation of the inertial sensor mass, w the ground translation and w_θ the ground rotation.

Table 5.1: Parameters Values of the 2DOF model presented in figure 5.1.

Variable	Description	Value
g	Gravitational acceleration [m/s^2]	9.81
M	Mass of AP [kg]	1921.1
m	Mass of the inertial sensor [kg]	0.3
h	Height of the COM of the AP [m]	0.1
h_f	Actuator height [m]	0.02
l_f	Horizontal distance from vertical actuator to pin-slot joint [m]	0.5
l_k	Horizontal distance from vertical stiffness to pin-slot joint [m]	0.5
k_1	Horizontal stiffness [N/m]	3.82×10^5
k_2	Vertical stiffness [N/m]	5.12×10^5
k_h	Horizontal stiffness of the inertial sensor [N/m]	1

This model can now be written in state space form as explained in section 3.1. This allows for its manipulation for computation. The different matrices are expressed in equation 5.1. As can be seen, the states of the system are the two degrees of freedom of the AP and the one of the inertial sensor, and their velocities. The outputs of the state space are the translation and rotation of the AP and the horizontal relative displacement between the inertial sensor mass and the COM of the platform. Now that the relation between inputs and outputs is clearly established, this system can also be expressed as a Transfer Function (TF) matrix

$$Y(s) = G(s)U(s)$$

$G(s)$ having three rows for the outputs and four columns for the inputs, $Y(s)$ being the outputs and $U(s)$ being the inputs, both in the Laplace domain. Moreover, $G(s)$ is stable, all his pole real parts being negative. This means that no inputs could be amplified by the system and that it will stabilize itself in a passive way.

$$A = \begin{bmatrix} 0_{3\times3} & I_{3\times3} \\ M^{-1}K & 0_{3\times3} \end{bmatrix}, \; B = \begin{bmatrix} 0_{3\times4} \\ 1 & 0 & k_1 & -Mg \\ -h_f & l_f & 0 & k_2 l_k^2 \\ 0 & 0 & 0 & 0 \end{bmatrix}$$
$$C = \begin{bmatrix} 1 & -2h & 0 & 0 & 0 & 0 \\ 0 & 1 & 0 & 0 & 0 & 0 \\ -1 & 0 & 1 & 0 & 0 & 0 \end{bmatrix}, \; x = \begin{bmatrix} x \\ \theta \\ x_m \\ \dot{x} \\ \dot{\theta} \\ \dot{x}_m \end{bmatrix}, \; y = \begin{bmatrix} x \\ \theta \\ x_h \end{bmatrix}, \; u = \begin{bmatrix} f_1 \\ f_2 \\ w \\ w_\theta \end{bmatrix} \tag{5.1}$$

The Bode plot of the transmissibility of the 2DOF model is shown in figure 5.4. It is then a transfer function matrix having as input the ground translation w and rotation w_θ and as outputs the AP translation x_1 and rotation θ. It can be observed that for each element, a roll-off is present at high frequencies. The AP is then isolating itself from any disturbances at those frequencies. Moreover, it can be seen that from the ground rotation w_θ to the AP translation x_1, the majority of the curve is below the unity line. Indeed, only the peaks are above it. Then, the coupling between the ground rotation and the platform translation is naturally not important. This is not the case for the coupling term between ground translation w and the AP rotation θ where a bigger part of the curve is above the unity line. This coupling term will then be harder to mitigate. However, the priority stays the diagonal elements of the transfer function matrix. As can be seen, for low frequencies they follow the unity line, meaning that they purely transmit the input signal to the output. Then, magnification occur before the roll-off. This will be the major concern of the isolation.

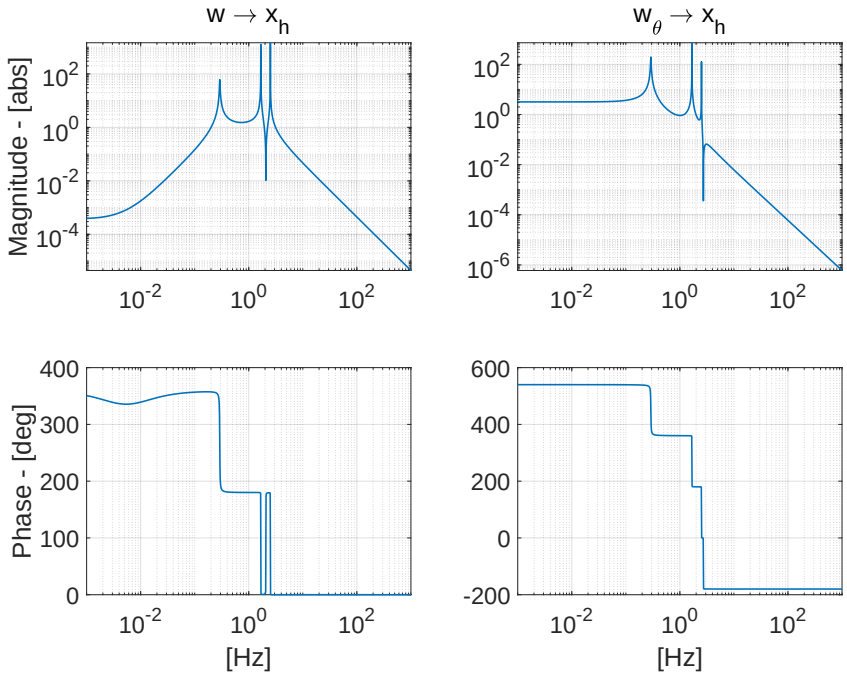

Figure 5.2: Bode plots of the transfer functions taking as inputs the ground translation w and rotation w_θ, and as outputs the inertial sensor measurement x_h.

An important dynamic of the plant is the inertial sensor as presented in figure 5.2. This sensor should output an estimation of the AP translation. As can be seen compared to figure 5.4, the estimation of the translation is good after the first resonance peak. This latest simply corresponds to the damped natural frequency of the sensor.

$$f_d = \frac{1}{2\pi}\sqrt{\frac{k_h}{m}} \cdot \sqrt{1 - \left(\frac{c_h}{2\sqrt{k_h m}}\right)^2} = 0.2906[Hz]$$

Inertial sensors provide good estimation of the translation only after their resonance peak. This can be explained by the dynamic of such a sensor. Referring to figure 5.3a, the transfer function describing the motion of the inertial sensor compared to the base it is mounted on is :

$$\frac{Y(s)}{W(s)} = \frac{-ms^2}{ms^2 + cs + k}$$

This transfer function is plotted in figure 5.3b. It is clear that it is only after the resonance peak of the mass contained in the sensor that the measurement is good.

This is one of the main features of the inertial sensors that affects the measurement that will be provided to a controller. It is then expected to have impact on it. Another significant feature of the inertial sensor is that it will provide outputs even for rotation of the AP w_θ as can be seen in figure 5.2. This coupling is due to gravity. Indeed, when the platform rotates, the mass of the inertial sensor can then slide over it.

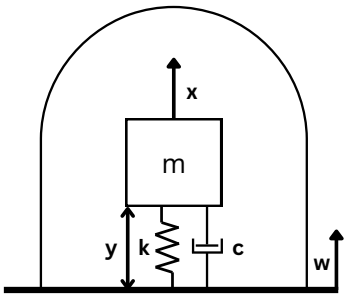

(a) Schematic of an inertial sensor measuring its base motion w. Schematic provided by PML.

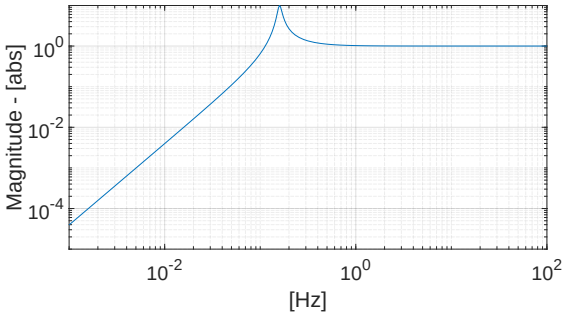

(b) Transfer functions representing the dynamic of an inertial sensor.

Figure 5.3: Schematic and transfer functions corresponding to the dynamic of an inertial sensor measuring its base motion.

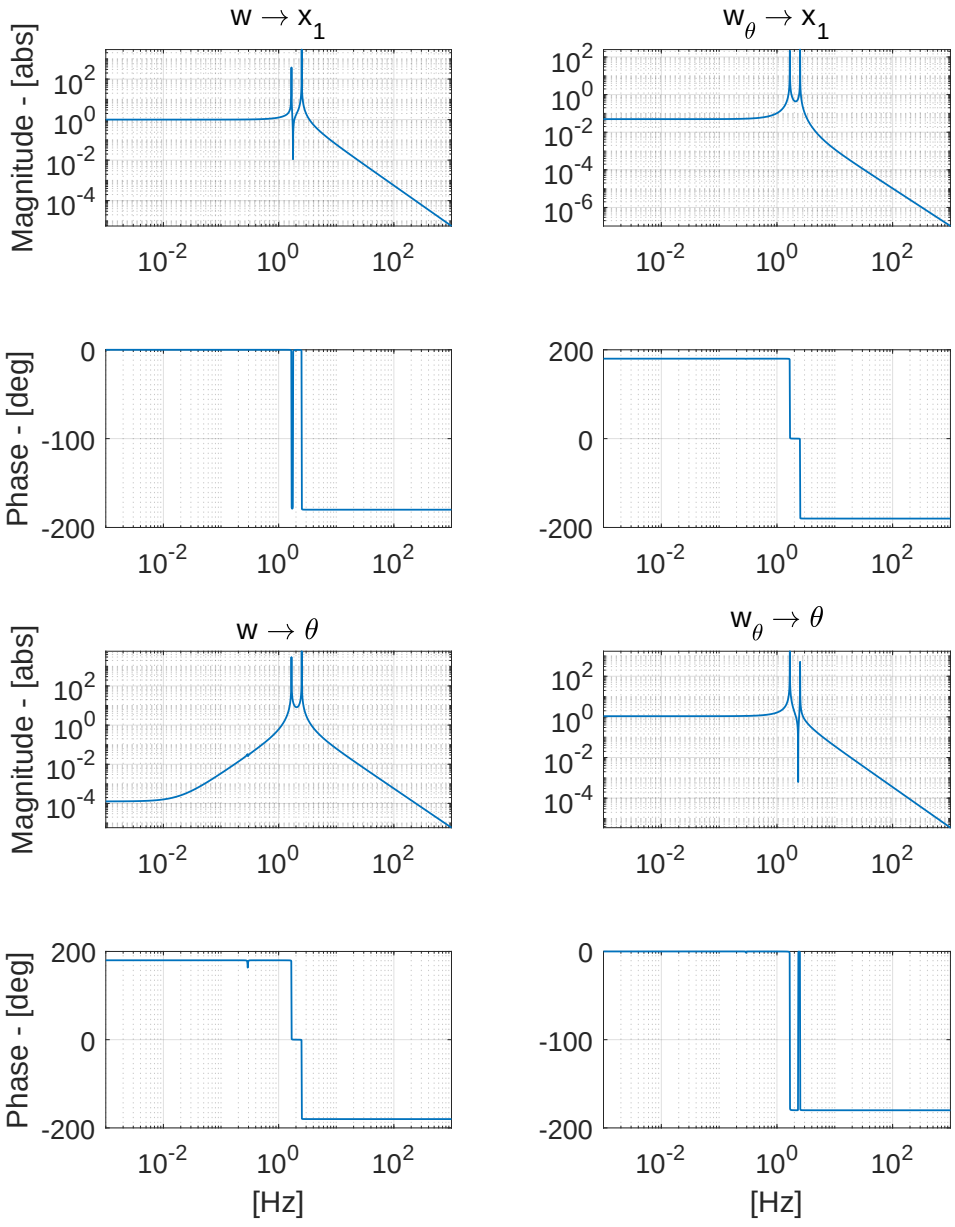

Figure 5.4: Bode plots of the transmissibility function of the 2DOF Model. Inputs are the ground translation w and rotation w_θ and the outputs are the AP translation x_1 and rotation θ.

5.1.2 Setup of the problem

In order to use the $\mathcal{H}_\infty$ method, it is necessary and good practice to well organize the system that we synthesize a controller for. This means that the inputs and outputs must be selected and classified as a perturbation (the exogenous variable), a controlling inputs, an output to be minimized (the error signal), or a sensor output used to close the loop. Those concepts are presented in section 3.5. This methodology will be applied to the system.

The choice for the different inputs is relatively straightforward. Indeed, the ground translation w and rotation w_θ being the perturbation in our problem, it can be classified as the exogenous inputs, noted $\boldsymbol{w}$. Then, the vertical and horizontal actuator are obviously the inputs that will be used to close the loop, noted $\boldsymbol{u}$. The choice for the outputs is not as simple. The objective is to minimize the movement of the AP in any direction. Then, the two degrees of freedom of the platform, x and θ, have to be in the error signals. Also concerning the translation degree of freedom of the system, the output of the sensor, noted as x_h, can be chosen as an error signal. It should assure to minimize any dynamics concerning the translation of the platform and also the coupling element. The actuator signals can also be included in the error category. This will allow for the management of the actuators effort, which is necessary to limit the aggressiveness of the controller. Indeed, an extreme controller is certainly not implementable in reality since it would need too much actuator power making it saturated. Those error signals are noted $\boldsymbol{z}$. The sensor signals will simply be the output of the inertial sensor x_h and the system output θ. The latest implies then the assumption of a perfect gyroscope. Those signals are noted $\boldsymbol{v}$. It can be noticed that some signals are duplicated. The actuators are simultaneously inputs and outputs and the sensors signals are also included in the error signals. Indeed, they also represent degrees of freedom that need to be minimized. Then, weights will be applied to those signals, following the mixed-sensitivity method presented in section 3.6. However, signals that have been modulated through weights are no more relevant as inputs for the controller. They are only relevant for the mixed-sensitivity $\mathcal{H}_\infty$ method. This is the reason for their duplicity.
This organization of the system is shown in figure 5.5, where W_{x1}, W_{f1}, W_{f2}, W_{x_h} and W_θ are respectively the weights applied to the translation of the AP, the two actuators, the inertial sensor output and the gyroscope output. The reasoning behind the choice of the weights will be explained in the following section.

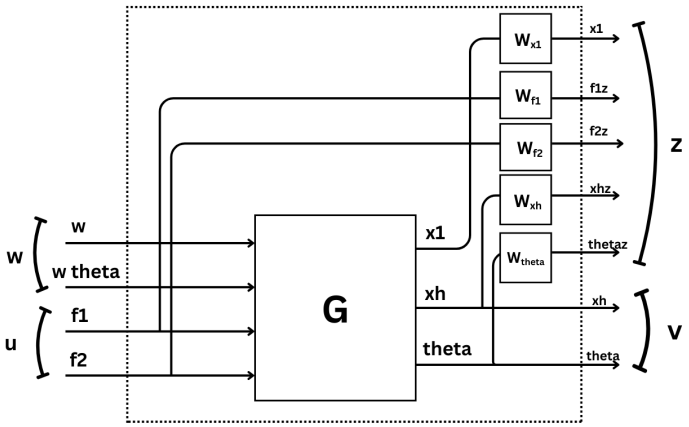

Figure 5.5: Organization of the 2DOF system in terms of inputs and outputs for the $\mathcal{H}_\infty$ method. The variables contained in $\boldsymbol{w}$ are the exogenous signals, considered as disturbances. The $\boldsymbol{z}$ variables are the error signals that will be minimized by the method. The vector $\boldsymbol{u}$ contains the control variable and the vector $\boldsymbol{v}$ the measured variables. Those will serve as outputs and inputs for the controller developed with the $\mathcal{H}_\infty$ method.

The system that will be minimized by $\mathcal{H}_\infty$ can then be written as

$$\left\| \begin{bmatrix} W_{x1}S_{\boldsymbol{w}\to x_1} & 0 \\ 0 & W_{f1} \\ 0 & W_{f2} \\ W_{x_h}S_{\boldsymbol{w}\to x_h} & 0 \\ W_\theta S_{\boldsymbol{w}\to\theta} & 0 \end{bmatrix} \right\|_\infty$$

where S is the sensitivity function, K the controller and, $\boldsymbol{w}$ are the exogenous inputs. Then, as inputs it takes w, w_θ and the actuators signals and as outputs it gives the weighted signals of x_1, f_1, f_2, x_h, and θ. For this matrix, the weights W_{f1} and W_{f2} can be considered as non-full identity matrices outputting the right actuator. Moreover, the sensitivity can simply be interpreted here as the transfer function in closed loop using the $\mathcal{H}_\infty$ controller that takes as inputs the perturbations w and w_θ and as outputs the error signals.

5.1.3 Choice of the weights

In this section, the weights applied to each selected error signal will be determined. They are selected to reflect the frequency dependence of a signal depending on its performance specifications. Those weights help to shape the open or closed loop response [23]. Those weighting transfer functions must be rational, stable and minimum-phase. As explained in section 3.5, the $\mathcal{H}_\infty$ method will optimize the relation

$$F_l(P,K) \leq \gamma$$

where $F_l(P,K)$ is the transfer function from the exogenous inputs $\boldsymbol{w}$ and the error signals $\boldsymbol{z}$ in closed loop, using the controller synthesized by the method. Then, applying weights to the error outputs of the plant can be expressed as

$$WF_l(P,K) \leq \gamma \Rightarrow F_l(P,K) \leq \frac{\gamma}{W}$$

Where W represents the weight matrix containing the weights applied to each error signal. This means that by applying the weights, the transfer function between $\boldsymbol{w}$ and $\boldsymbol{z}$ is shaped as it will be always bellow the inverse of the weight with a multiplicative factor γ. This dynamic between the weight and the obtained transfer function is shown in figure 5.6. In the same figure, the generic profile of a weight for sensitivity is presented. Indeed, it should have a large gain at low frequency. This will assure good tracking performances. In our case, the reference is zero since the AP must be isolated from the ground. At high frequency, the gain is generally low to limit the possible overshoot. Also, limiting the constraints at higher frequency permits to have a less aggressive controller in that region which is desirable. Indeed, at high frequencies, the flexible modes of the structures are present, and they could be excited by the controller if it was active this far. The weight has then the shape of a low pass filter. The inverse fits with the sensitivity function presented in the figure. The limitation of overshoot should be done cautiously since it adds damping, then limiting the response speed. The exception is the weights applied to actuator signals. They are generally chosen constant [23] as their only purpose is to limit the saturation and the sensor noise amplification in the actuator signal.
The transfer functions used as weights should remain simple. Indeed, the obtained controller with the $\mathcal{H}_\infty$ method has the same order as the system given to the method. Then, frequency dependent weights increase the order of the plant, increasing also the order of the obtained controller. If the controller must be practically implementable, its order should be kept as small as possible. Then, anything more complex than explained here is not recommended. Also, the gain of the weight is highly dependent on the signal it is applied to. The precise value of the weights is then case specific.

For the problem presented in this paper, weights will then be chosen for the error signals as shown in figure 5.5. However, for simplicity the same weight is used for the two actuators and another one for the error signal x_1 and x_h. For the latest, this is not a problem since the inertial sensor gives a good

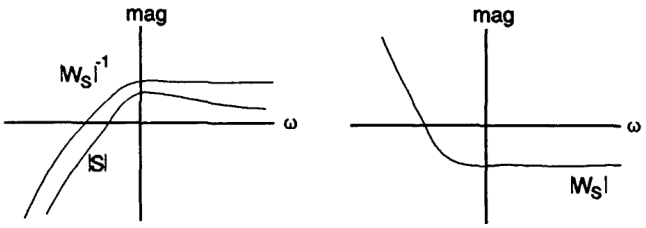

Figure 5.6: Plots of the inverse of the weight applied to the error signal and the sensitivity function (left). Plot of the weight alone (right). This figure is retrieved from [23].

estimation of the translation, the signal has then the same order of magnitude. The chosen weights are presented in figure 5.7. The weight applied to x_1 and x_h is in blue and the weight applied to θ is in orange. It can be seen that they both have the shape described in this section. Their bandwidth is the frequency at which those functions cross the unity line. This value has been made as high as possible allowing for more control. As explained, the weight applied to the actuator signals is a constant gain with a value of $4 \cdot 10^{-7}$. This can be perceived as very low. However, as explained the value of the weights being case-sensitive, this actually limit the actuators' effort. Those weights transfer functions only contain one pole and one zero, creating this low-pass filter form. They then have only one state, making them the simplest possible in order not to increase the number of states of the plant given to the $\mathcal{H}_\infty$ method. After implementing those weights to the system, the final state-space system has nine states. Six come from the original 2DOF model, and the last three corresponds to the three weighting functions, knowing that the fourth is just a constant gain containing no state.

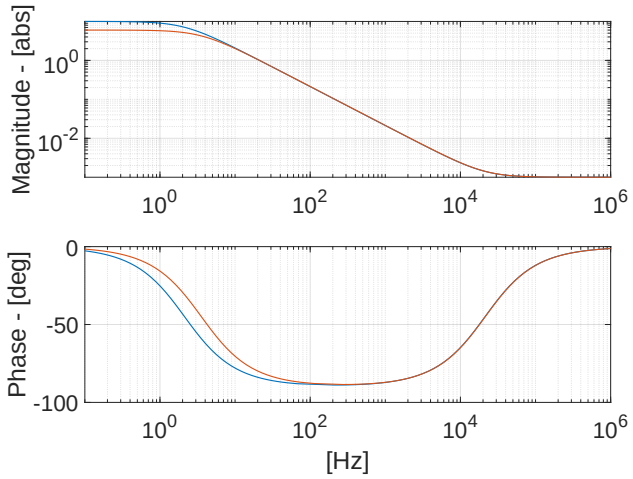

Figure 5.7: Bode plot of the weights applied to the outputs signals defined as error signals. — corresponds to the weight applied to signals x_1 and x_h, — corresponds to the weight applied to signal θ

5.1.4 Controller

The problem has been set up by arranging a generalized plant corresponding to the $\mathcal{H}_\infty$ requirements and weights have been chosen to shape the final sensitivity of the system. All of these elements can be provided to the algorithm described in section 3.5 and 3.6. The output of the method is the controller shown in blue in figure 5.8. It takes as inputs the sensors signals x_h and θ and as outputs the actuators signals f_1 and f_2. It can be observed that the low frequency part of the controller corresponds to a classic lag as can be done for a Proportional Integral Derivative (PID) controller. The most unfamiliar part is at higher frequencies where a bump in magnitude is observed. This could be expected from an

optimization problem to produce such shape of controller at higher frequency. Indeed, this allows for the control until the frequency corresponding to this bump. Afterward, the controller will not magnify any signal, pushing the gain margin as much as possible. Doing so, the $\mathcal{H}_\infty$ method ensures a high gain margin and then, as much stability as possible. This will be further discussed in section 5.2. Also, it is important to notice that each element of the controller matrix have the same order of magnitude. This means that the $\mathcal{H}_\infty$ method does not focus on the diagonal elements but rather uses all the information and signals that have been pass to it via the generalized plant and the organization of the problem.

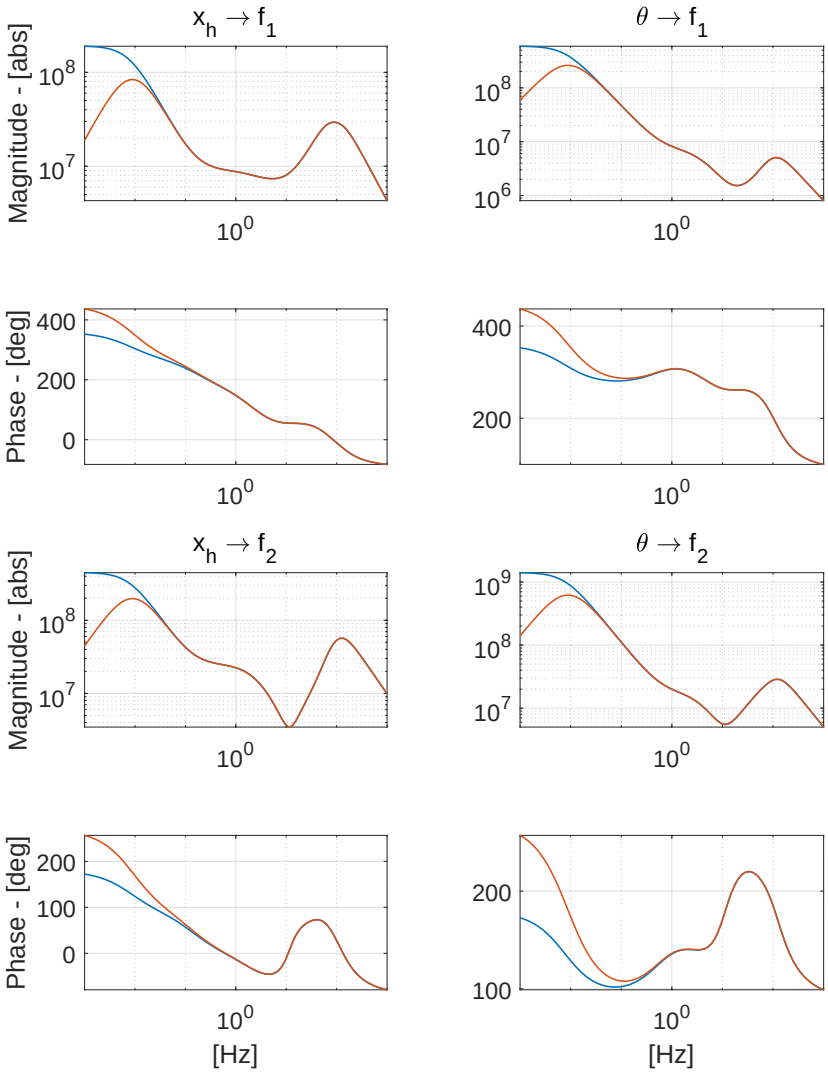

Figure 5.8: Bode plot of the transfer functions of the controller synthesized with the $\mathcal{H}_\infty$ method and the same controller with a High-Pass Filter (HPF). — is the original controller. — is the controller with the High-Pass Filter (HPF) applied.

5.1.5 Filters

The controller produced with $\mathcal{H}_\infty$ is design to perform in a certain bandwidth. It could be inappropriate to certain frequencies. Specially at low frequencies where high gain is not desirable. Indeed, it would input signal to the actuator at Direct Current (DC). Such behavior can be problematic since this could result in the saturation of the actuator voltage. This means that the actuator could not act anymore because it would have reached its limits. To prevent this problem, a High-Pass Filter (HPF) will be used. A HPF is a filter that allows for signals with frequency higher than a certain cutoff frequency and that attenuates signals with frequency lower. Different filters can be used depending on the signal that must be attenuated. Indeed, HPF of multiple order exist, the higher the order, the steeper the slope. A filter of first order will have a slope of $20dB/dec$ while a second order would have a slope of $40dB/dec$ as can be seen in figure 5.9. The choice of the filter's type is then completely depending on the slope of the controller (or the gain loop) at DC up to the cutoff frequency. Indeed, the slope of the filter must induce an ascending curve in the final controller, for the gain to be zero at DC. From section 5.1.4, it is clear that the filter should be of first order since the slope of the controller at lower frequency is higher than $-20dB/dec$. The HPF can be seen in blue in figure 5.9. In order to apply it to the controller, it can simply be multiplied to it as

$$HPF(s) \cdot K(s),$$

where $HPF(s)$ is the filter and $K(s)$ the controller. The obtained controller is illustrated in orange in figure 5.8. It is observed that a positive slope is present at low frequency, indicating that no gain is applied at DC.

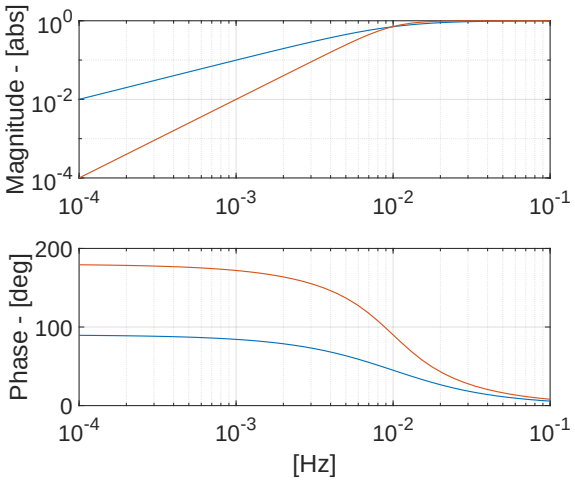

Figure 5.9: Comparison between a high pass filter of first (used for the produced controller) —— and second order —— in magnitude and phase.

5.2 Controller implementation

In this section, the results and performances of the controller developed in section 5.1 will be analyzed. First the gain loop will be shown. It will attest if the gain asked by the controller are experimentally possible. Secondly, the closed loop is shown. This directly attests the performances of the controller. A robustness study is made on the closed loop, allowing the characterization of the impact of perturbation on the system. Finally, the noise budget is done to know the resolution allowed by this controller and the impact of each perturbation on it.

5.2.1 Gain loop

The gain loop is the system with the controller applied to it without closing the loop. This is presented in figure 5.10. This allows for the observation of the gain that will be asked to the actuators to control the system experimentally. The Gain loop takes as inputs the inputs of the controller and as outputs the outputs of the system considered. This is then important to notice that some inputs of the system are not considered since only the signals useful for the control strategy are represented.

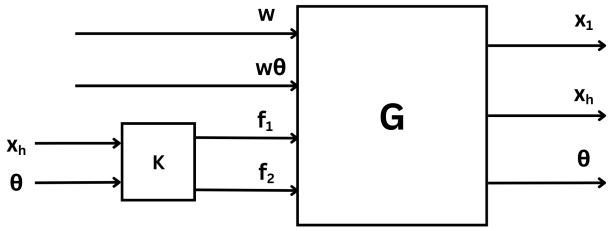

Figure 5.10: Schematic of the gain loop of the 2DOF model. K is the controller, G is the 2DOF model.

Using the controller and the 2DOF model presented in section 5.1, the obtained gain loop is shown in figure 5.12. The different peaks corresponding to the modes of the system are present. However, the most important observations are in low and high frequencies. Indeed, in the control bandwidth, the plant has been raised as would have done a PID controller. At lower frequencies, it can be observed that the gain is made steady and very high. As explained, this justifies the use of a high pass filter since this steady gain would send signals to the actuators at DC. This behavior is due to the dynamic of the inertial sensor. Indeed, it does not give a good approximation of the translational degree of freedom under its natural frequency. Then, the controller tries to compensate this dynamic by applying high gain at lower frequencies. This can be highlighted by using a model which is equipped only with inertial sensors. Then, the gyroscope is replaced by a VINS. This is closer to the real setup since no gyroscope is mounted on the AP. The goal is to see how the $\mathcal{H}_\infty$ method will compensate the lost of the information brought by the gyroscope and will use the information given by the new inertial sensor. Indeed, it should also compensate the dynamic of the added VINS.

This study is shown in figure 5.11. Controllers have been developed for the model presented in this section and a model replacing the gyroscope by a VINS. Those controllers have been made to reach the same performances in closed loop as can be seen in figure 5.11c. The open loop is blue while the closed loop of the model using the gyroscope is orange and the model using exclusively inertial sensor is yellow. First, it is important to know that the weights applied to the different outputs are not the same between each model. It was harder to reach good performances in the model using only inertial sensors, specially for the rotational direction. This makes sense since the method must reconstruct the information of the rotation only with inertial sensors in two perpendicular direction. This is obviously

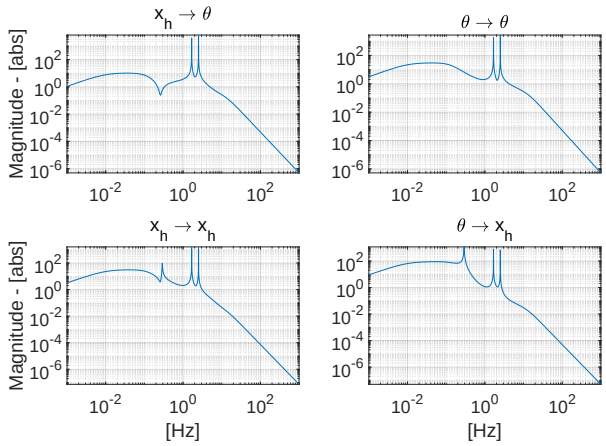

(a) Bode plots of the gain loop of the model using the gyroscope and the HINS.

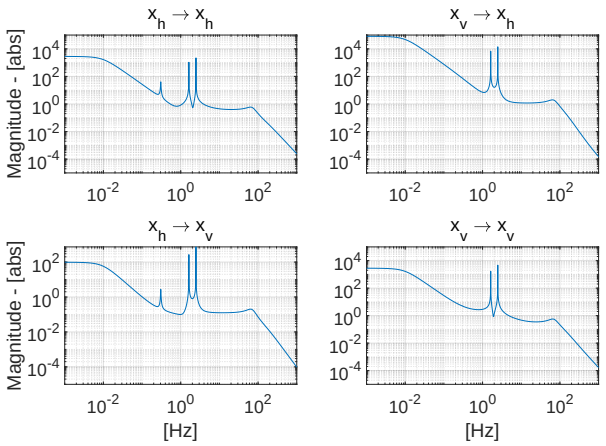

(b) Bode plots of the gain loop of the model using the HINS and the VINS.

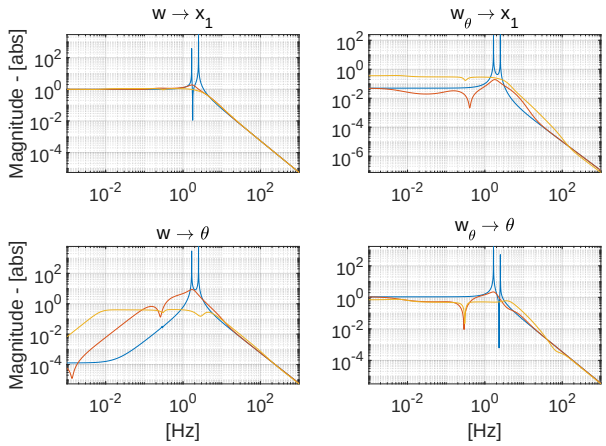

(c) Bode plots of the comparison of the closed loop of both model. — is the transmissibility open loop. — is the model with gyroscope. — is the model using only inertial sensors.

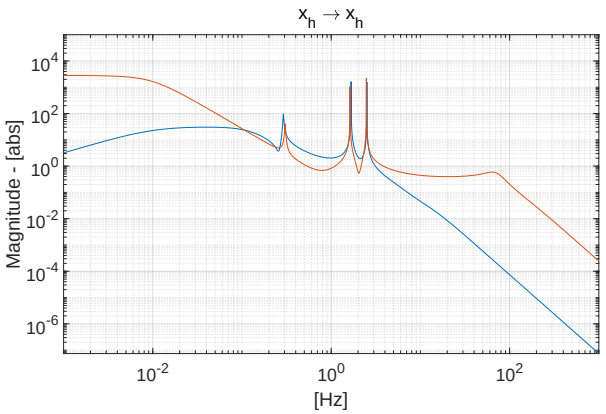

(d) Comparison of the gain loop element using only the HINS for both models. — is the gain loop of the model using gyroscope. — is the gain loop of the model using only inertial sensors.

Figure 5.11: Comparison of the performances of the $\mathcal{H}_\infty$ method depending on the model that is used. The first model uses a gyroscope and a HINS while the second model uses a HINS and a VINS.

less adapted than a gyroscope. Moreover, the vertical sensor brings limitation due to its dynamic at lower frequencies than its resonance frequency. However, even for those humble performances, it can be seen from the gain loop of both model that even more gain is applied at low frequencies when only inertial sensors are used. A proper comparison is only possible for the element of each gain loop going from the HINS to the HINS. This is shown in figure 5.11d. The conclusion about the low frequency is confirmed. For the bandwidth including the different peak, the gain loop is similar. For higher frequencies, it can be seen that a plateau is present before having the same roll-off as in the gyroscope model. From the gain loop of the model using HINS and VINS shown in figure 5.11b, it seems that this extension of the gain at higher frequencies is more related to the control bandwidth of the gain loop element coming from x_v to x_h. To conclude, it can be said that the performances and the amount of actuation needed by the $\mathcal{H}_\infty$ method is highly dependent on the way the information are given to the controller and on the limitations of this information, meaning here the dynamic of the sensor. Indeed, since no gyroscope is equipped on the second model, the method must reconstruct the information of the rotation to control those states, and it also must compensate the dynamic of the sensor.

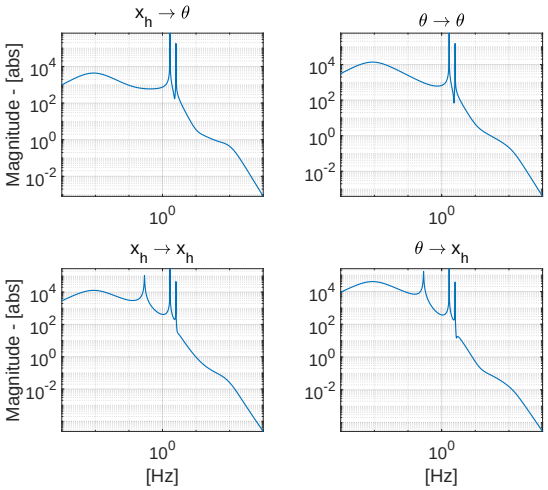

Figure 5.12: Bode plots of the gain loop corresponding to the 2DOF model as shown in schematic 5.10. It takes as inputs the inputs of the controller x_h and θ. The outputs are the one of the model used for the control loop, here it is also x_h and θ.

On the other hand, coming back to the analysis of the model using gyroscope shown in figure 5.12, at high frequency, the gain loop shows a roll-off in two steps. Indeed, two different slopes can be seen. The first one is smooth, then the second one is steeper. This is related to the bump at higher frequencies in the controller as presented in section 5.1. Indeed, the zeros and poles that are resulting in this double slope roll-off are the one creating the bump in the controller. As already explained, this then is intensifying the roll-off in order to obtain a higher gain margin. This is a result of the optimization algorithm of $\mathcal{H}_\infty$.

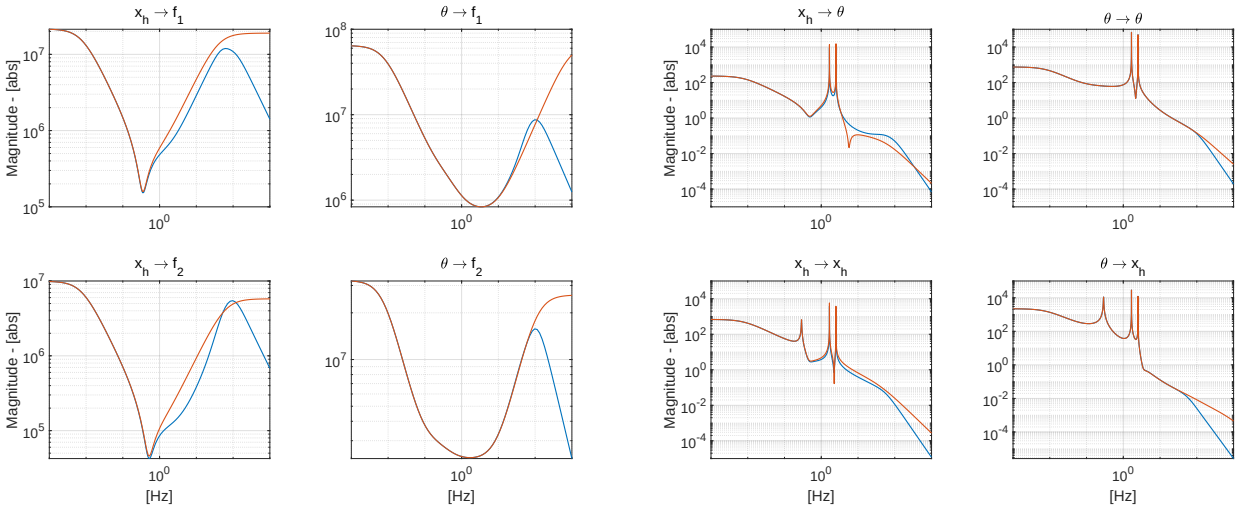

(a) Bode plots of the comparison of both controller. — is the controller obtained with $\mathcal{H}_\infty$ presenting the bump. — is the previous controller modified thanks to a lead at higher frequencies, suppressing the bump.

(b) Bode plots of the gain loops corresponding to both controller. — is the gain loop of the $\mathcal{H}_\infty$ controller. — is the gain loop corresponding to the modified controller.

Figure 5.13: Bode plots of controllers and gain loop corresponding to a controller featuring a bump at high frequencies and another one shaped like a PID at higher frequencies (lead).

This can be highlighted by modifying a controller presenting a bump to have a classic lead at high frequencies as presented in figure 5.13a. Then, the gain loops using the original and the modified controller can be compared in figure 5.13b. It can clearly be seen that the double slope roll-off becomes a simple roll-off as expected.
It is also important to understand that with fully populated controller matrix, new behaviors will come up. Indeed, when computing an element of the gain loop, it is in fact the addition of a diagonal element with a non-diagonal element as can be seen in equation 5.2. GL is the gain loop, G is the plant describing the system and K is the controller. G has f_1 and f_2 as inputs, and as outputs x_1, x_h and θ. K has x_h and θ as inputs and f_1 and f_2 as outputs. The matrix GL has then the same inputs and outputs as in figure 5.10.

$$GL = G \cdot K$$

$$\begin{bmatrix} G_{11}K_{11} + G_{12}K_{21} & \cdot \\ \vdots & \vdots \\ \cdot & G_{31}K_{12} + G_{32}K_{22} \end{bmatrix} = \begin{bmatrix} G_{11} & G_{12} \\ G_{21} & G_{22} \\ G_{31} & G_{32} \end{bmatrix} \cdot \begin{bmatrix} K_{11} & K_{12} \\ K_{21} & K_{22} \end{bmatrix} \tag{5.2}$$

Then, the poles and zeros of those two elements will be present in the calculated gain loop element. Moreover, new poles and zeros can appear due to the addition of those two elements. Indeed, when summing up two TF, the numerator and denominator of the two functions will interact $\frac{N_1}{D_1} + \frac{N_2}{D_2} = \frac{N_1 D_2 + N_2 D_1}{D_1 D_2}$. The bump studied here is one of these dynamics. The $\mathcal{H}_\infty$ method is then using all the signals provided to create a fully populated control matrix highly depending on each of its elements.

5.2.2 Closed loop

Now that the effects of the controller on the plant have been assessed thanks to the gain loop analysis, the loop will be closed on the plant thanks to the controller as shown in figure 5.14.

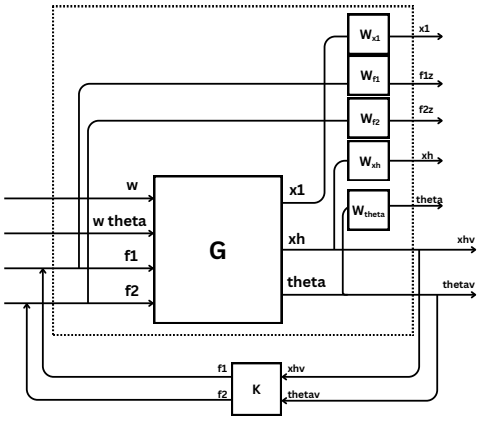

Figure 5.14: Schematic of the closed loop where G is the plant of the 2DOF model and K the controller.

Doing so, it is possible to attest of the performance of the controller in terms of isolation. Indeed, bode plots of the transmissibility can be seen in figure 5.15. The blue curve is the open loop, meaning the system without any control. The orange curve is the closed loop where the controller is used for feedback. It is clear that all elements of the transfer function matrix have been isolated thanks to the controller. However, a slight amplification can be seen for all elements around $10\,Hz$ except for the one taking as input the ground translation w and as output the AP translation x_1. Also, an amplification can be seen in the off-diagonal element taking as input the ground translation w to the AP rotation θ for the lower frequencies.

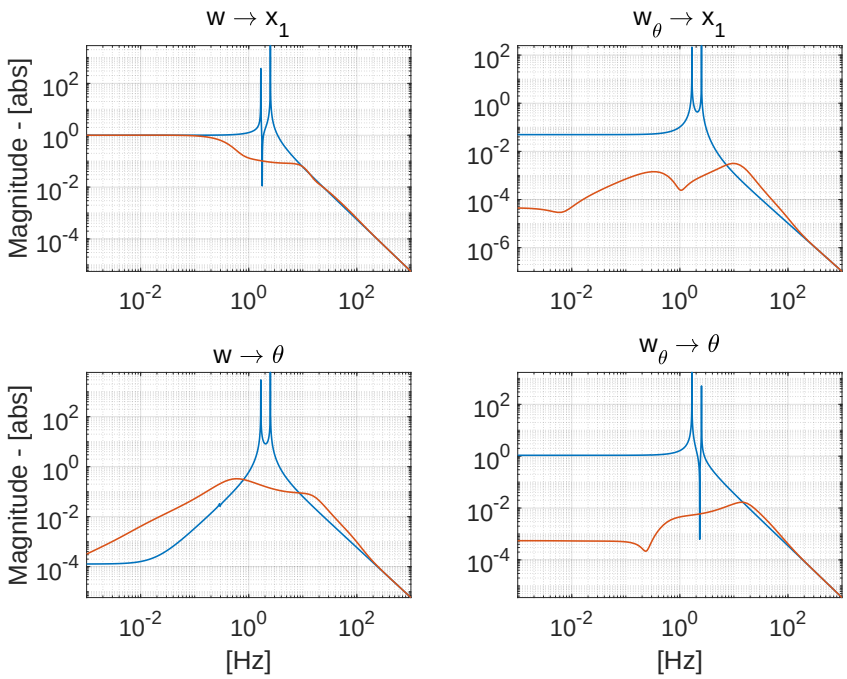

Figure 5.15: Bode plot of the 2DOF model from inputs w and w_θ to outputs x_1 and θ. —— is the open loop. —— is the closed loop.

However, the main concern is the isolation of the diagonal elements. The control bandwidth is between $10\,mHz$ and $10\,Hz$. A logarithmic ratio can then be computed as shown in equation 5.3 using the curves present in figure 5.15.

$$\text{Ratio} = 20 \cdot log\left(\frac{\text{Control off}}{\text{control on}}\right) \tag{5.3}$$

Since it is a logarithmic ratio, anything above the $0\,dB$ line means that the ratio is greater than one. Then the control off curve is above the control on meaning that there is an isolation. Anything below then means that there is an amplification. The plots of the ratio for the diagonal elements are shown in figures 5.16a and 5.16b. The first one is the isolation of the first diagonal element, from w to x_1. The latest is the isolation of the second diagonal element, from w_θ to θ. Vertical red lines are the upper and lower limit of the control bandwidth while the horizontal red line represents the two orders of magnitude of isolation wanted. For the first plot, it is clear that the requirement are not fulfilled since the isolation obtained could be qualified of sufficient only between $0.5\,Hz$ and $5\,Hz$. Indeed, the only moment where the two orders of magnitude of isolation is reached and surpassed is at the peaks. However, the second off-diagonal element isolation is very good since the two orders of magnitude are surpassed for most of the bandwidth.

The isolation is then not sufficient for each element of the transfer function matrix. However, taking into account the Gain loop, it already takes a lot of gain to reach those performances. Trying to reach better isolation for every element would require more actuation leading to a higher gain in the Gain loop. This would be unrealistic in terms of actuator performances.

The proper conduct of the $\mathcal{H}_\infty$ method can be verified using the SVD as explained in section 3.4. Then, applying this procedure on the weighted plant elaborated in section 5.1.1 (with the weights applied), the matrices shown in figure 5.18a are obtained for frequency zero. At that frequency, it can be seen that the coupling dynamic between the ground rotation w_θ and the inertial sensor x_h is the

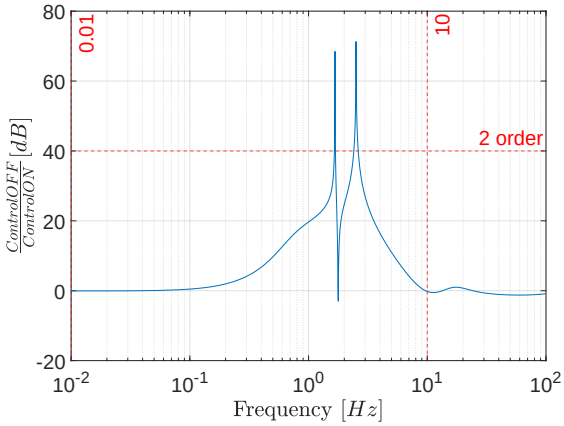

(a) Performance ratio of the 2DOF system from input w to output x_1.

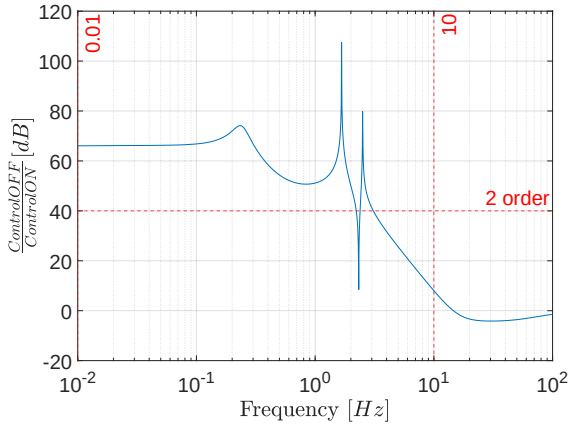

(b) Performance ratio of the 2DOF system from input w_θ to output θ.

Figure 5.16: Logarithmic Ratio of the open loop and the closed loop shown in figure 5.15. The red vertical lines are the beginning and end of the wanted control bandwidth and the red horizontal line is the desired ratio of two order of magnitude.

most important. Indeed, for the first dynamic, the first column of each matrix has to be taken. The V matrix correspond to the inputs and the U matrix to the outputs. The biggest coefficient in the matrix is then the concerned inputs or outputs. The S matrix contains in its diagonal the multiplicative factor between the signal of the inputs and the outputs. Then, the transmission between the ground w and the AP translation x_1 is of the same order of magnitude. The same decomposition can be applied to the weighted plant with the loop closed using the controller developed. The matrices are shown in figure 5.18b. Now, only the dynamic between the ground w and the AP translation x_1 is dominating while the coupling has been diminished.

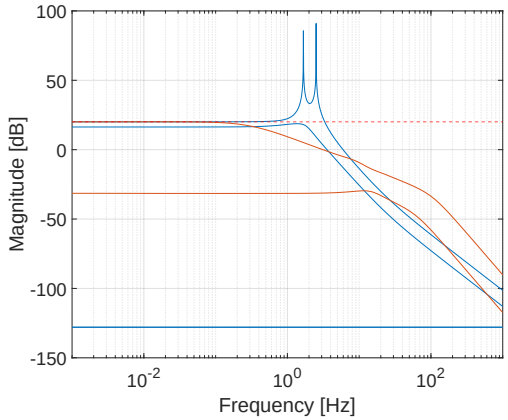

(a) Plot of the singular values depending on the frequency for the weighted plant (open and closed loop). — corresponds to the open loop. — corresponds to the closed loop. The red horizontal line corresponds to the value of gamma.

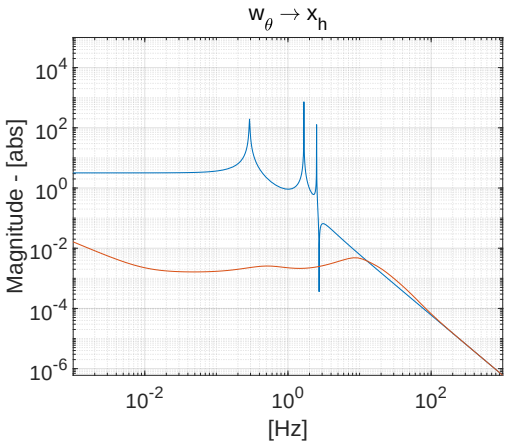

(b) Bode plot of the final closed loop from the ground rotation w_θ to the sensor output x_h compared to the open loop. — is the open loop. — is the closed loop.

Figure 5.17: Singular value decomposition in function of the frequency for the weighted plant and the weighted closed loop and bode plot of the final closed loop from the ground rotation to the sensor output.

This can be seen in figure 5.17a where the singular values are plotted depending on the frequency. The $\mathcal{H}_\infty$ method has then succeed diminishing the different dynamic of the system. It has specially decreased the coupling between the ground rotation and sensor output. This is confirmed by figure 5.17b where the open loop and closed loop of the non-weighted system of that dynamic is shown. It has also decreased the transmission of the ground to the AP in translation as it was already shown in figure 5.15.

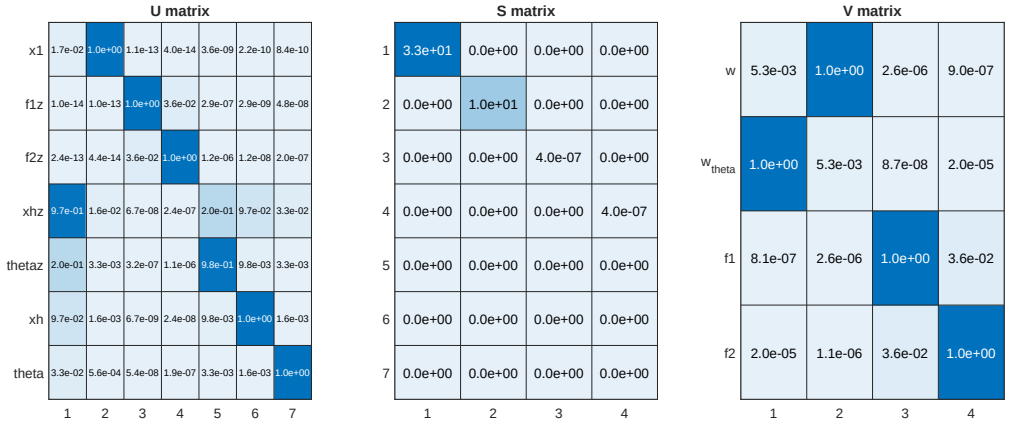

(a) SVD of the weighted plant made for the 2DOF model.

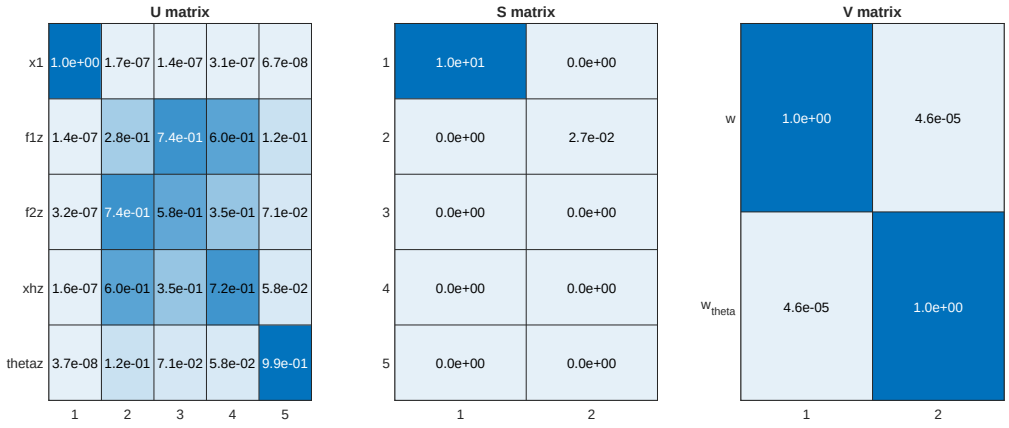

(b) SVD of the closed loop formed with the weighted plant made for the 2DOF model.

Figure 5.18: Those figures represent the matrices obtained when applying the SVD to different transfer functions. The first one is the weighted plant presented in figure 5.5 and the second one is the closed loop made with the developed controller and this weighted transfer function. The matrices correspond to the SVD matrices at the frequency zero.

5.2.3 Robustness

Now that the performances of the controller have been assessed, it is important to know if it is robust. Indeed, even by using a precise model describing the dynamic of the prototype, it is impossible to have something exactly matching the reality of the setup. Stiffness or masses could be slightly different due to the machining of the structure of the prototype, of its sensors or any other parts of the construction. The controller must then stay sufficiently effective even with variation of the parameters of the system. It should at least remain stable, to have no difficulties while applying the controller. Since the model used, which was presented in section 5.1.1, is completely analytical, it allows us for the modification of each of its parameter. It is then possible to see the effect of each parameter on the stability and the performances allowed by the controller when it is applied to the slightly modified system. Then in this model, the major parameters that must be changed are the different stiffness and the masses. The height of the position of the actuators h_f will also be modified to attest of the influence of the coupling to the robustness of the controller. All the different parameter that are selected to be modified are in the first column of the table 5.2. Each of those variables will be changed with a maximum of 10% of its nominal value. The only exception is the height of the actuators that will be changed with a maximum value being ten times its nominal values. Those variations are non-negligible. However, it is interesting to see how react the controller, even with large deviations from the nominal system.

Table 5.2: Parameters Values of the 2DOF model variation for the robustness analysis.

Variable	**Nominal value**	**Variation**	**Proportion of stable samples**
M	1921.1	10%	100%
m	0.3	10%	83.21%
k_1	3.82×10^5	10%	100%
k_2	5.12×10^5	10%	100%
k_h	1	10%	82.56%
h_f	0.02	$\times 10$	100%

Then, 10000 samples of the closed loop of the 2DOF model have been drawn with the variation shown in the table applied to the indicated parameters. In the last column of table 5.2, the percentage of stable closed loop systems over the 10000 samples is shown. It can be seen that the stability is only depending on the parameters of the sensor. Then, making those two variables change at the same time by drawing 10000 samples, it provides a proportion of 77.4% of samples that are a stable system. This can be considered as high. However, it is important to know if the performances are still comparable to the one obtained with the nominal system. The bode plots of the transmissibility for a selection of those samples is shown in figure 5.19. It can be seen that the isolation is conserved for the transmissibility between the translation of the ground w and the translation of the AP x_1. There is almost no variation between the different samples and no degradation of the closed loop as magnification is observed. The performances are also conserved in the other combination of inputs and outputs. However, variation of the gain can be observed, specially at lower frequencies. This does not provoke any amplification compared to the open-loop. This is then just a diminution of the isolation which is acceptable.

The performances are then conserved or at least not degraded a lot, but it would be interesting to know how the parameters of the inertial sensor are affecting the stability of the system. To do so, the poles of the closed loop system can be observed in function of the inertial sensors parameters. This is shown if figure 5.20, where the poles map in function of the sensor natural frequency has been computed. The sensor frequency has been computed as follows $\sqrt{\frac{k_h}{m}}$. In the figure, the red crosses are the poles of the nominal system. The rest are the poles of the different sampled closed loop system with the gradient of color corresponding to the inertial sensor frequency. Poles placed further left have been ignored for the figure. It can be seen that most of the groups of poles visible in figure 5.20 does not present a clear gradient. This signifies that the sensor is not the main dynamic corresponding to

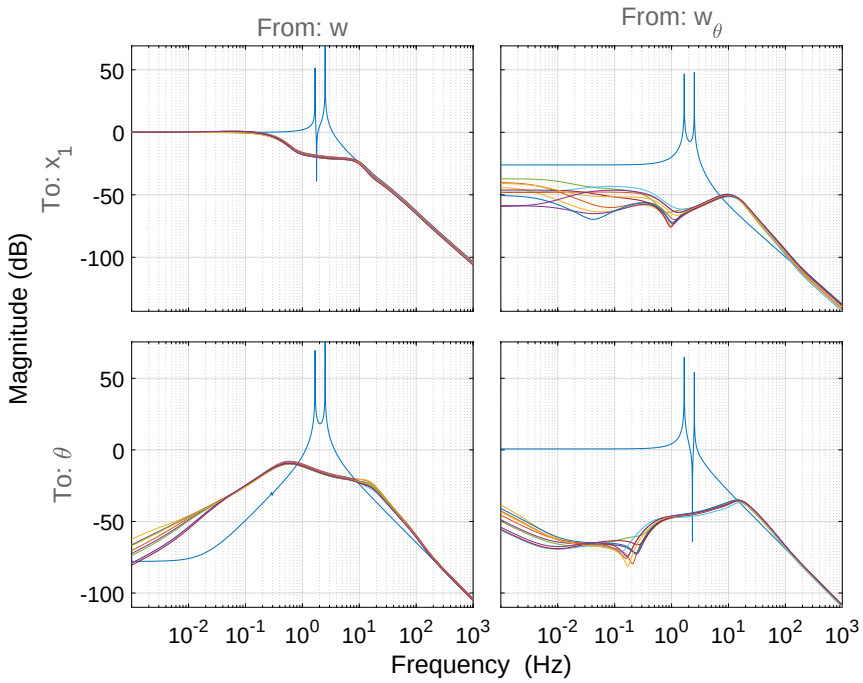

Figure 5.19: Bode plots of the transmissibility function of the 2DOF model in open loop and a set of the samples of the closed loop using the $\mathcal{H}_\infty$ controller. — is the open loop. The other curves correspond to the different closed loop sampled.

those poles. Then, the variation of the location of those poles is not linear with the frequency of the sensor. Moreover, those poles can be considered as far to the left as they do not act on the stability of the system.

The more interesting poles are located closer to the imaginary axis as can be seen in figure 5.21a which is a first close up of the previous figure. Indeed, there, the gradient depending on the frequency of the sensor is clearly visible. From this perspective, the frequency of the sensor should be as high as possible since it seems to move every pole to the left. However, in the second close up in figure 5.21b, it can be seen that the pole close to the origin would go closer to the right half plane. This same pole would also first become imaginary and then go back to the real axis to approach again the origin from the right half plane, if the frequency was diminished. It would follow one of the circle present on the figure. The other part of circle correspond to the pole which was present on the first close up. This pole would become imaginary by following the other part of the circle structure and then would go further to the right if the frequency was lower.

It can be concluded that the poles constituting a problem for the stability and the robustness are sensitive to the dynamic of the inertial sensor. The bigger its natural frequency, the more to the left are the majority of the poles. However, as seen in the second close up in figure 5.21b, for the pole which is the closer to the origin, this is not as simple. Indeed, if the frequency of the sensor is made as high as possible, this would approach it to the right. Also, if the frequency is made as small as possible, this pole, and also the others, would go to the right. Some would be in the right half plane causing instabilities. Then, a trad-off between those two tendencies must be found. Those results could be considered as counter-intuitive since as explained before with figure 5.3b, the lower the frequency of the sensor, the better is the estimation of the motion. The contradiction with the effect shown in these figures is due to the fact that the controller has been developed for the system with the nominal value of the sensor characteristics. Then, any variation from those nominal values could cause problem to

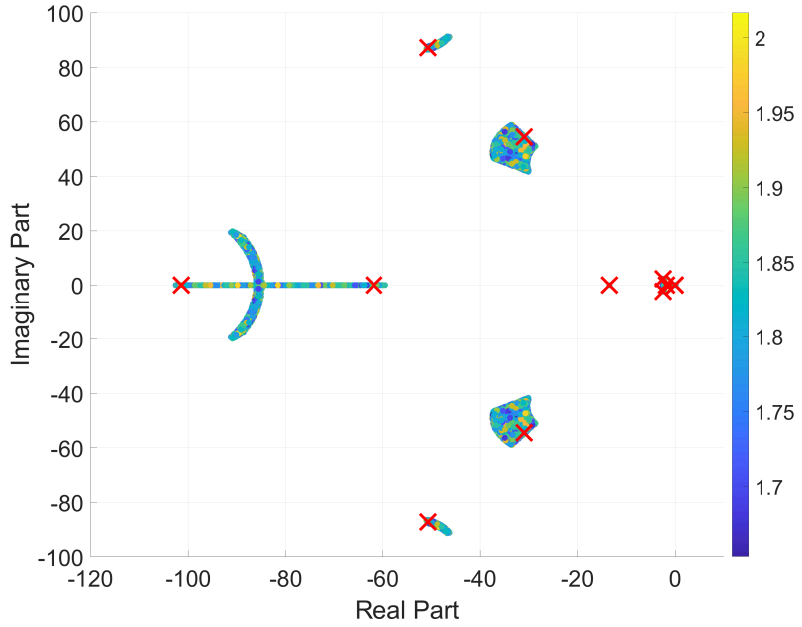

Figure 5.20: Map in the complex plane of the poles of the different closed loop samples. The natural frequency of the inertial sensor is shown with the color gradient while the poles of the nominal system are marked with red crosses. Some poles which are further left have been ignored for the figure.

the stability, which is represented by this trade-off. Moreover, all those poles concerning the stability depending on the sensor characteristic are not poles coming directly from the plant or the controller. They are a result of the closed loop dynamic which can be considered as different from the plant and the controller taken separately. Indeed, the closed loop is this transfer function $\frac{K(s)\cdot G(s)}{I+K(s)\cdot G(s)}$. This means that the poles correspond to $I + K(s) \cdot G(s)$ which can bring new dynamic due to the multiplication of the plant by the controller. Then, this confirmed that any variation from the nominal value would cause degradation of the stability since the $\mathcal{H}_\infty$ algorithm has developed the closed loop in function of the plant that has been provided. The stability will then depend on the controller which has been produced by the $\mathcal{H}_\infty$ method to obtain the final closed loop, which make the robustness of the obtained system a function of the inputs of the $\mathcal{H}_\infty$ algorithm, meaning the generalized plant and its weights.

A good practice and common technique to improve the robustness of classical systems using PID controller is to previously apply a controller to the plant in order to damp it. This would form a first loop. Then the controller is applied in a second loop. This procedure has then been applied to the system and the same complex maps have been retrieved from the final closed loop. As previously, 10000 samples have been drawn and 77.93% of those were stable. A slight augmentation of the percentage is observed. However, this could not be considered as an improvement of the robustness since this small increase could be only due to the samples that have been selected. The effects of the damping on the poles is shown in figure 5.22a. This shows directly the poles close to the origin. A first observation is that those have been shifted to the left, specially the one that was located around the origin as shown in figure 5.22b. This should provide more flexibility to the system before reaching instability. Also, the new damped system has new dynamics since a new pole can be seen. The lack of improved robustness could be due to the fact that even if the poles have been shifted, the dynamic between the sensor and the rest of the system has been changed and compensate the robustness gained by the poles that have been shifted. Also, the controller has been synthesized via the $\mathcal{H}_\infty$ method where the damped plant has been provided. The damping has maybe improved the nominal case but, as seen in section 3.5, the algorithm takes into account the worst case in the construction of the controller. This worst-case

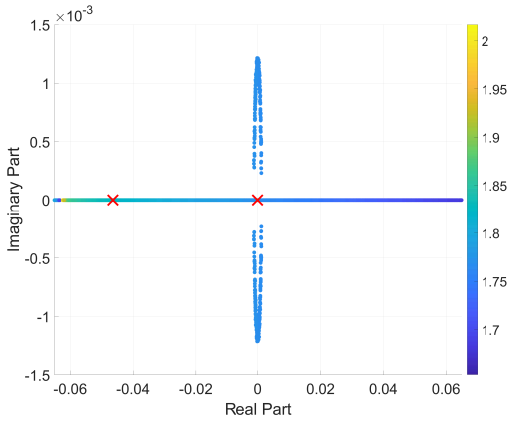

(a) First close up of the complex plane map shown in figure 5.20.

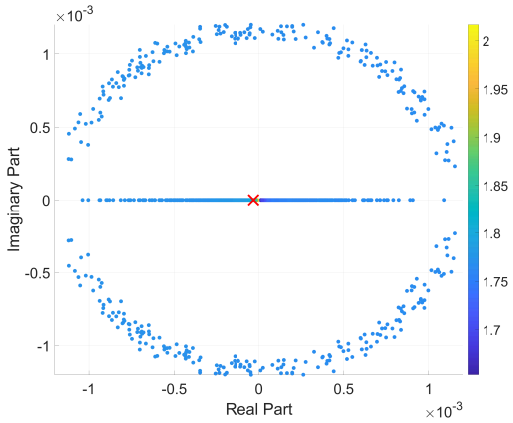

(b) Second close up of the complex plane map shown in figure 5.20.

Figure 5.21: Those figures constitute a close up of figure 5.20. The second is further zoomed.

has maybe not been changed by the damping, leading to the shaping of a similar closed loop by the method. Also, for completeness, the controller developed with the undamped system has been applied to the damped system, to bypass that dynamic with the worst case. However, no better results have been obtained.

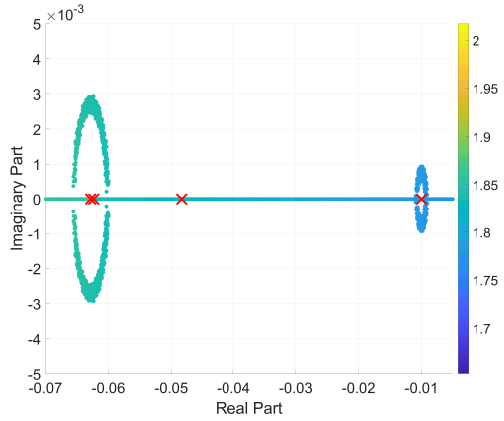

(a) First close up of the complex plane map of the damped system.

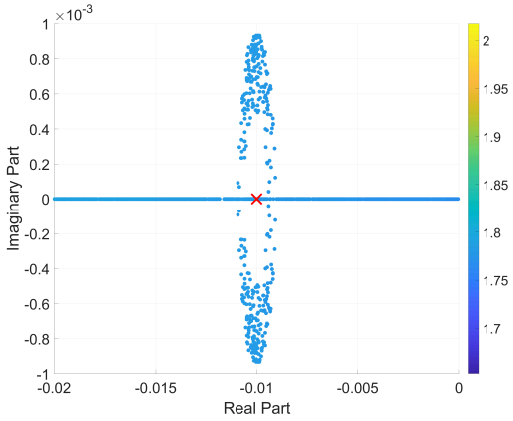

(b) Second close up of the complex plane map of the damped system.

Figure 5.22: Those figures constitute a close up of the complex plane map of the closed loop using the previously damped system.

5.2.4 Noise Budget

The noise budget is an important step of the validation of a controller. Indeed, the bode plots as shown earlier are the response of the system to each signal, but those signals are unitary. However, in reality, all signals do not have the same intensity. Budget noise will then use Amplitude Spectral Density (ASD) and Power Spectral Density (PSD) to attest the response of the system to signals with certain intensities. It also allows for the introduction of noise in sensors and actuators. This is a major dynamic to take into account since the performances are directly limited by the noise of the instruments used in the system. As can be seen in figure 5.23, noise has been introduced in the sensors and the

actuators. Assumptions have been made. Indeed, it is considered that the same noise is introduced in both sensors. The same assumption is made for the actuators. However, in the latest case, it is physical since both actuators are the same, simply oriented in a different direction. In the case of the sensors, this represents a bigger approximation since both are not of the same nature. One is an inertial sensor while the other is a gyroscope. However, this will give a good representation of the possible isolation allowed by the controller.

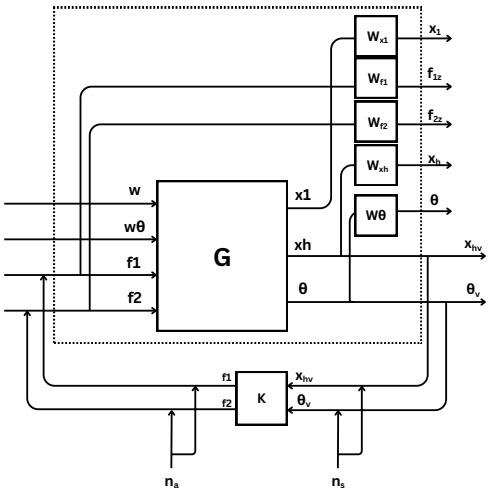

Figure 5.23: Schematic of the closed loop of the 2DOF model, including the introduction of sensor and actuator noise. The assumption is made that the noise of both sensor is the same, and the noise of both actuator is similar.

The shape of the noises also has to be defined. The inputs coming from the ground are based on measurement data. Those data form the blue PSD that can be seen in figure 5.24. For the sensor, the noise can be obtained by multiplying the signal noise by the dynamic of the inertial sensor which has been shown in figure 5.3b. Here, the ASD of the sensor has been chosen at $10^{-10}\, m/\sqrt{Hz}$ and must be multiplied by the sensor dynamic $\frac{-ms^2}{ms^2+cs+k}$ which gives the orange curve shown in figure 5.24. On the other hand, the noise from actuators can simply be considered constant with a value of $10^{-8}\, A/\sqrt{Hz}$.

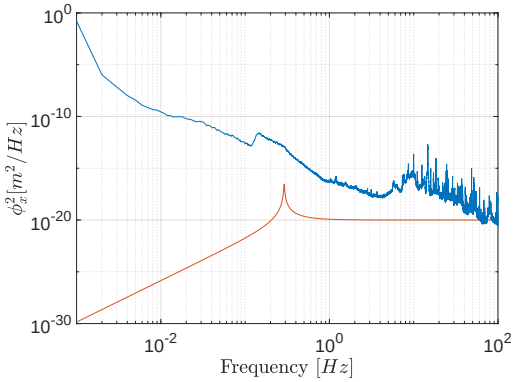

Figure 5.24: PSD of the noises of the ground and the sensors. The curve — represents the ground noise and the curve — is the dynamic of the noise of the sensor.

The PSD of the AP in translation X and in rotation Θ can then be computed using those selected noises. The calculation is shown in equation 5.4 for X and in equation 5.5 for Θ.

$$X = CL(1,3)^2 W + CL(1,4)^2 W_\theta + \left[CL(1,1)^2 + CL(1,2)^2\right] N_a + \left[(CL(1,1)K(1,1) + CL(1,2)K(2,1))^2 + (CL(1,1)K(1,2) + CL(1,2)K(2,2))^2\right] N_s \quad (5.4)$$

$$\Theta = CL(2,3)^2 W + CL(2,4)^2 W_\theta + \left[CL(2,1)^2 + CL(2,2)^2\right] N_a + \left[(CL(2,1)K(1,1) + CL(2,2)K(2,1))^2 + (CL(2,1)K(1,2) + CL(2,2)K(2,2))^2\right] N_s \quad (5.5)$$

where CL is the state-space representing the closed loop system shown in figure 5.23, K is the controller, and W, W_θ, N_a and N_s are respectively the PSD of the ground translation, ground rotation, the actuator noise and the sensor noise. Plots of the PSD can then be seen for both direction in figure 5.25a and 5.25b. In both figures, it is clear that the sensor noise is the main limitation at high frequencies. Indeed, the control on PSD become greater than the control off between $10\,Hz$ and $11\,Hz$ due to the sensors. Also for both direction, the actuator noise is not a problem when passing through the system dynamic. Indeed, the PSD corresponding to the contribution of the actuator noise is multiple orders of magnitude below the control on response. The disturbance contributions to the final PSD can also be discussed. It is interesting to see that the ground motion in translation is the main contribution as its curve is almost perfectly superposing with the final PSD. The ground rotation has less impact even in the rotational noise budget. Indeed, the ground rotation become the main contribution only at extremely low frequencies around $2\,mHz$ in figure 5.25b. Since no data were available for the ground rotation, the PSD used for the ground motion in translation is also used for the rotation. Then the curve representing the contribution of the ground rotation is less representative compared to the translation.

In terms of performances, it can be seen for the translational direction that the isolation is effective between $100\,mHz$ and $10\,Hz$ which is the wanted bandwidth. However, the two orders of magnitude of isolation are not fulfilled all over the bandwidth. Indeed, it is reached between $1\,Hz$ and $10\,Hz$. For the rotational direction, it can be seen that isolation is reached until the point where the noise of the sensor causes the amplification. However, between $10\,mHz$ and $1\,Hz$, the two orders of magnitude are not reached.

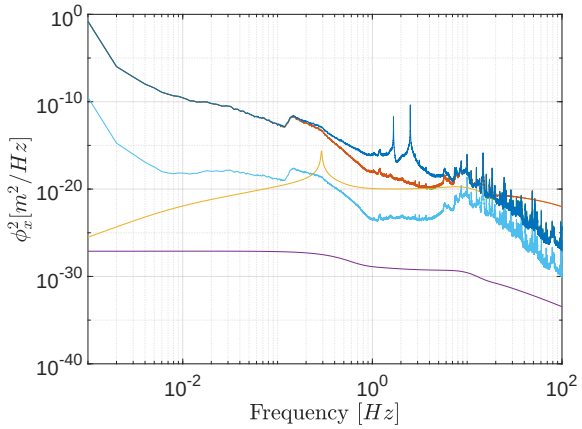

(a) Noise budget in translation. — is the control off response, — is the control on response, — is the contribution of the sensors to the final PSD, — is the contribution of the actuators to the final PSD, — is the contribution of the ground translation to the final PSD, and — is the contribution of the ground rotation to the final PSD.

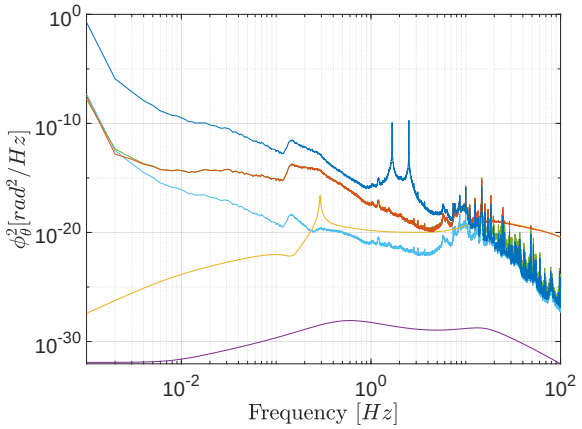

(b) Noise budget in rotation. — is the control off response, — is the control on response, — is the contribution of the sensors to the final PSD, — is the contribution of the actuators to the final PSD, — is the contribution of the ground translation to the final PSD, and — is the contribution of the ground rotation to the final PSD

Figure 5.25: Noise budget showing the PSD of the different noises taken into account and the response of the system in translational and rotational direction.

Chapter 6

Experimental implementation

Now that the $\mathcal{H}_\infty$ method has been applied to a theoretical model, the methodology can be extended to a more representative one. The goal of this model, provided by PML, is to represent the AP of the E-TEST project prototype well enough to develop a controller that will be applied to it. Moreover, this model only represents the AP, without the IP, IPP, etc. Then, dummy masses have been placed to represent the inertia of those elements. However, this model is not analytical unlike the first one. Indeed, it has been designed using the ***Simscape*** tool provided by the ***matlab*** environment as can be seen in figure 6.1. From the representation, it can be seen that the model contains every element discussed in chapter 4 with the added dummy masses in grey. It is then important to make sure that this model follows experimental data obtained from measurements of the prototype. Otherwise, the controller that will be obtained may not be applicable. As a first test, this controller only aims at damping the AP of the prototype in the vertical direction.

6.1 Controller development

In this first section, as was done for the 2DOF model, the development of the damping controller will be explained. However, since many of the principles have been explained for the previous model, it will be considered trivial for this chapter and many things will not be re-developed.

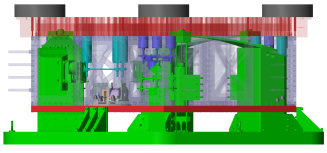

(a) CAD modeling of the AP from the E-TEST project prototype. This is a transversal view.

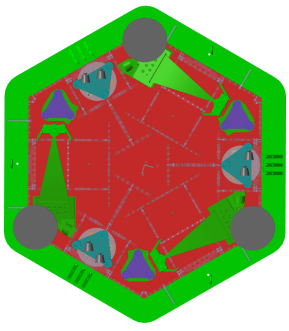

(b) CAD modeling of the AP from the E-TEST project prototype. This is the top view.

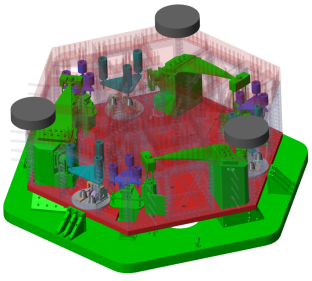

(c) CAD modeling of the AP from the E-TEST project prototype. This is an isometric view.

Figure 6.1: CAD modeling of the AP of the E-TEST project prototype as described in chapter 4. This has been done on ***Simscape*** in the ***matlab*** environment and was provided by PML.

6.1.1 Plant model

In order to implement the controller, a plant sufficiently close to the experimental data must be used. Then, the model developed on ***Simscape*** must be fine-tuned. Especially, the different poles must coincide to have corresponding modes between the model and reality. This is important for the $\mathcal{H}_\infty$ method since it uses the plant provided to develop the controller as has been explained in section 3.5 and demonstrated with the 2DOF model. To do so, different stiffness from springs but also the AP itself have been modified to make the modes match. More than the stiffness, the placement of the springs can also be fine-tuned. Indeed, this will also make vary the different modes. Other parameters could not be modified, as the actuators and sensors positions. This has an impact on the different poles and zeros of the model, but then the outputs and inputs of the controller would not correspond anymore to the real actuation that would be sent to the AP due to a mismatch between those actuators in the model and in the prototype. The same logic can be applied to the sensors. The information sent to the controller would not correspond anymore to the same displacement in the model and in the prototype. Moreover, the actuators of the prototype cannot be moved. In figure 6.2, the comparison between the tuned model in blue and the experimental data in orange can be seen. The outputs and inputs considered are

$$\boldsymbol{u} = \begin{bmatrix} F1V & F2V & F3V \end{bmatrix} \quad \boldsymbol{y} = \begin{bmatrix} VINS1 & VINS2 & VINS3 \end{bmatrix}$$

$\boldsymbol{u}$ containing the different vertical actuators and $\boldsymbol{y}$ the different VINS. Their position on the AP has been described in chapter 4. The focus was then the corresponding peaks between each curve. The two first peaks after $1\,Hz$ are rotational modes around the axis normal to the view seen in figure 6.1a. The third one is simply the translational mode in the vertical direction. The model shown in the figure is considered precise enough since it captures the dynamic of those three modes and due to the fact that only damping is wanted. This model is manipulated in the form of a state-space. However, each state is not a physical degree of motion as it would be in the 2DOF analytical model. Indeed, with ***Simscape***, the states obtained in the state-space correspond to joints placed in the model and making the link between two degrees of freedom. Also, it contains then a lot more states than in the previous model. No analytical description of the state-space will then be given but the algorithm synthesizing the controller still has access to the same type of information, meaning a state-space model. This one is just more complex. This then means that the controller will also have more states, since with the $\mathcal{H}_\infty$ method the controller has the same order as the plant.

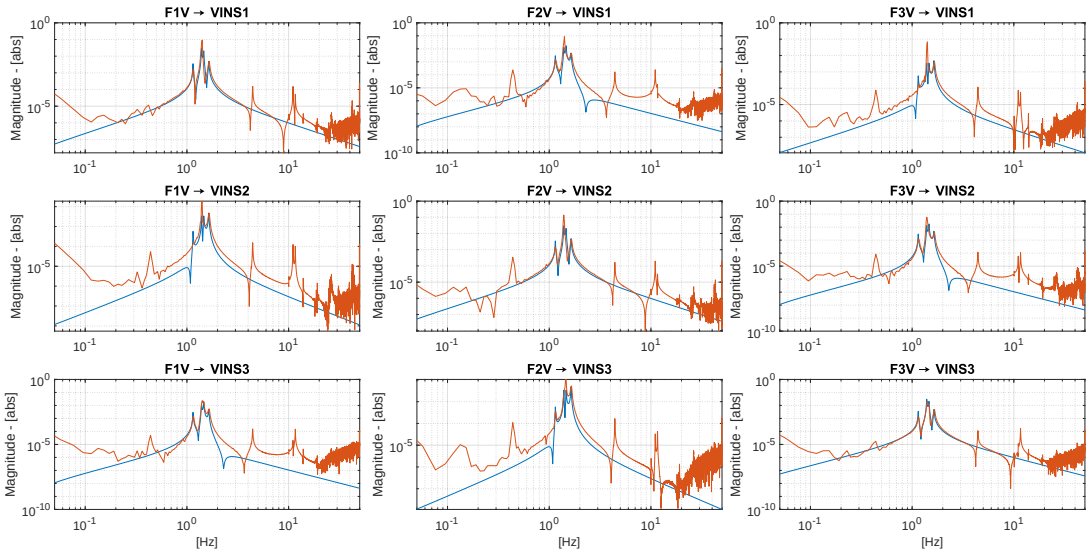

Figure 6.2: Bode plots of the ***Simscape*** AP model (which is ——) compared to the experimental one (which is ——). The inputs are the three vertical actuators and the outputs are the three VINS.

6.1.2 Setup of the problem

Now that the model developed matches well enough the experimental data, it can be used to produce a controller. As explained in section 3.5, the outputs and inputs of the system will be categorized, allowing the $\mathcal{H}_\infty$ method for the reduction of the wanted signals and disturbances. The exogenous signals are noted $\boldsymbol{w}$ and correspond to the motion of the ground in each degree of freedom. The error signals firstly contain the actuators signals. As already explained for the 2DOF model, this permits to limit the allowed actuation effort. Since the goal is to damp in the vertical direction, the state corresponding to the translational motion of the AP center in the vertical direction must be an error signal. Then, following the same reasoning, the signals of the VINS sensors are also included. The control variables are the signals of the three vertical actuators and the measured variables are the signals of the three VINS. Those latest will be used to close the loop on the model. This organization of the problem can be seen in figure 6.3. In the scheme, the position of the different weights can already be seen, but their choice is made in the following section.

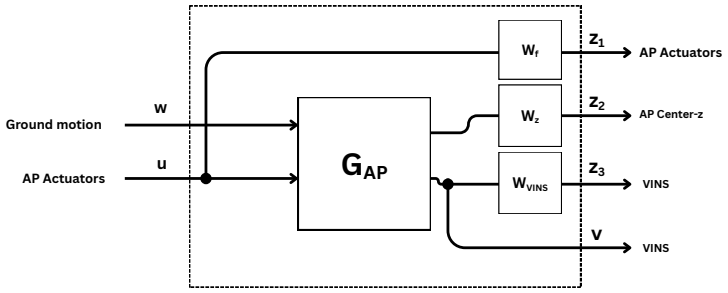

Figure 6.3: Organization of the AP system in terms of inputs and outputs for the $\mathcal{H}_\infty$ method. $\boldsymbol{z_1}$ is a vector containing the signals of the three actuators, $\boldsymbol{z_2}$ is a unique signal of the AP in the vertical direction, $\boldsymbol{z_3}$ is a vector containing the signals of the three VINS and $\boldsymbol{v}$ is a vector containing the signals of the three VINS that will be used for the feedback. $\boldsymbol{w}$ is a vector containing the motion of the ground in the six degrees of freedom and $\boldsymbol{u}$ is a vector containing the signals of the three vertical actuators.

Following the problem that has been set up, the $\mathcal{H}_\infty$ method will minimize this problem :

$$\left\| \begin{bmatrix} 0 & W_f \\ W_z S_{\boldsymbol{w} \to z_{AP}} & 0 \\ W_{VINS} S_{\boldsymbol{w} \to \boldsymbol{VINS}} & 0 \end{bmatrix} \right\|_\infty$$

which takes as inputs the exogenous signals, meaning the ground motion in six direction and the three vertical actuators and as outputs it has the actuators signals, the center of the AP in the vertical direction and the signals of the three VINS.

6.1.3 Choice of the weights

The choice of the weights is straightforward from the selection made for the 2DOF model. Indeed, the same process can be followed. High gain is applied at low frequencies for good tracking performances while low gain is taken for high frequencies to limit any overshoot. Moreover, applying too much gain at high frequencies could magnify noises which would degrade the performances. Then, the shape of the weights is the same as for the 2DOF model. However, from one system to another, the intensity

of the signals varies. The gain applied to those weights must be fine-tuned depending on the system itself. The weights applied to the vertical motion of the AP and the VINS signals are presented in figure 6.4, while no weight is applied to the actuators. Indeed, constraining the actuators was producing an unstable controller. Since only damping is wanted for the experiment, there is no need for massive actuation. This will be highlighted in the next chapter, analyzing the gain loop produced with the controller. It will be shown that the control bandwidth is small, as well as the magnitude of the gain loop in this bandwidth.

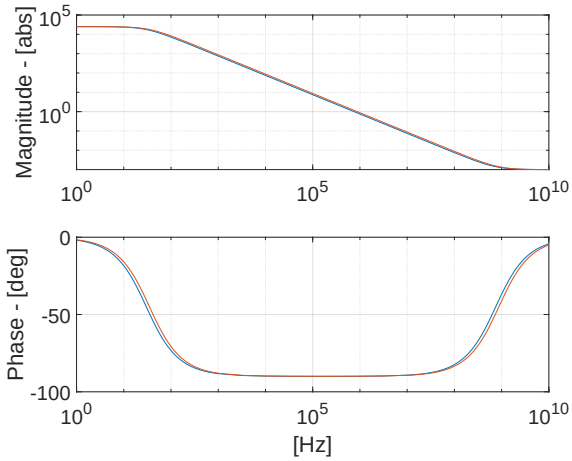

Figure 6.4: Bode plot of the weights applied to the outputs signals defined as error signals. —— is the weight applied to the AP center signal in the vertical direction. —— is the weight applied to all the signals of the VINS.

After implementing those weights, the final weighted plant has forty states. Thirty-six are coming from the model. Three correspond to the weights applied to each three VINS and the last one is the weight applied to the vertical motion of the AP as shown in figure 6.3. This represents a lot of states that will be contained in the controller. However, this should still be applicable to the experimental setup but no more complicated model should be used. Indeed, the material allowing for the implementation of the controller to the real sensors and actuators is limited by a number of fifty states.

6.1.4 Controller and filter

Since the problem has been prepared and that all the weights are selected, the $\mathcal{H}_\infty$ method can be used. The obtained controller can be seen in figure 6.5. As wanted when selecting the measured and control signals, the controller takes as inputs the signal provided by the VINS and gives as outputs the signals of the three vertical actuators. In the figure, the controller is in blue and the controller with a HPF is also shown in orange. The first observation is that the magnitude of the controller is smaller compared to the controller developed for the 2DOF model shown in figure 5.8. This is due to the fact that the controller was supposed to isolate while this one is only made for damping. Also, as already observed with the 2DOF model, at low frequencies, a lag can be observed. It can also be seen that the HPF is effective around $10^{-2}\,Hz$. At high frequencies, as already observed too for the simpler model, the 'bump' can be seen. However, between those common formations of the $\mathcal{H}_\infty$ method, there are poles and zeros forming peaks and valleys depending on the input output combination. Those are not damped much. This being plant inversion is a hypothesis, meaning that this controller would not be robust depending on variation of the system.

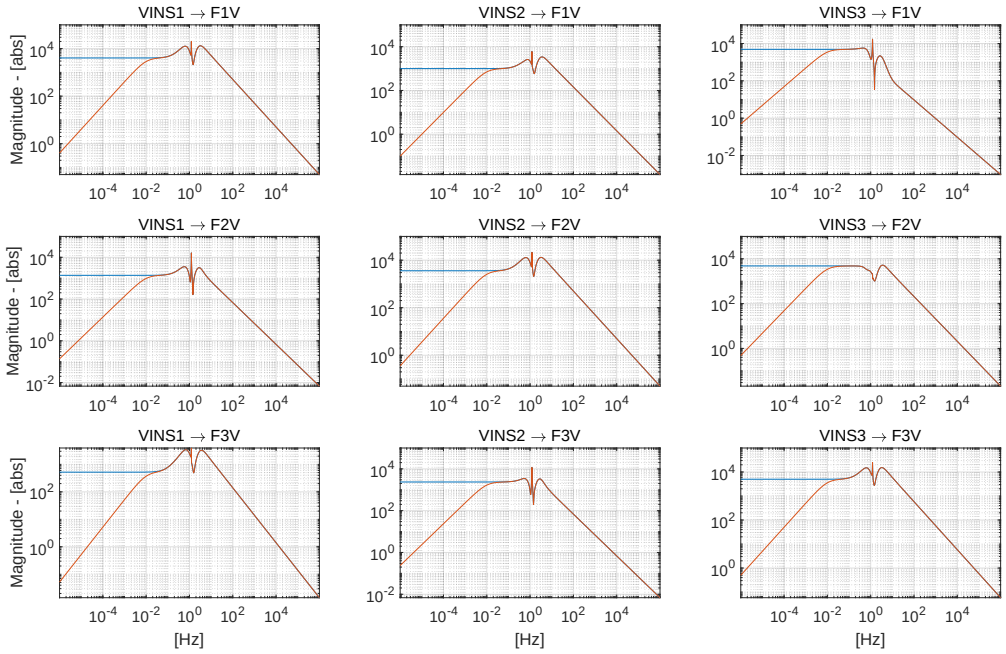

Figure 6.5: Bode plot of the controller produced for the AP model using the $\mathcal{H}_\infty$ method. It takes as inputs the signals of the VINS and gives as outputs the signals that will be provided to the actuators. — is the controller coming directly from the $\mathcal{H}_\infty$ method. — is the controller with the HPF applied.

6.2 Controller Implementation

Now that the controller for damping has been developed, its performances when applied to the plant can be analyzed. This is the subject of this section. The analysis will be done for the gain and closed loop. Those theoretical results will then be confronted to the experiment.

6.2.1 Gain Loop

Now that the controller has been developed, the first step is to analyze the gain loop which is shown in figure 6.6. It takes then the VINS as controller inputs and as outputs the VINS from the system.

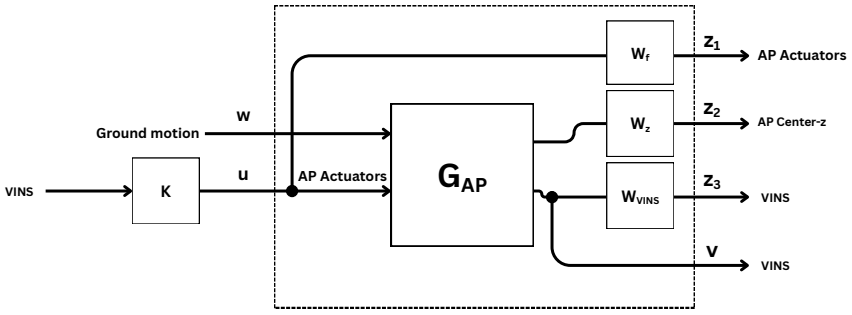

Figure 6.6: Schematic of the gain loop of the AP model.

The bode plots of this gain loop are shown in figure 6.7. Those are not experimental results. They are computed using the AP model and the synthesized controller. Since this latest was designed to only apply damping to the system, it can be seen that only a small part of each curve is above the unity line ($0\,dB$). The controller is only active around the main peaks, as wanted. Indeed, the control bandwidth is between $1\,Hz$ and $2\,Hz$ approximatively, depending on the input output combination. Also, the magnitude of the gain loop is lower than one order of magnitude, then there is no preoccupation for the actuators since no big efforts would be required.

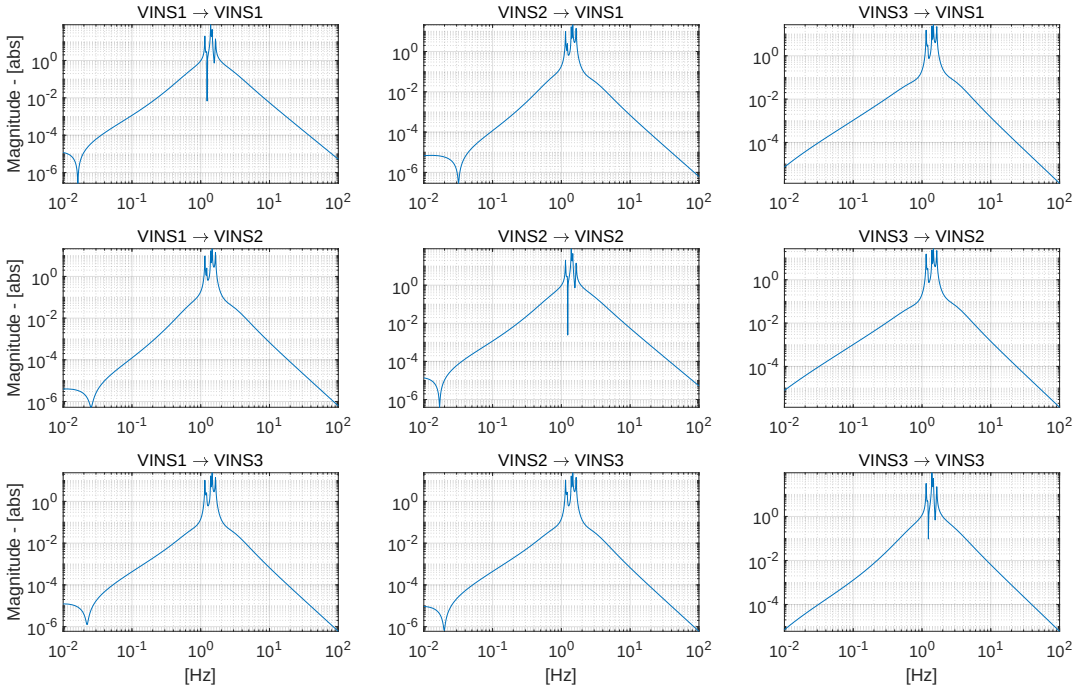

Figure 6.7: Bode plots of the gain loop of the AP model. The inputs and outputs are the three VINS.

6.2.2 Closed Loop

The loop can then be closed on the theoretical model as presented in figure 6.8 where the open loop is in blue and the closed loop in orange. It can be seen that the system is well damped. Indeed, those peak are diminished of at least one order of magnitude in each plot. Also, at the border of the control bandwidth, slight magnification can be seen. However, for the rest of the frequencies, there is no control since the closed loop follow exactly the open loop curve.

The performances of the controller are then assured on the model developed using the experimental data. The effects are what is expected when designing the controller. However, this controller has to be tested on the real prototype. The objective is to retrieve the same performances but, as seen in figure 6.2, some miss-matching can be seen in off-diagonal elements. Then, those variations compared to the real dynamic of the system could cause problems to the application of the controller to the prototype. The theoretical results that have been presented will then have to be put into perspective with the real performances obtained on the E-TEST project prototype.

As was done for the 2DOF model, the performances of the $\mathcal{H}_\infty$ method can be stated using the SVD. This time, no matrices are shown since all the outputs, and then the dynamics, concern the vertical direction. The plot of the singular values depending on the frequency is shown in figure 6.9. It can be seen, as in the closed loop, that the different dynamics of the open loop in blue are slightly

damped as wanted. The red dotted horizontal line is the value of gamma that corresponds to the maximum of the obtained singular values of the closed loop in orange. It can be noticed that minor dynamics have been intensified at very low magnitude. However, their magnitude is still negligible. The $\mathcal{H}_\infty$ method has been successfully applied to the system.

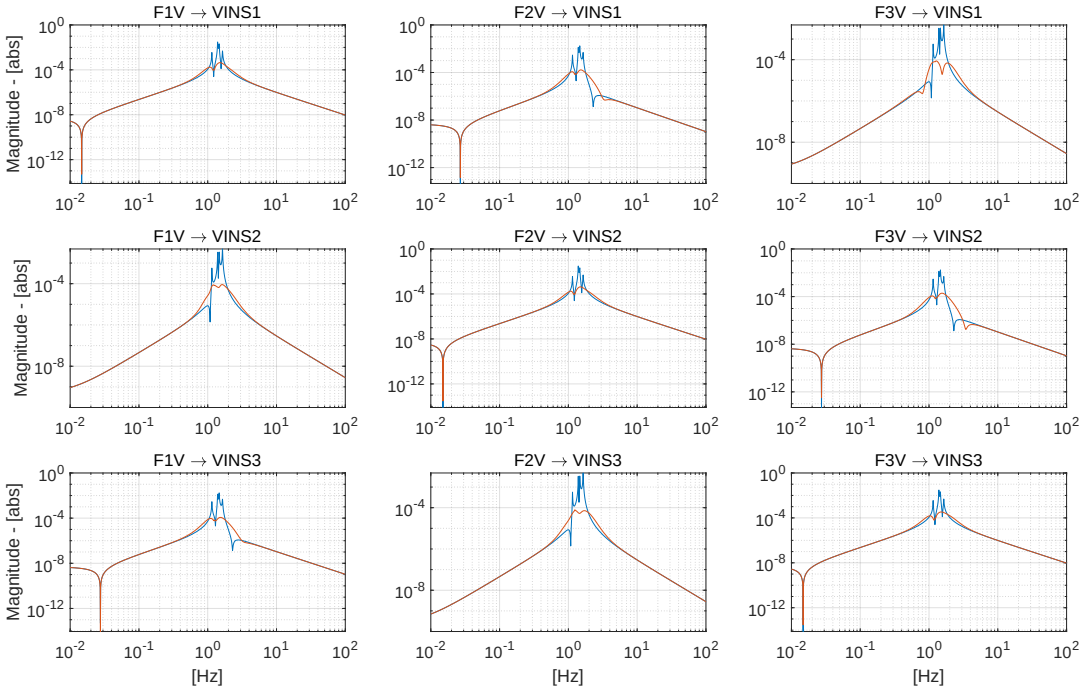

Figure 6.8: Bode plots of the closed loop of the AP model compared to its open loop. The inputs are the three vertical actuators and the outputs are the three VINS. — is the open loop. — is the closed loop.

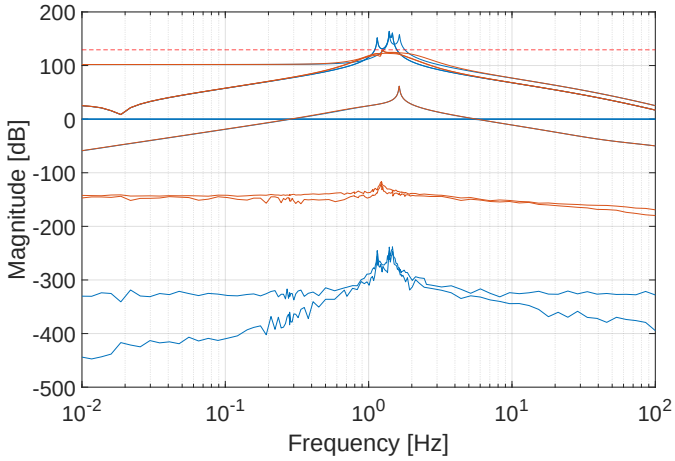

Figure 6.9: Plot of the singular values depending on the frequency for the weighted plant, the closed loop weighted plant. — is the singular values of the weighted plant. — is the singular values of the closed loop weighted plant. The red horizontal line corresponds to the value of gamma.

6.2.3 Experimental results

If we want to apply the controller to the real structure, it is good practice to assure that the linear augmentation of the gain until 100% of its initial value does not pass by unstable configuration. This theoretical procedure is shown in figure 6.10 where the gain of the controller applied to the developed model is progressively increased and represented in the pole-zero map of the closed loop obtained. It is clear that no configuration is unstable since each system is in the left half plane. However, it can be noticed that some poles are close to the imaginary axis. Then, the system could not be very robust. However, the other poles are going away from the axis once the gain is increased. Also, some other poles further left are approaching the axis. However, they are far from it.

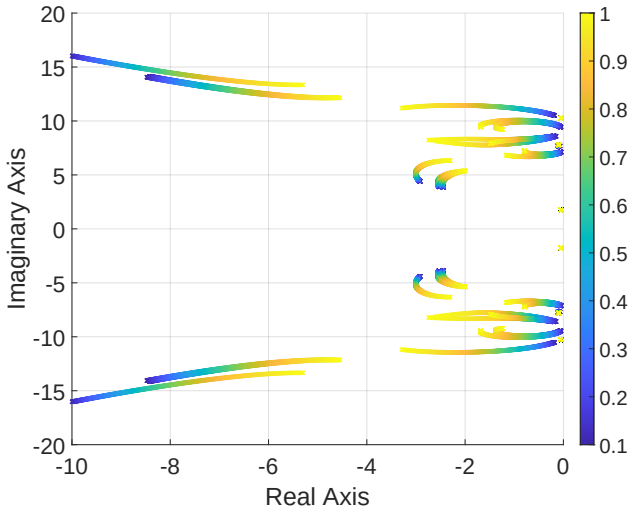

Figure 6.10: Pole-zero map of the closed loop made with the developed model and the controller, increasing its gain. This is not the experimental system.

The controller is then theoretically applicable to the real system, which has then been done. However, the gain could not be increased up to 100%. Indeed, the amplitude of the signals of the actuators was increasing continuously when its frequency was around $5\,Hz$. This attests of instabilities of the closed loop system at that frequency. However, the controller has been applied with its gain being 20% of its original value. The measure of the ASD from the collocated actuator sensor pairs is shown in figure 6.12. From those plots, it can be seen that the main peaks are indeed damped. The controller is then able to have effects on the real system. The $\mathcal{H}_\infty$ method has then been successfully applied to the prototype. However, around $5\,Hz$, the instabilities are clearly visible since a peak is present at that frequency. An assumption could be that this instability corresponds to one of the modes present in the experimental curve seen in figure 6.2 which is not modelized by the ***Simscape*** system. Then, the controller not being produced with the knowledge of this mode, could make the system unstable around this frequency. However, even without the knowledge of this peak, as long as the model follows the general trend of the dynamic of the system, those unmodelled modes should only result in decrease in the performances. Another possibility is that the off-diagonal elements of the model shown in figure 6.2 are less precise compared to the experimental curve. This can be confirmed by looking at the closed loop of both the model and the experiment. If the same tendencies are observed, this could be the confirmation of this explanation. To do so, other measurements have been taken using the same controller with 20% of its gain to reproduce the condition of the first experiment. This allows for the closed loop transfer function from each vertical actuators to all VINS to be retrieved. This will be compared to the closed loop of the model developed in ***Simscape***. The same controller with 20% of its gain is also used with the model. This permits a fair comparison. This can be observed in figure 6.11. The measurement are reliable from $0.5\,Hz$ to $5\,Hz$. This is clearly visible in the diagonal element

of the figure where the blue curve is the model and the orange curve is the experimental results. In this bandwidth, it can be noticed that the diagonal elements of the model in closed loop are almost perfectly fitting with the data. However, in the off-diagonal elements, differences can be observed as expected. Indeed, in the model, most of the off-diagonal elements present a roll-off with two different slope after the peak corresponding to the vertical and rotational modes. From the experimental curve, it is clear that this roll-off follows a single slope as it can be observed in the diagonal element. Due to these two slopes, the peak of the real system around $5\,Hz$ is most of the time not aligned with the dynamic described in the model for the off-diagonal elements, even if it is not modelled. It is then at a magnitude higher than the magnitude of the model at that frequency. This shows that the differences between the model and the real system are too excessive. They are magnified when closing the loop causing the instabilities encountered when applying the controller. To conclude, this experimental example has shown that the application of such kind of controller produced with robust control method as $\mathcal{H}_\infty$ was possible. However, since the method required a representation of the system to produce the controller, this model must be accurate enough not to end with instabilities as it was the case in this implementation. Then, only a better model would be required to obtain better performances and developed a controller for proper isolation and not only damping.

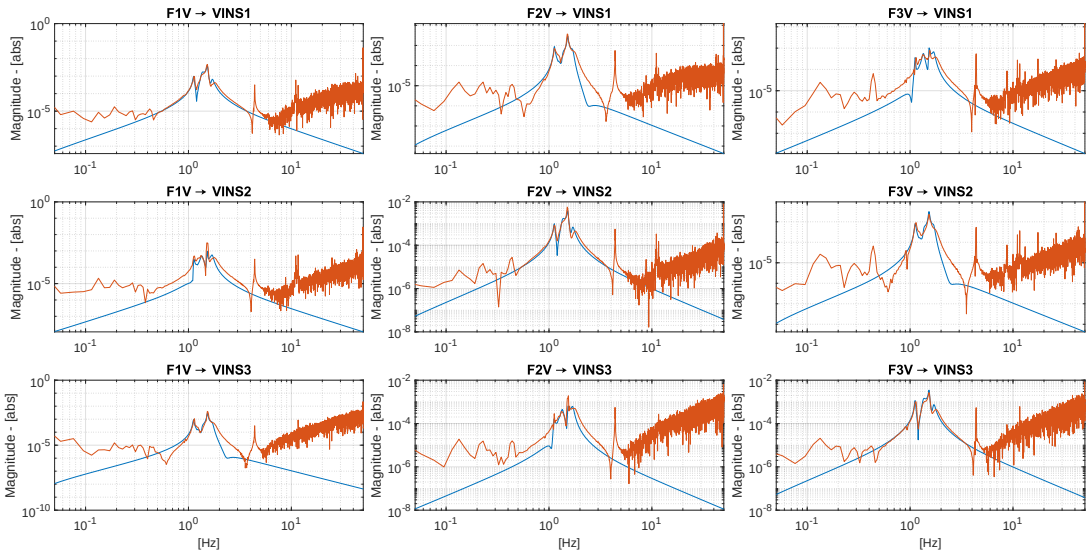

Figure 6.11: Bode plots of the closed loop of the AP model made in ***Simscape*** compared to the one obtained experimentally. — is the model, and — is the experimental curve. The inputs are the three vertical actuators and the outputs are the three VINS. The controller used for the model is the same that has been implemented, meaning the one developed with a gain of 0.2.

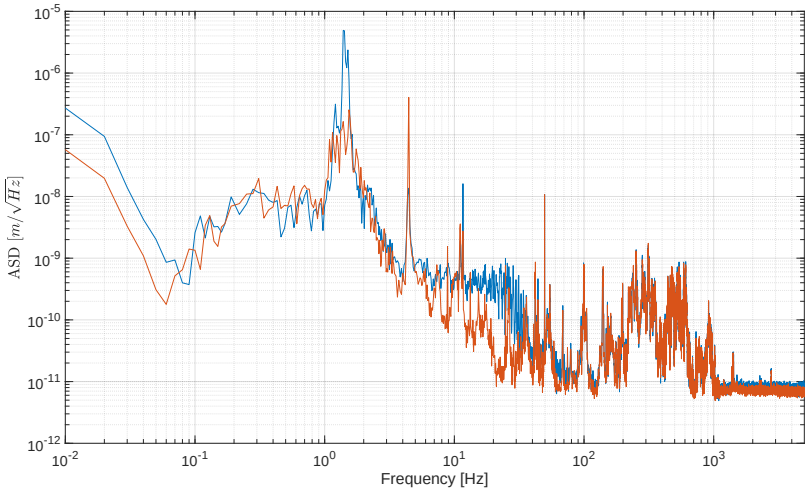

(a) ASD of the experimental results from the first actuator to the first VINS.

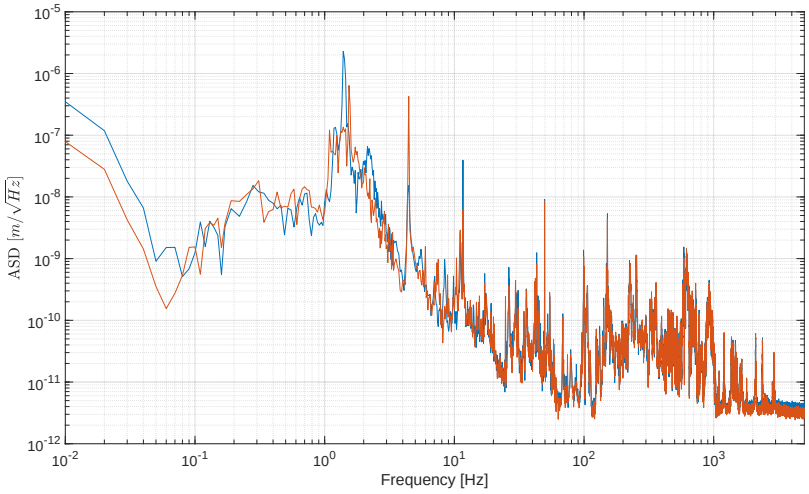

(b) ASD of the experimental results from the second actuator to the second VINS.

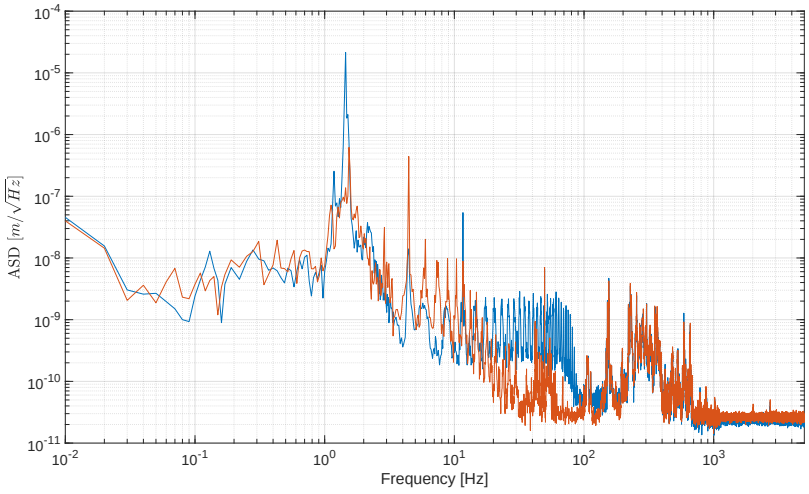

(c) ASD of the experimental results from the third actuator to the third VINS.

Figure 6.12: ASD of the experimental results from actuators to VINS. — is the open loop. — is the closed loop.

Chapter 7

Conclusions and perspectives

In this chapter, the conclusions that can be drawn from the accomplished work are explicitly stated alongside a reminder of each step leading towards the development of the final controller. Secondly, the perspectives of this work are established. Indeed, this thesis represents only the first stages of the implementation of such controller. Then, the future development and the important leads must be clearly defined for the searcher that will take over this development.

7.1 Conclusions

To conclude, the aim of this work was to understand and implement the $\mathcal{H}_\infty$ method on models of the E-TEST project prototype to obtain implementable controllers. This has been rarely done using robust control method on such complex model. Finally, one of those controllers should be applied to the prototype to prove the feasibility of such method in practice.

Thus, a simplified model representing only the AP in one degree of translation and one of rotation has been used for a first implementation of the $\mathcal{H}_\infty$ method, the 2DOF model. This was provided by PML. It has been chosen since it was complex enough to highlight some features of the method but also simple enough for a first implementation, making it perfect to detect early the problems that could arise or its advantages. Then, the different inputs and outputs of the system have been classified as required by the method. All inputs from the ground have been considered as disturbances and the inputs corresponding to the actuators are chosen to later close the loop of control. The sensor outputs alongside the degrees of freedom of the AP are set to be minimized to achieve isolation. The same is done for the signal of the actuators to prevent their saturation and provide a control over their efforts. The choice of the weights for those signals has been done. The low-pass filter shape was shown to be the best. The different gain for each function was fine-tuned depending on the signal. Once the controller was produced, and a high pass filter applied to it, its performances could be assessed. It was shown that the method could compensate the dynamics of the sensors at lower frequencies. The nature of the signal provided as input to the controller was determined to be an important factor shaping the final controller. Also, unusual formations have been observed at higher frequencies. Those provoke the presence of the double slope roll-off. It has been seen that the closed loop performances were not meeting exactly the requirements. However, the gain needed for the performances reached was already high. More performances would have led to an unimplementable controller. The robustness has been tested by applying uncertainties to certain parameters of the model. It has been determined that the variables of the sensor were the limiting ones. It was obvious that the $\mathcal{H}_\infty$ method was designed for the nominal system. Then, having a sensor with a higher or lower natural frequency was just making the system drift from its nominal state, leading to instabilities. However, after sampling 10000 systems, around 75% turned out stable, which can be considered as robust. It has also been shown that a supplementary damping loop before the control loop was not increasing the robustness. Hypothesis

have been made about the fact that the $\mathcal{H}_\infty$ method was creating a controller taking into account the worst case of the plant, which was not changed by applying damping in the first loop.

With the acquired knowledge of the implementation of such controller, it was decided to develop one for the prototype, focusing only on damping since it was the initial implementation on the structure. The same procedure as for the 2DOF model has been followed to develop the controller. The only difference was that the model provided by PML was developed in ***Simscape***. This is not an analytical model. However, like the previous model, it only depicted the AP, and the influence of the IPP or any other parts were replaced by dummy mass in the model. Indeed, the goal was to only damp the platform since the rest of the prototype was not ready. Then, the controller has been made for damping only, and its performances have been confirmed with the model. It has also been assured that the closed loops formed with a controller corresponding to a reduced gain of the original one were all stable until reaching 100% of the initial gain. Indeed, during the implementation, the gain of the controller was progressively increased to be sure that no instabilities would degrade the prototype. In practice, the gain of the controller has been set to 20% maximum as instabilities were encountered around $5\,Hz$. However, the controller was damping the prototype. This has proven that robust control methods could be applied to such complex MIMO systems. After investigation, the instability is due to miss-matching of the model in the off-diagonal element of the system.

To conclude, the difference of the controllers developed with the $\mathcal{H}_\infty$ method compared to classical controller as PID have been highlighted with the 2DOF model. Then, it has been shown that it was possible to implement such controllers in complex systems to perform at least damping. The main limitation of the method is the model. Indeed, it is due to miss-matching between the model and the experiment that the controller was not fully applied. Moreover, if the model is improved, it should not contain more states since the order of the controller depends on the order of the system given to the method. Then, an accurate model must be chosen, but it should remain as simple as possible.

7.2 Perspectives

After completing this work, questions and precision issues remain. To reach a complete analysis of the subject, some points should be further explored. The main improvement of the method would be the design of a model fitting the experiment, even in the off-diagonal element. This way, it would confirm that the limitation of the application of the full controller was linked to those miss-match. It would also enable the implementation of a controller designed for broader purposes beyond damping. An additional approach regarding the model would be the development of sub-models focusing only on a specific aspect of the dynamics of the prototype. This would produce models of lower order facilitating the implementation of controllers. Indeed, it was clear that the increasing complexity of the model is a problem for the performances of the method.

On the other hand, for the understanding of the method, it would be interesting to further analyze the stability of the obtained system using tools adapted to MIMO systems such as the disk margin for example. It is also necessary to further investigate why the application of a damping loop does not lead to an increase in robustness. A different organization of the problem could be tested. Indeed, for this implementation, it has been decided to include the sensor outputs in the error signals. However, a more complete comparison with different setup of problem could provide a good understanding of the method. The weights applied to the actuators could also be modified depending on their direction, making those weights adapted to the degree of freedom influenced by the actuator. Frequency dependent weights could also be applied in order to concentrate the actuators efforts at low frequency. Other implementation of the $\mathcal{H}_\infty$ method could be implemented on ***matlab***. For example, the µ-synthesis could be used, considering the ground to be a perturbation. Also, the controller developed for the prototype presents peaks and valleys in its bode plots, which is unusual compared to the controller developed for the 2DOF model. Confirmation should be brought to the fact that this represents plant inversion. Indeed, if it is the case, this will turn out to be an issue since this would make the controller not robust. The leads mentioned above should provide an adequate foundation for future research.

Bibliography

[1] Matthew Bailes, Beverly K Berger, PR Brady, M Branchesi, Karsten Danzmann, M Evans, Kelly Holley-Bockelmann, BR Iyer, T Kajita, S Katsanevas *et al.* : Gravitational-wave physics and astronomy in the 2020s and 2030s. *Nature Reviews Physics*, 3(5):344–366, 2021.

[2] Gravitational waves, einstein's ripples in spacetime, spotted for first time. `https://www.science.org/content/article/gravitational-waves-einstein-s-ripples-spacetime-spotted-first-time`, 2016.

[3] What is a gravitational wave? `https://spaceplace.nasa.gov/gravitational-waves/en/`, 2020.

[4] Michelson interferometer. `https://www.britannica.com/technology/Michelson-interferometer`, 2025.

[5] Sheila Rowan et al. : Gravitational wave detection by interferometry (ground and space). *Living Reviews in Relativity*, 3, June 2000.

[6] Matthew Pitkin, Stuart Reid, Sheila Rowan et Jim Hough : Gravitational wave detection by interferometry (ground and space). *Living reviews in relativity*, 14:1–75, 2011.

[7] Python gravitational wave interferometer noise calculator. `https://pypi.org/project/gwinc/`.

[8] B Abbott, F. Abbott, Ranav Adhikari, A. Ageev, Bruce Allen, Ria Amin, S. Anderson, Warren Anderson, Melody Araya, H. Armandula, Fedah Asiri, Peter Aufmuth, Carsten Aulbert, Stanislav Babak, R. Balasubramanian, Stefan Ballmer, B. Barish, C. Barker-Patton et M. Fyffe : Detector description and performance for the first coincidence observations between ligo and geo. *Nuclear Instruments and Methods in Physics Research Section A: Accelerators, Spectrometers, Detectors and Associated Equipment, v.517, 154-179 (2004)*, 05 2016.

[9] Peter R. Saulson : Thermal noise in mechanical experiments. *Phys. Rev. D*, 42:2437–2445, Oct 1990.

[10] What is photon shot noise? `https://camera.hamamatsu.com/us/en/learn/technical_information/thechnical_guide/photon_shot_noise.html`.

[11] WA Edelstein, J Hough, JR Pugh et W Martin : Limits to the measurement of displacement in an interferometric gravitational radiation detector. *Journal of Physics E: Scientific Instruments*, 11(7):710, 1978.

[12] Ameer Sider, Loïc Amez-Droz, Anthony Amorosi, F Badaracco, P Baer, G Bruno, A Bertolini, Christophe Collette, P Cebeci, Chiara Di Fronzo *et al.* : E-test prototype design report. *arXiv preprint arXiv:2212.10083*, 2022.

[13] S Braccini, C Bradaschia, R Del Fabbro, A Di Virgilio, Isidoro Ferrante, Francesco Fidecaro, R Flaminio, A Gennai, A Giassi, A Giazotto *et al.* : Seismic vibrations mechanical

filters for the gravitational waves detector virgo. *Review of scientific instruments*, 67(8):2899–2902, 1996.

[14] Vincenzino Dattilo : The virgo suspensions: design and recent performance measurements. *Physics Letters A*, 318(3):192–198, 2003.

[15] Fabrice Matichard, B Lantz, Richard Mittleman, Kenneth Mason, J Kissel, B Abbott, S Biscans, J McIver, R Abbott, S Abbott *et al.* : Seismic isolation of advanced ligo: Review of strategy, instrumentation and performance. *Classical and Quantum Gravity*, 32(18):185003, 2015.

[16] T Akutsu et al : Vibration isolation systems for the beam splitter and signal recycling mirrors of the kagra gravitational wave detector. *Classical and Quantum Gravity*, 38(6):065011, mar 2021.

[17] Ameer Sider : *TOWARDS LOW FREQUENCY SEISMIC ISOLATION OF LARGE CRYOGENIC MIRROR*. Thèse de doctorat, ULiège - University of Liège [Engineering], Belgium, 2024.

[18] control theory. `https://www.britannica.com/science/control-theory-mathematics`.

[19] Katsuhiko Ogata : Modern control engineering.

[20] Sigurd Skogestad : Multivariable Feedback Control: Analysis and Design.

[21] The singular value decomposition (svd). `https://math.mit.edu/classes/18.095/2016IAP/lec2/SVD_Notes.pdf`.

[22] Ad Damen et Siep Weiland : Robust control. *Measurement and Control Group Department of Electrical Engineering, Eindhoven University of Technology*, 2002.

[23] John E Bibel et D Stephen Malyevac : Guidelines for the selection of weighting functions for h-infinity control. *Naval Surface Warfare Center: Dahlgren Division*, pages 1–18, 1992.